Pontificia Universidad Católica de Chile
Facultad de Física
Instituto de Astrofísica

The Blue Straggler Star Populations in Galactic Globular Clusters

by

Mirko Simunovic Muñoz

Thesis presented to the Instituto de Astrofísica, Facultad de Física, Pontificia Universidad Católica de Chile to obtain the degree of Doctor in Astrophysics

Thesis presented to the Combined Faculties for the Natural Sciences and for Mathematics of the Ruperto-Carola University of Heidelberg, Germany to obtain the degree of Doctor of Natural Sciences

Supervisors	:	Prof. Dr. Thomas H. Puzia
		Prof. Dr. Eva K. Grebel
Correctors	:	Prof. Dr. Marcio Catelán
		Prof. Dr. Dante Minnitti
		Prof. Dr. Jorge Alfaro

Santiago – Heidelberg 2016

Dissertation

submitted to the
Instituto de Astrofísica, Facultad de Física
Pontificia Universidad Católica de Chile, Chile
for the degree of
Doctor in Astrophysics

submitted to the
Combined Faculties for the Natural Sciences and for Mathematics
of the Ruperto-Carola University of Heidelberg, Germany
for the degree of
Doctor of Natural Sciences

Put forward by

Mirko Simunovic Muñoz
born in: Antofagasta, Chile

Oral examination: October 19, 2016

The Blue Straggler Star Populations in Galactic Globular Clusters

Mirko Simunovic Muñoz
Astronomisches Rechen-Institut

Referees: Prof. Dr. Eva K. Grebel
Prof. Dr. Thomas H. Puzia

Abstract

The puzzling existence of Blue Straggler Stars (BSSs) implies that they must form in relatively recent events, after the majority of the constituent globular cluster (GC) stellar population was formed. In this thesis we compile a large set of independent work to help understand the formation of BSSs. In Chapter 2 we present new proper-motion cleaned BSS catalogs in 38 Milky Way GCs based on multi-passband and multi-epoch treasury survey data from the Hubble Space Telescope. We study the accuracy of our proper motion measurements using estimates of central velocity dispersions and find very good agreement with previous studies in the literature. Finally, we present a homogeneous BSS selection method, that expands the classic BSS selection parameter space to more evolved BSS evolutionary stages. In Chapter 3 we present the largest ever data set of velocity dispersion profiles of BSSs, which confirm that BSSs are populations that have been greatly affected by two-body relaxation, as it has been previously expected based on basic equipartition principles. In addition, we show from photometric BSS mass estimates that there is a striking correlation between the average BSS mass and the cluster dynamical age. We relate the measured proper-motion velocity dispersions with the photometric BSS mass estimates and use them to propose a novel interpretation of BSS CMDs and its relationship with the binary-evolution and dynamical formation channels. In Chapter 4 we present the first dynamical study of BSSs in three galactic GCs: NGC 3201, NGC 5139 (ωCen), and NGC 6218. We measure the $v\sin(i)$ values of the sample BSSs and find their distribution functions peaked at slow velocities with a long tail towards fast velocities in each globular cluster. We find that the BSSs in each of the GC sample which show $v\sin(i) > 70$ km s^{-1} are all found in the central cluster regions. In all globular clusters we find rapidly rotating BSSs that have relatively high differential radial velocities which likely put them on hyperbolic orbits, suggestive of strong dynamical interactions in the past. In Chapter 5 we present a multi-passband photometric study of the BSS population in NGC 1261. The inner BSS population is found to have two distinct sequences in the color-magnitude diagram, similar to double BSS sequences detected in other GCs. These well defined sequences are presumably linked to single short-lived events such as core collapse, which are expected to boost the formation of BSSs. In agreement with this, we find a BSS sequence in NGC 1261 which can be well reproduced individually by a theoretical model prediction of a 2 Gyr old population of stellar collision products, which are expected to form in the denser inner regions during short-lived core contraction phases. We argue that NGC 1261 can be considered a candidate for the post-core-collapse bounce state seen in dynamical simulations of old GCs.

Zusammenfassung

Die gegenwärtig noch unverstandene Bildung von Blue Straggler Sternen (BSS) in Kugelsternhaufen impliziert, dass sie sich in relativ jungen Ereignissen bilden müssen, nachdem die Kugelhaufen-Sternpopulation gebildet wurde. In dieser Arbeit präsentieren wir eine große Menge unabhängiger und neuer Beobachtungen, um die Bildung von BSS besser zu verstehen. In Kapitel 2 stellen wir neue Eigenbewegungssternkataloge von BSS in 38 Milchstraßenkugelsternhaufen vor, die auf Multi-Filterbeobachtung basieren und mit dem Hubble-Weltraumteleskop in einer Zeitspanne von 7 Jahren aufgenommen wurden. Wir untersuchen die Präzision und Genauigkeit unserer Eigenbewegungsmessungen der zentralen Geschwindigkeitsdispersionen und finden eine sehr gute übereinstimmung mit früheren Studien in der Literatur. Schließlich präsentieren wir eine homogene BSS-Selektionsmethode, die den klassischen BSS-Parameterbereich erweitert, um zusätzliche, weiter entwickelte BSS Entwicklungsstadien zu berücksichtigen. In Kapitel 3 stellen wir den größten jemals zusammengetragenen Datensatz von Geschwindigkeitsdispersionspofilen von BSS Populationen in Kugelsternhaufen zusammen. Diese Daten bestätigen, dass die BSS-Populationen stark durch Zweikörperinteraktionsprozesse beeinflusst werden, was zuvor durch theoretische Studien anhand der Prinzipien der Energieequipartition grundlegend erwartet wurde. Wir zeigen eine auffällige Korrelation zwischen der photometrisch bestimmten durchschnittlichen BSS Masse und dem dynamischen Alter des Kugelsternhaufens. Wir korrelieren die gemessenen Eigenbewegungsgeschwindigkeitsdispersionen mit den photometrischen BSS Massenabschätzungen und nutzen sie für eine neuartige Interpretation von BSS in Farbhelligkeitsdiagrammen sowie zu der Erörterung ihrer Beziehung zu den durch dynamische Entwicklung der Kugelsternhaufen und der Binärstern-Entwicklung bestimmten Bildungsmechanismen. In Kapitel 4 stellen wir die erste dynamische Studie von BSS in drei galaktischen Kugelsternhaufen vor: NGC 3201, NGC 5139 (ωCen) und NGC 6218. Wir messen die Rotationsgeschwindigkeiten ($v\sin(i)$) von BSS und finden, dass ihre Verteilungsfunktionen bei langsamen $v\sin(i)$ Werten kulminiert, die wiederum in jedem Kugelsternhaufen durch eine ausgeprägte Verteilung zu schnelleren Geschwindigkeiten charakterisiert ist. Wir beobachten, dass diejenigen BSS, welche $v\sin(i) > 70$ km s^{-1} zeigen, alle in den zentralen Haufenbereichen zu finden sind. In allen Kugelsternhaufen finden wir schnell rotierende BSS, die relativ hohe Differenzradialgeschwindigkeiten aufweisen und sich wahrscheinlich auf nicht gebundenen Hyperbelbahnen befinden, was auf starke dynamische Wechselwirkungen in der Vergangenheit hindeutet. In Kapitel 5 präsentieren wir eine photometrische Multifiteruntersuchung der BSS Population in NGC 1261. Die inneren BSS zeigen zwei unterschiedliche Sequenzen im Farbhelligkeit-Diagramm auf, was ähnlich zu anderen Doppel-Sequenzen, die in anderen Kugelsternhaufen gefunden wurden. Diese gut definierten Sequenzen

sind vermutlich auf einzelne kurzlebigen Ereignisse, wie z.B. der sogenannte Kernkollaps, zurückzuführen und die Bildungsraten von BSS steigern. In übereinstimmung mit diesem Resultat finden wir eine BSS-Sequenz in NGC 1261, die auch durch ein theoretisches Modell vorhergesagt ist. Dieses Model ist in übereinstimmung mit den Daten bei einer BSS Population, bei der es sich um 2-Gyr-alte Kollisionsprodukte handelt, die sich in den dichteren Innenbereichen der Kugelsternhaufen bilden. Dies geschieht bevorzugt, während der kurzlebigen Kontraktionsphasen des Kugelsternhaufenkerns. Wir argumentieren, dass NGC 1261 ein Kandidat für einen sogenannten post-kernkollaps Kugelsternhaufen ist, die auch in numerischen Simulationen von alten Kugelsternhaufen beobachtet werden.

Resumen

La desconcertante existencia de las Estrellas Rezagadas Azules (ERAs) implica que deben formarse en acontecimientos relativamente recientes, después de que se formó la mayor parte de la población estelar del cúmulo globular (CG) constituyente. En esta tesis se compila un conjunto grande de trabajo y métodos independientes para ayudar a comprender la formación de las ERAs. En el capítulo 2 se presentan nuevos catálogos, descontaminados con movimientos propios, de ERAs en 38 CGs galácticos basados en datos multi-banda y multi-época del telescopio espacial Hubble. Estudiamos la exactitud de las mediciones de movimiento propio utilizando estimaciones de dispersiones de velocidad central y encontramos una muy buena concordancia con estudios previos en la literatura. Por último, se presenta un nuevo método de selección homogénea de ERAs, que expande el espacio de parámetros de selección clásico de ERAs hacia etapas evolutivas más avanzadas en el diagrama color-magnitud. En el capítulo 3 se presenta el mayor conjunto de datos hasta la fecha de perfiles de dispersión de velocidades de ERAs, que confirman que las ERAs son poblaciones que han sido afectadas en gran medida por la relajación dinámica de dos cuerpos, tal como se ha previsto anteriormente basado en principios básicos de equipartición. Además, usando estimaciones fotométricas de masa de ERAs mostramos que existe una correlación sorprendente entre la masa promedio de las ERAs y la edad dinámica del cúmulo. Relacionando los resultados de las dispersiones de velocidad obtenidas del movimiento propio junto con los cálculos fotométricos de masa de ERAs proponemos una nueva interpretación del diagrama color-magnitud de ERAs y su relación con los canales de formación relacionados a evolución de binarias y a interacciones dinámicas. En el capítulo 4 se presenta el primer estudio dinámico de ERAs en tres CGs: NGC 3201, NGC 5139 (ωCen), y NGC 6218. Se miden los valores de $v \sin(i)$ de la muestra de ERAs y se muestra que en cada CG sus distribuciones alcanzan un valor máximo a velocidades de rotación lentas pero con una larga cola hacia velocidades altas. Encontramos que las ERAs en cada CG que muestran $v \sin(i) > 70$ km s^{-1} se hallan siempre en las regiones centrales del cúmulo. En todos los CGs se encuentran ERAs con alta velocidad de rotación que tienen un diferencial alto de velocidad radial relativo a las estrellas del cúmulo, lo cual probablemente sugiere órbitas hiperbólicas, indicando fuertes interacciones dinámicas en el pasado. En el capítulo 5 se presenta un estudio fotométrico multi-banda de la población ERA en NGC 1261. Se encuentra que la población central de ERAs tiene dos secuencias distintas en el diagrama color-magnitud, similar a las secuencias dobles de ERAs detectadas en otros CGs. Estas secuencias bien definidas están presuntamente vinculadas a eventos dinámicos tales como colapso del núcleo, el cual se espera que

sirva de catalizador en la formación de ERAs. En concordancia a esto, encontramos una secuencia de ERAs en NGC 1261 que puede ser bien reproducida individualmente por un modelo teórico de una población de 2 Gyr de edad de productos de colisiones estelares, los cuales posiblemente se forman en las regiones interiores más densas durante fases de contracción del núcleo. Se argumenta que NGC 1261 puede ser considerado como un candidato para el estado de rebote post-colapso del núcleo, el cual ha sido observado en las simulaciones dinámicas de CGs.

Acknowledgements

I cannot possibly list all the people who have made a positive impact in my life, and to whom I am always grateful. There have been several critical times in my life that, one way or another, helped to build in me the character and confidence that eventually led me to decide pursuing a career in science. I am therefore most grateful to life and to the amazing fortune of being able to get an education and take opportunities that most don't even have the privilege to consider. It is our obligation and responsibility as privileged humans, to use the tools that were offered to us and contribute accordingly to our community. I am therefore grateful, to all those who came before me, and helped create a modern society that values individual achievements and even supports those that, like me, dedicate their minds to the exciting world of science.

Still, I would like to dedicate some words to people that have helped considerably to the success of this work.

To my advisor and friend, Thomas, without whom I would have never even considered a thesis so vast and diverse in its methodology. His seemingly endless energy and enthusiasm is something that we, as graduate students, appreciate enormously. Undertaking a long and hard research project is something that requires conviction and can easily break your spirit when you don't see immediate progress. It is because of this, that the role of the advisor should be as much of scientific guidance, as of a private therapist. On that note, I would like to thank all of my fellow students and postdoctoral researchers, who undoubtedly are just as important in a process of scientific research. Specially to Roberto Muñoz, Javier Alonso, Matthew Taylor, and everyone in the Complex Stellar Population Group at PUC. Thank you to all of you who helped me obtain the fellowship at Heidelberg University. Thank you specially to Eva Grebel, my advisor during the time I spent in Germany. She always had nothing but the best disposition and good-willingness to help me finish my research at Germany.

To my parents, whose lives full of achievements did nothing but inspire and motivate me to reach a sincere sense of self-fulfillment. Thank you for giving me the great gift of a formal education and the even more important one of freedom. Because it is only through being free in your life's choices that you can truly understand the value in one's own work.

To my beautiful wife, Camila. Because you are my best friend and closest partner in crime. Your infinite support and care gave me strength in times when I thought I had no more to use. Thank you for so many late-hour nights of sharing coffee and companionship, which all resulted in significant portions of this work.

Publications

The work that is presented in this Thesis is largely based on research that has been published in peer-refereed journals during my Ph.D. For the interested readers, we provide the full references:

1. *"Blue Straggler Star Populations in Globular Clusters. I. Dynamical Properties of Blue Straggler Stars in NGC 3201, NGC 6218, and ω Centauri"*
   Simunovic, M., & Puzia, T. H. 2014, The Astrophysical Journal, 782, 49
2. *"The Blue Straggler Star Population in NGC 1261: Evidence for a Post-core-collapse Bounce State""*
   Simunovic, M., Puzia, T. H., & Sills, A. 2014, The Astrophysical Journal Letters, 795, L10
3. *"Blue Straggler Star Populations in Globular Clusters. II. Proper Motion Cleaned HST Catalogs of BSSs in 38 GCs"*
   Simunovic, M. & Puzia, T. H. 2016, Monthly Notices of the Royal Astronomical Society, Accepted on 2016 July 26.

Contents

Chapter 1

Introduction

At the beginning of all scientific fields there comes a time of crude observations and speculations. The multiple attempts at trying to explain a phenomena can then be viewed as extrapolations of sometimes incomplete and biased conclusions based on observations that are not always generally valid, but only true in a certain context. In time, those extrapolations will converge into a now more complex set of ideas. The scientific method works as the judge that will asses the validness of such set of ideas by simple falsification of its grounds as well as its predictions. Given sufficient time (and sometimes entire *careers*), many independent sets of such self-consistent ideas will connect based on their compatibility, and keep growing as more and more observations become available. This forms what is called the current paradigm. The field of astrophysics was once undoubtedly subject to that initial time of incomplete observations and ideas. Nevertheless, in the present the scientific community has gained such a complex understanding of the Universe that one cannot help but be amazed at the capabilities of the human mind[1]. Such knowledge is indeed the result of countless works and efforts throughout history.

The subject of this thesis falls in the more general subject of Globular Clusters (GCs). Our Milky Way has about 150 known GCs. They continue to serve as the most used laboratories for stellar evolution, given their relatively well constrained conditions. Therefore, GCs act as a natural *reservoir* of untapped information that astronomers have used for decades to shape the current paradigm of stellar formation and evolution, as well as the formation and evolution of stellar systems (e.g. the GCs themselves and also galaxies). In the last few decades, CCD cameras came to completely revolutionise the field of GCs, while also giving birth to new subjects of study that rely on high-resolution

---

[1] Ironically this now motivates one to try to understand the human mind *per se*. Yes, I am a "frustrated" neuroscientist. But then again, we are the Universe, just as much as a supercluster of galaxies is the Universe. So, what is an astronomer but not the Universe trying to understand itself?. Ok, back to the thesis.

imaging and spectroscopy. This thesis is the result of years of research in the field of Blue Straggler Stars (BSSs) in GCs. This is one such young field of study that is still undergoing constant reshaping of its paradigms. We have collected large amounts of data and tried to let the data speak for itself, while also not focusing on any specific question beforehand but letting the questions arise naturally from the observations. In that sense, the aim of this work is try to provide robust observational evidence that can help clarify the formation of BSSs and their tight relationship with the dynamical evolution of GCs. It is our hope that this work serves as a significant contribution to the understating of these topics, and can be considered a valuable step towards the shaping of a new paradigm in this constantly evolving field of astrophysics.

1.1 Globular Cluster Dynamics

The current understanding of the evolution of GCs is in part determined by the dynamical interactions between the member stars and the evolution of the large-scale gravitational potential. We can directly study such topics because of the nice conditions in which GCs are defined:

- They are essentially in isolated environments (although some are found in the bulge and the disk too)
- They are composed of (almost) coeval stellar populations (multiple stellar populations formed early in the cluster's lifetime are now known to be present in probably all GCs (Gratton et al., 2012))
- They contain no gas or dust
- They are almost spherical

It is clear that the denser regions in GCs are not collisionless systems and therefore two-body relaxation processes are expected to affect global properties. Two-body scattering events will induce, for example, close stellar interactions inducing binary hardening or disruption (Heggie, 1975). Two-body encounters can also result in a direct collision between stars. Complex interactions such as this are constantly shaping the evolution of the gravitational potential, and the potential itself is subsequently dictating the orbits of the star in the system. This non-trivial interplay between the stars and the potential is what drives the dynamical evolution of GCs.

In a more analytical approach, we can describe the physical laws governing GC evolution by introducing the radial moment of inertia of the system

$$I = \sum_{i=1}^{N} m_i \, |r_i|^2 \tag{1.1}$$

By taking the second derivative of the moment of inertia, we can trivially obtain

$$\ddot{I} = \sum_{i=1}^{N} 2m_i \left(v_i^2 + r_i \, \ddot{r_i} \right) \tag{1.2}$$

In dynamical equilibrium we must have by definition $\ddot{I} = 0$, and hence

$$\sum_{i=1}^{N} m_i \, v_i^2 + \sum_{i=1}^{N} m_i \, r_i \, \ddot{r_i} = 0 \tag{1.3}$$

If we consider the formal definition of kinetic energy and potential energy of self-gravitating systems, it is straight-forward to realise that the above can be written as

$$2\,K + U = 0 \tag{1.4}$$

where K is the kinetic energy and U is the total potential energy and the total energy is $E = K + U = -K$. This is simply the Virial Theorem. For a GC in virial equilibrium, this equation defines how the time-averaged kinetic and potential energy of the stellar system relate one to another. It tells us how much kinetic energy you need to keep the system stable. In such a virial state, at any point in the cluster there are as many stars moving inward as moving outward, that is to say there is no net radial flux (McMillan, 2015).

The thermal energy in the cluster flows from the core to the external regions through two-body relaxation, as stars experiencing close encounters transfer energy one to another. We then say that a cluster has become relaxed when the stars have evolved into a Maxwellian velocity distribution, and the timescale for this to happen is defined as the relaxation time (McMillan, 2015). The stars in the tail of the velocity distribution can adopt a velocity that is higher than the escape velocity and escape the cluster's potential. This reduces the total mass of the system and therefore the cluster expands, while the core contracts. The process repeats itself throughout the cluster's lifetime, and each time the core will again contract and heat up, while the extra thermal (kinetic) energy gets transported to the outer regions, causing the core to contract again and heat up again. This gravothermal instability can start a runaway process known as *core collapse* (Lynden-Bell & Wood, 1968; Cohn, 1980), although it is thought that additional energy sources in the core such as binary-hardening during dynamical interactions can efficiently support the core against collapse (Heggie & Aarseth, 1992; McMillan et al., 1990). The post-core-collapse phase can then be subject again to the same gravothermal instability and undergo a phase of large-amplitude core oscillations. This is yet to be confirmed observationally for GCs, but N-body simulations of realistic clusters have shown that they can occur (Hurley & Shara, 2012; Makino, 1996).

1.2 The Nature of Blue Straggler Stars

GCs are excellent laboratories of stellar evolution and host abundant representatives of some of the more exotic stellar evolutionary phases. One such, still relatively unexplored phase is known by the name of its representatives, namely Blue Straggler Stars (BSSs). BSSs are characterized by their effective temperatures and luminosities as members of the main-sequence stellar population. However, given the ages of their host GCs they are expected to have evolved off the main-sequence to become red giant stars long time ago as their Hertzsprung-Russell diagram parameters place them at higher temperatures and luminosities, thus higher stellar masses, with respect to the main-sequence turn-off point (Bailyn, 1995; Stryker, 1993). The existence of BSSs implies that they must form in more recent events, after the majority of the constituent GC stellar population was formed.

The original discovery of BSSs came when Sandage (1953) published his work on the globular cluster M 3, as part of his PhD thesis. He was studying the color-magnitude diagram properties of M 3 and reported a group of stars that were above the main-sequence and looked as if they were a younger population than the bulk of the cluster stars. His original color-magnitude diagram of M 3 is shown in Figure 1.1, where we also mark the location of BSSs with a red circle. The nature of BSSs was completely unknown in those early years, and many eccentric theories were developed to try and explain their significance. Yet, M 3 was still the only convincing example of true BSSs for many decades. It wasn't until the introduction of CCD cameras that BSS began to be discovered ubiquitously in GCs (see e.g. Sarajedini, 1993). In a more general astrophysical context, BSSs represent an important unsolved problem for a series of reasons: (*i*) They are still a missing piece in the theory of stellar evolution, particularly for binary systems. (*ii*) The formation channels expected from binary evolution are also most likely acting in the field, hence BSSs represent a component of a galaxy population that is usually ignored. (*iii*) Their blue colours means that UV photometry of unresolved galaxies is significantly affected by BSS flux. Our ability to model their frequencies in other galaxies is therefore essential when using synthesis stellar population models.

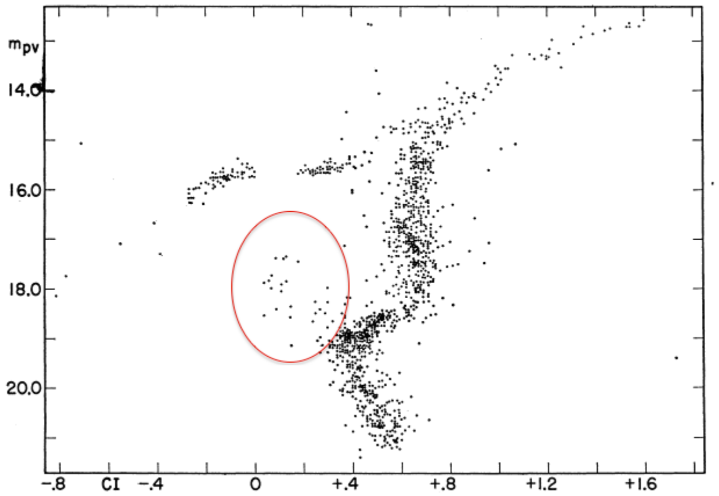

Figure 1.1: Color-magnitude diagram of M 3 obtained by Sandage (1953). We take this figure directly from his paper. The location of BSSs in the CMD is marked with a red circle.

1.3 BSS Formation Channels

In the recent literature, two formation mechanisms have gained most acceptance and are currently lively debated (see Sills, 2010, for a detailed review): *i*) BSSs form in stellar mergers induced by stellar collisions (Hills & Day, 1976), and *ii*) BSSs are rejuvenated stars forming by mass transfer as a result of binary evolution (McCrea, 1964). In principle, both of these scenarios could be actively at work and their predominance being a function of the local environment, although there is really no general consensus on this idea. We also note that separating both formation channels as completely independent processes, as sometimes is done in the literature, is probably not realistic, since the collision events that result in BSSs are frequently binary-mediated, just like mass-transfer can be triggered after a binary hardens during a close encounter (Hypki & Giersz, 2016a). It was first suggested that collision-induced BSSs are expected to form in the high density parts of GCs while mass-transfer BSSs are thought to form in the loose outskirts of GCs (Fusi Pecci et al., 1992). In that spirit, many efforts aimed at measuring which of the two mechanisms dominated (Knigge et al., 2009), while other results suggested that both mechanisms are simultaneously at work in GCs (Leigh et al., 2011). Recently, Ferraro et al. (2009) confirmed the presence of two distinct BSS sequences in M30 in a deep color-magnitude diagram (CMD) study, which the authors believe is suggestive of different formation histories/mechanisms for each BSS sequence. M30 is thought to have undergone core-collapse which could be responsible for the observed two BSS sequences in the CMD. The still unsolved problem of BSS nature is hence one of most importance for the accurate modelling of binary populations and binary evolution, as well as to the topic of stellar dynamics which is fundamental for the theory of dense stellar systems.

1.4 BSS Formation Diagnostics

One of the previous attempts at detecting a certain BSS formation channel is the C-O depletion measured in six 47 Tuc BSSs (Ferraro et al., 2006a). Such C-O depleted BSSs are expected if during their formation they accreted CNO-processed material from their binary companions. Therefore, such chemical anomalies may directly point to a mass-transfer mechanism. However, most of the BSSs in the sample were located in the outer regions of 47 Tuc, where mass-transfer induced BSS formation should be an active formation channel, and still only 14% of the studied BSSs were found having this C-O depletion (i.e. mass-transfer) signature. It is clear that the problem of BSS formation is far from being fully understood, and it is therefore fundamental to perform similar chemical analyses, including other elements, of BSSs in larger samples of GCs, significantly increasing the sample statistics.

Another potential indicator of the BSS formation mechanism may be their rotational velocity distribution function. In the mass-transfer scenario, the resulting BSS is believed to conserve most of the angular momentum from the binary system (Sarna & De Greve, 1996), therefore becoming a fast rotator ($v_{\rm rot} > 50$ km s^{-1}), as well as in the collision-induced formation scenario, in which it is also claimed that BSSs are formed having high rotational velocities (Benz & Hills, 1987). However, models show that in both cases BSSs could lose most of their initial angular momentum through mechanisms such as accretion disk braking/locking (Sills et al., 2005). This means that being able to link certain rotational velocity distributions to a certain formation mechanism is rather still complex.

Previous surveys of rotational velocities of BSSs include Lovisi et al. (2010) who found that 40% of the measured BSSs in M4 are fast rotators, which is the largest frequency of rapidly rotating BSSs ever detected in a GC, although no C-O depletion was found in any of these BSSs. Another study (Ferraro et al., 2006b) shows a flat radial distribution for the BSSs in NGC 5139 (ωCen), suggesting that this cluster is not completely relaxed yet. The same group has completed a spectroscopic survey of 78 BSSs in ωCen and found that the majority of them have rotational velocities $v\sin(i) < 20$ km s^{-1}, but still a considerable fraction (30%) are fast rotators of which some rotate even faster than 100 km s^{-1} (Lovisi et al., 2013a). Following the intriguing BSS double-sequence in M30 mentioned earlier, 12 BSSs were also observed in this cluster and most of them were found to rotate slowly (Lovisi et al., 2013b). Yet another example is the rotational velocity distribution measured for NGC 6397 (Lovisi et al., 2012) which shows most BSSs to rotate very slowly, and only one of them being a fast rotator.

The apparent tendency is therefore a similar BSS rotational velocity distribution function for many GCs, usually peaked around 10 km s^{-1}, and a low fraction of fast rotators, except for the cases of M4 and ωCen. The clear link between these observations and a definitive formation mechanism is still very unclear, since neither chemical analysis nor models have been able to successfully interpret these results. This rather complex scenario calls for larger surveys simultaneously sampling dynamical and chemical properties of BSSs with a homogeneous dataset in order to get a wider picture of the BSS formation processes and to improve on the statistical significance of previous results.

1.5 The link between BSS and GC Dynamical Age

The BSS formation channels described previously are strongly dependent on the local environment's dynamical state, and, therefore, BSSs can be used as tracers of past dynamical events, as well as of the current cluster dynamical state, given their strong response to two-body relaxation effects due to their relatively high stellar masses. Ferraro et al. (2012) proposed that the current BSS radial density profile can be used as a "dynamical clock" to estimate the dynamical age of a GC, and continued to classify a large set of GCs in three different classes according to their dynamical state. The dynamically oldest category contains, among others, GCs M 30 and NGC 362, which have been studied in this context more in detail by Ferraro et al. (2009) and Dalessandro et al. (2013). These studies have found that the BSS population is indeed consistent with dynamically old GCs. Furthermore, their CMDs reveal well defined double BSS sequences, which the authors claim are the result of single short-lived dynamical events, such as core-collapse. It is believed that during such core contraction the stellar collision rate would become enhanced, producing the bluer BSS sequence in the CMD, while the boosted binary interaction rate would lead to enhanced Roche-lobe overflows, thereby producing the redder BSS sequence. It is, therefore, clear that observational properties of BSSs can provide valuable information and put strong constraints on the dynamical evolution of individual GCs.

1.6 Outline of the Thesis

This thesis work was motivated by the general picture and the scientific questions described above. In particular, we wanted to conduct the larger ever study on BSSs that combined photometric and spectroscopic techniques for BSS samples in as many GCs as possible.

This document is the result of years of research on the observed properties of BSSs, and their connection to the potential BSS formation and dynamical evolution paradigm.

In Chapter 2 we combine high-resolution, multi-band and multi-epoch HST imaging data and construct the largest ever proper-motion cleaned catalogs of BSSs in the inner regions of GCs. Chapter 3 is designed as a sequel to the previous chapter. Here we use the BSS catalogs constructed in the previous chapter and study the physical properties of BSSs versus the cluster environment and their dynamical state. We relate the measured proper-motion velocity dispersions with photometric BSS mass estimates and use them to propose a novel interpretation of BSS CMDs and its relationship with the binary-evolution and dynamical formation channels. In Chapter 4 we move into another direction and study the spectroscopic dynamical information properties of wide-field BSS samples in three GCs. We derive radial and rotational velocities for a large set of BSSs and put new constraints for BSS formation. In Chapter 5 we move again in a different direction and use stellar collision models to study the color-magnitude diagram of the inner BSS population in NGC 1261 and compare it to the collision models predictions. We identify a remarkable collisional BSS sequence along with other interesting BSS populations in NGC 1261 and discuss these findings in the context of the particular dynamical state of the cluster. Finally, we summarise our work and write our conclusions in Chapter 6.

Bibliography

Bailyn , C. D. 1995, Annual Review of Astronomy and Astrophysics, 33, 133

Benz, W., & Hills, J. G., 1987, The Astrophysical Journal, 323, 614

Dalessandro, E., Ferraro, F. R., Massari, D., et al. 2013, The Astrophysical Journal, 778, 135

Ferraro, F. R., Sabbi, E., Gratton, R., et al. 2006, The Astrophysical Journal Letters, 647, L53

Ferraro, F. R., Sollima, A., Rood, R. T., et al. 2006, The Astrophysical Journal, 638, 433

Ferraro, F. R., Beccari, G., Dalessandro, E., et al. 2009, Nature, 462, 1028

Ferraro, F. R., Lanzoni, B., Dalessandro, E., et al. 2012, Nature, 492, 393

Fusi Pecci, F., Ferraro, F. R., Corsi, C. E., Cacciari, C., & Buonanno, R., 1992, The Astronomical Journal, 104, 1831

Gratton, R. G., Carretta, E., & Bragaglia, A. 2012, Astronomy and Astrophysics Reviews, 20, 50

Heggie, D. C. 1975, Monthly Notices of the Royal Astronomical Society, 173, 729

Heggie, D. C., & Aarseth, S. J. 1992, Monthly Notices of the Royal Astronomical Society, 257, 513

Hills, J. G., & Day, C. A. 1976, The Astrophysical Journal Letters, 17, 87

Hypki, A., & Giersz, M. 2016, arXiv:1604.07033

Hurley, J. R., & Shara, M. M. 2012, Monthly Notices of the Royal Astronomical Society, 425, 2872

Knigge, C., Leigh, N., & Sills, A. 2009, Nature, 457, 288

Leigh, N., Sills, A., & Knigge, C. 2011, Monthly Notices of the Royal Astronomical Society, 416, 1410

Lovisi, L., Mucciarelli, A., Ferraro, F. R., et al. 2010, The Astrophysical Journal Letters, 719, L121

Lovisi, L., Mucciarelli, A., Lanzoni, B., et al. 2012, The Astrophysical Journal, 754, 91

Lovisi, L., Mucciarelli, A., Lanzoni, B., Ferraro, F. R., & Dalessandro, E. 2013, arXiv:1301.3295

Lovisi, L., Mucciarelli, A., Lanzoni, B., et al. 2013, arXiv:1306.0839

Lynden-Bell, D., & Wood, R. 1968, Monthly Notices of the Royal Astronomical Society, 138, 495

Cohn, H. 1980, The Astrophysical Journal, 242, 765

Makino, J. 1996, The Astrophysical Journal, 471, 796

McCrea, W. H. 1964, Monthly Notices of the Royal Astronomical Society, 128, 147

McMillan, S. L. W. 2015, Ecology of Blue Straggler Stars, 225

McMillan, S., Hut, P., & Makino, J. 1990, The Astrophysical Journal, 362, 522

Sandage, A. R. 1953, The Astronomical Journal, 58, 61

Sarajedini, A. 1993, Blue Stragglers, 53, 14

Sarna, M. J., & De Greve, J. P., 1996, Quarterly Journal of the Royal Astronomical Society, 37, 11

Sills, A., Adams, T., & Davies, M. B., 2005, Monthly Notices of the Royal Astronomical Society, 358, 716

Sills, A. 2010, American Institute of Physics Conference Series, 1314, 105

Stryker, L. L. 1993, Publications of the Astronomical Society of the Pacific, 105, 1081

Chapter 2

Proper Motion Cleaned HST Catalogs of Blue Straggler Stars

2.1 Introduction

It has been shown that the present BSS population and its abundance ratio scales with GC structural parameters (Knigge et al., 2009; Leigh et al., 2007; Piotto et al., 2004). This helps to give constraints to the likely formation scenario (Davies, 2015; Leigh et al., 2013, 2011). At the same time, the dynamical evolution of GCs is driving much of the initial conditions, and BSSs are in fact good tracers of their current dynamical state (Ferraro et al., 2012, 2015). This broad context makes it necessary that we study BSS populations in the most general approach, by looking at them and their properties in multiple galactic GCs.

This approach led us to start looking at the dynamical properties of BSSs in multiple GCs. In particular, we have used wide-field samples of BSSs and studied the radial velocities and rotational velocities of BSSs in NGC 3201, NGC 6218 and NGC 5139 (ωCentauri) and we found interesting results regarding their dynamical properties (see Chapter 4). That study showed an apparent central segregation of fast rotating BSSs, which were preferentially located within one core radius of their parent cluster. This result was confirmed independently by Mucciarelli et al. (2014) for the case of ωCen, who also found a peak in the fast rotating BSS fraction at the inner regions of ωCen. This type of observation suggests that fast rotating BSSs form preferentially in the inner regions of GCs, where the higher rates of dynamical interactions may facilitate formation conditions that favor high angular momentum transfer. Such fast rotating BSSs observed in the inner cluster regions may be considered proxies for young BSSs, if these spin-down over time due to strong magnetic braking following their formation. Another clue that points towards this scenario is the finding of collision product BSSs in the inner regions of GCs (e.g. Ferraro et al., 2009), that seem to be coeval and produced by such environments of higher rates of dynamical interactions. Nevertheless, although the crucial interplay between BSS formation and GC dynamical evolution has recently gained enormous attention, a full dynamical characterization of BSSs is still lacking in the literature. In this work, we present a large effort to obtain proper motion cleaned catalogs of BSSs in several Galactic GCs.

The Chapter is organized as follows. Section 2.2 presents the data and data reduction, while section 2.3 describes the methods adopted for proper motion measurements and cluster member selection. Section 2.4 presents the analysis of the proper motion accuracy and the selection of BSS candidates. We summarize our work in Section 2.5.

2.2 Observations and Data Reduction

This work is based on Hubble Space Telescope (HST) observations of Galactic GCs which come from two large photometric Surveys. Firstly, "*The ACS Globular Cluster Survey*" (PI: Ata Sarajedini, HST Program 10775) which provides us with fully-calibrated photometric catalogs for the inner regions of GCs in the F606W and F814 filters, available on the ACS/WFC camera. Secondly, "*The HST Legacy Survey of Galactic Globular Clusters: Shedding UV Light on Their Populations and Formation*" (PI: Giampaolo Piotto, HST Program 13297), from which we obtain imaging data for the inner regions of GCs in the F275W, F336W, and F436W filters available on the WFC3/UVIS camera.

2.2.1 ACS/WFC Photometry

The ACS photometric catalogs come from the HST/ACS Galactic Globular Cluster Survey (Sarajedini et al., 2007). It consists of ∼30 min. exposures in the F606W ($\sim V$) and F814W ($\sim I$) bands for the central $\sim 3.4' \times 3.4'$ fields of 74 GCs. The photometry available in the online catalogs has been corrected to account for updated HST/ACS WFC zero points and calibrated in the Vega photometric system. These catalogs provide high quality photometry down to ∼6 mag below the main-sequence turn-off of most GCs. For quality purposes, we filter out all detections that have a QFIT value larger than 0.2 in the F606W or F814W photometry. See Sarajedini et al. (2007) for further details on this value.

2.2.2 WFC3/UVIS Photometry

For the purpose of this work, we limit ourselves to the F336W filter images alone, given that this filter has usually the most amount of frame exposures per cluster field, which serves our main goal of obtaining accurate astrometric measurements. The original data is comprised of FLT images downloaded from the Mikulski Archive for Space Telescopes (MAST)[1]. These FLT images are the calibrated and flat-field corrected by the automatic calibration pipeline CALWF3. The procedure that we apply for the construction of the final photometric catalogs is explained in the following subsections.

2.2.2.1 Charge-Transfer Efficiency Correction

It is well known that, when in orbit, the HST detectors suffer cumulative radiation damage. As a consequence, this produces charge traps that affect the movement of electrons during detector read-out. The observed effect of this diminished charge-transfer efficiency (CTE) is that point sources leave traces of charge in the direction of the amplifiers, affecting more pixels the further away from the amplifiers. Ideally, one would want all the trace counts that ”leaked” from a point source to be ”put back” to their original position on the detector. For such a correction, we apply the `wfc3uv_ctereverse` script, available from the STScI website, that converts the FLT files into FLC files. This script reverses the CTE effect, but does not offer a perfect correction, as the measured centroids of the stellar sources suffer small systematic offsets that are dependent on the source location across the chip. However, if understood this does not affect our results given that, as we shall see later, this uncertainty in the centroid is much smaller than the proper motion dispersion threshold we typically use for the cluster membership selection function.

2.2.2.2 Source Detection and Flux Measurements

The corresponding point-source photometry is performed on the FLC images using the standard `img2xym_wfc3uv` script provided by STScI. The software typically outputs $\sim$200k detections per frame. We adopt a higher-limit of 0.3 for the QFIT parameter, which records the fractional disagreement between the model and the image pixels, in order to filter out most of the noisy detections. Compared to the ACS photometry, this constraint has to be more relaxed given the shallower photometry of the WFC3 dataset.

---

[1] https://archive.stsci.edu

2.2.2.3 Geometric-distortion Corrections

The WFC3 UVIS detector is tilted at $\sim 21°$ about one of its diagonals, producing a projected rhomboidal elongation of $\sim 7\%$. This in turn changes the plate scale across the field. More precisely, the sky covered by a UVIS pixel varies by about ∼7% from corner to corner over the full field of view. Hence, the raw source coordinates obtained from the photometry are calibrated with the `WFC3_UVIS_gc` script in order to remove the corresponding geometric distortion effects. This is our final calibration and, from here on, all WFC3/UVIS catalogs mentioned in the text are implicitly the result of this procedure.

The final selection of the sample is mostly determined by the quality of the WFC3/UVIS imaging data. In particular, we decide to remove from the sample a small number of catalogs because of saturation affecting the position measurements of bright stars. The final target sample consists of 38 GCs, and their main properties are listed in Table 2.1, while Figure 2.1 shows the luminosity and metallicity distribution of the sample in relation to the entire Milky Way GC system.

2.3 Measuring Proper Motions

One of the advantages of combining the optical and near-UV catalogs is the possibility of measuring proper motions. Indeed, the two datasets used in our work were taken approximately 7 years apart, therefore providing a long enough period for the proper motions to be detectable. The series of steps taken to obtain proper motions can be summarized as follows:

1. For a given WFC3/UVIS filter, we find linear coordinate transformations for all different exposures (between 2 and 6 depending on the cluster) of the same cluster field and set them all to the coordinate frame of an arbitrary exposure.
2. We do a cross-match and keep only the sources detected in all exposures. We then calculate the average coordinate for each source and repeat (1) using the average coordinates as master the frame.
3. We calculate again the average coordinate for each source and and keep them as final coordinates of that cluster field.
4. We find linear transformations from the WFC3 master coordinates to the ACS reference frame.

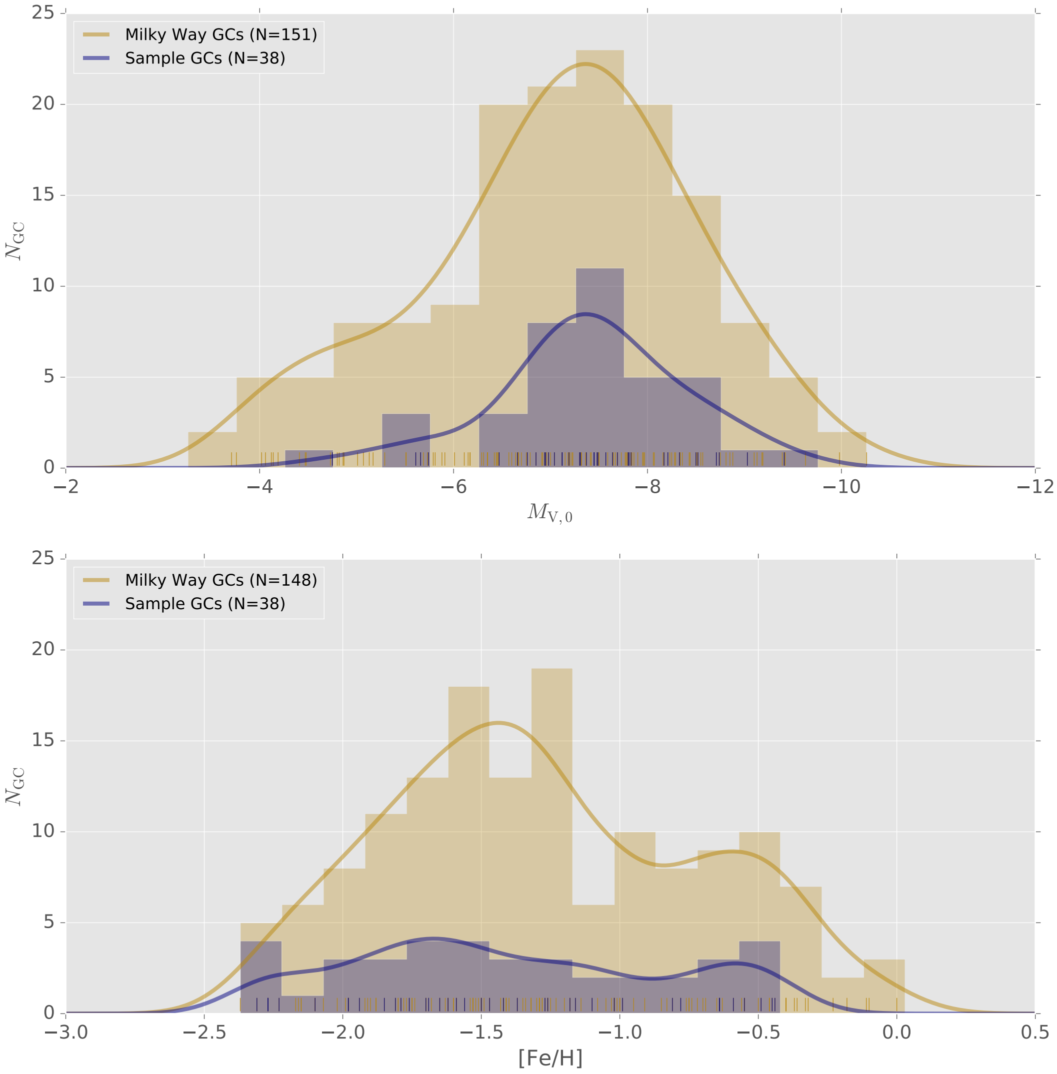

Figure 2.1: Luminosity and metallicity distribution functions of our 38 sample GCs in comparison with the total Milky Way GC system. The solid curves show non-parametric probability density estimates for each distribution. All values were taken from Harris (2010).

5. We cross-match both catalogs and, based on preliminary proper motions, select high-likelihood members and use them to find a new transformation solution.
6. We use this final transformation to map the WFC3 catalog coordinates into the ACS master reference frame.
7. We cross-match again both catalogs and measure the proper motions in pixel units directly as the difference between the two coordinate sets.

The details of this procedure are fully described in the following subsections.

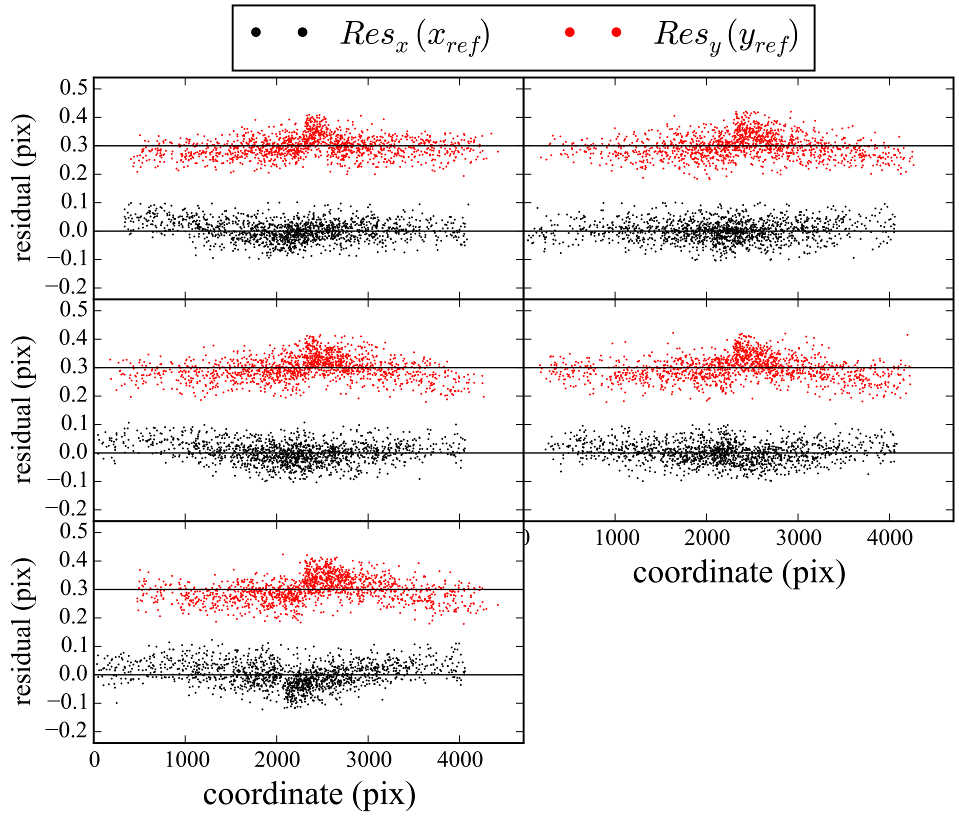

Figure 2.2: Coordinate transformation residuals obtained with `ccmap`. We show in each panel the corresponding residuals in the mapping of each individual NGC 6717 WFC3 exposure into the reference frame exposure. Black and red points show the residual in X as a function of reference X coordinate and the residual in Y as a function of reference Y coordinate, respectively. The residuals in Y have been shifted for clarity.

2.3.1 Creating the WFC3 Master Catalog

We take the resulting catalogs obtained after applying the procedure explained in Section 2.2.2 and group them by target cluster. The objective is to obtain a WFC3 master catalog which uses the astrometric information from all different exposures of the same target cluster. First, we arbitrarily choose one of the exposures to be the frame of reference to be mapped onto all other image frames. Then, we identify multiple star pairs on the individual exposures of the same target cluster in order to find a first-order initial coordinate transformation that sets every catalog's coordinate system in the chosen frame of reference. Each exposure was taken with an arbitrary rotation angle of the spacecraft, therefore we need a tool that can find, without any initial information, star pairs in catalogs that have arbitrarily shifted and rotated coordinates relative to one another. For this, we use the IRAF task `xyxymatch` with its *triangles* matching algorithm. This process defines a sample of a few dozen bright, non-saturated star matches in each frame catalog. These star matches serve as the input for the IRAF task `ccmap`

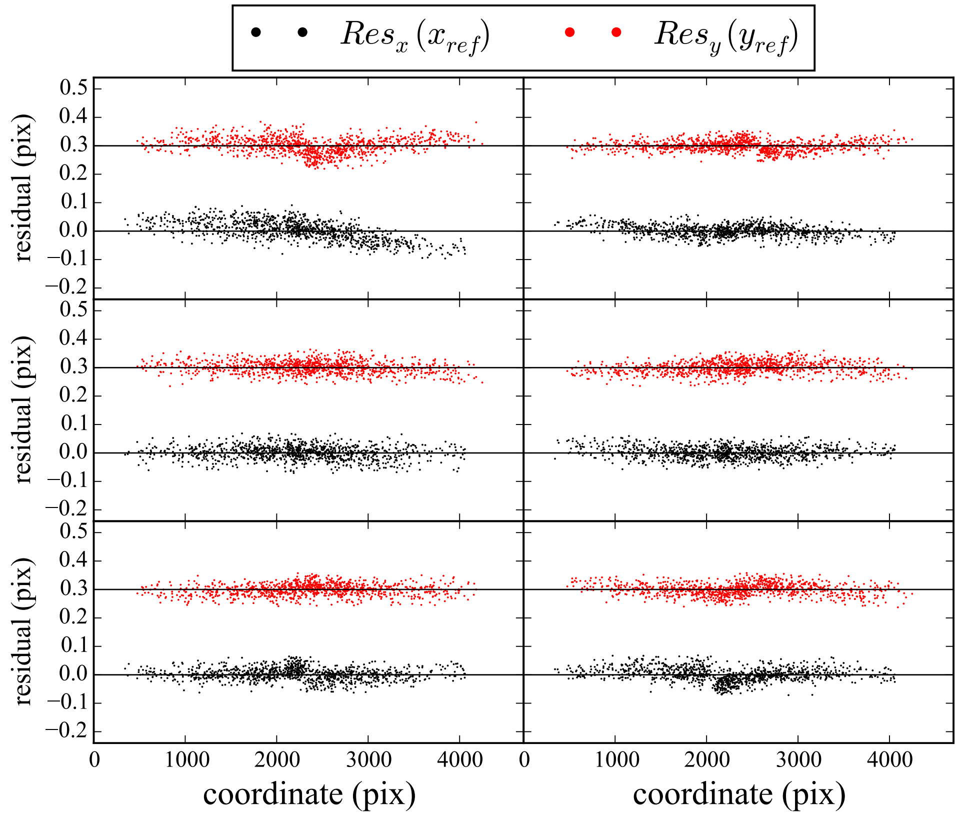

Figure 2.3: Same as Fig. 2.2 but using the average XY coordinates from all exposures as the reference frame in `ccmap`.

which calculates the initial coordinate transformation of each catalog into the frame of reference. The catalog coordinates are then transformed using the linear transformation within the IRAF task `ccsetwcs`. Once every catalog of a given target cluster is, to first-order, set to the same frame of reference, we repeat the process with `xyxymatch`, which now is able to find significantly more matching stars in all frames using only a few pixels as matching tolerance.

We use the augmented, full list of star matches, which now contains several thousands of stars as input for `ccmap` and allow a full 6-parameter fit for the transformation solution. We show in Figure 2.2 one representative set of residuals for a case of 6 different exposures of the same target cluster. Again, this solution is applied using `ccsetwcs` to all catalogs. At this point we perform a new source cross-match between every catalog of a target cluster and calculate the average X and Y coordinate of every source[2]. This average XY catalog is used in the following as the frame of reference and we reiterate the procedure. We show in Figure 2.3 the new resulting set of residuals from the same cluster catalogs as in the previous Figure. Note that there is an additional transformation coming from the

---

[2] This is true provided there is a detection in every exposure, which is not always the case for stars near the chip-gaps and edges of individual frames, which are not always covered by the detectors given the variations in pointing and spacecraft roll angle.

catalog that was before used as the frame of reference, and is now also available to map into the average XY catalog. As can be seen from the residuals shown in Figure 2.3, this method is able to correct for most of the lower-frequency systematics. However, a small sawtooth residual effect, caused by CTE effects (Baggett et al., 2015) is still visible and hard to remove entirely at this point for most catalogs. We perform a new and last source cross-match on all catalogs of a target cluster and recalculate the average X and Y coordinate of every source, which becomes the final WFC3 master coordinate catalog of a given target cluster. An important positive outcome is that part of the sawtooth effect is removed as it tends to cancel out when averaging over the different sub-exposure catalogs. We find this effect to be no more than ~ 0.03 pixels, and its impact on our measurements is discussed in the subsequent analysis sections.

2.3.2 Mapping the WFC3 Master Catalog into the ACS Coordinate Frame

At the beginning of our WFC3-to-ACS mapping procedure, we construct the WFC3 stellar luminosity function (LF) of every cluster and use it to detect the horizontal branch (HB) luminosity, which can be identified in the LF as a local overdensity in the brighter end. We then use the approximate F606W magnitude of the HB of each cluster as given in Dotter et al. (2010) and construct the LF in the range of two magnitudes brighter and fainter than the given HB F606W magnitude level. This way we find the peak of the HB optical LF, which we assume to be populated by the same group of stars as the peak of the LF from the WFC3 data. We select a small group of stars around the HB LF peak in both the WFC3 master catalog and the ACS catalog and use again the IRAF task `xyxymatch` with its *triangles* matching algorithm to find star matches. This does not give immediate results every time, and further manual interaction with the code is needed in some clusters for correct matches to be found. In particular, in some clusters we had to fine-tune the *nmatch* and *tolerance* parameters until correct matches were found. Once we have a small list of star-matches from both catalogs, it becomes basically a matter of repeating a similar procedure as explained in the previous subsection. First we use `ccmap` and `ccsetwcs` to set, to a first-order, the WFC3 master catalog of a cluster into the ACS coordinate reference frame. We then find a much larger list of matching stars using `xyxymatch` and use the full 6-parameter fit to find the new transformation solution with `ccmap`.

The solution is applied using `ccsetwcs` and then we perform a source cross-match using one pixel as matching tolerance. For the matched sources, we calculate now the preliminary proper motions and select the stars that have a proper motion within 1σ of the entire sample. These are assumed to have a high likelihood of being cluster members

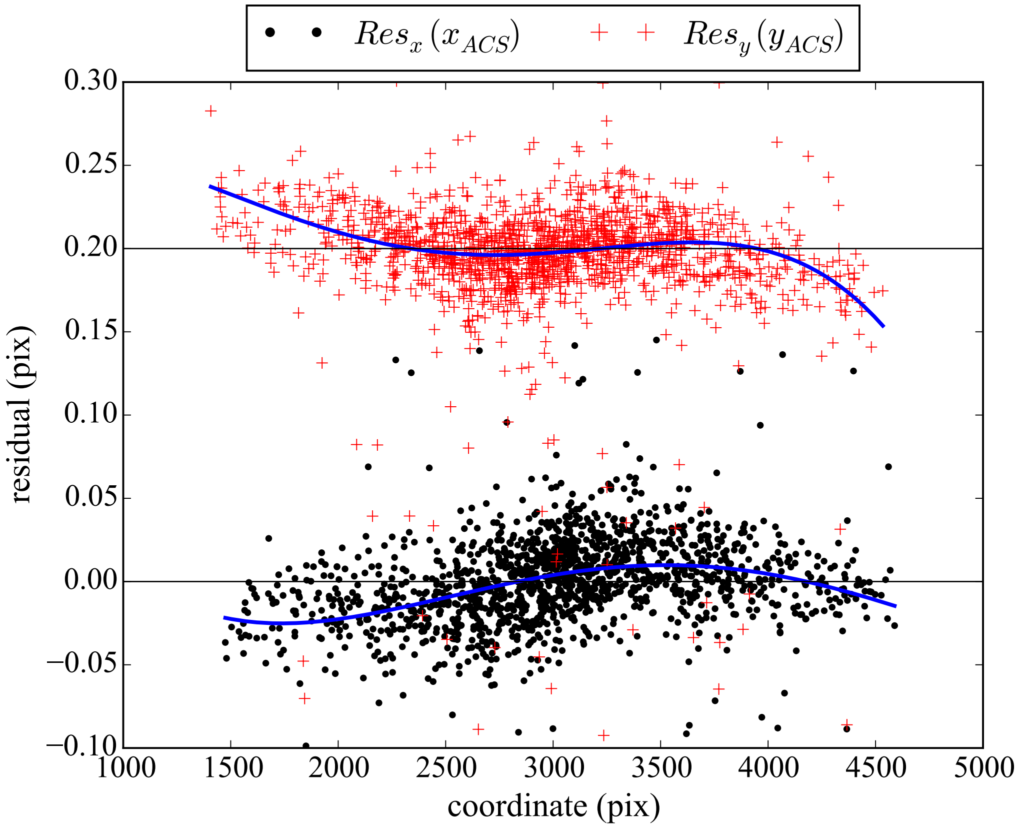

Figure 2.4: Coordinate transformation residuals obtained with `ccmap`, which correspond to the mapping of the final NGC 6717 WFC3 catalog into the ACS coordinate catalog. Black points and red crosses show the residual in X as a function of reference X coordinate and the residual in Y as a function of reference Y coordinate, respectively. Note the residual dependence as a function of ACS pixel coordinates. This is caused by residual CTE systematics and the remaining CTE effects within the ACS catalog. The solid blue lines show a 4th-degree polynomial fit to the residuals. The residuals in Y have been shifted for clarity.

and, therefore, we use this new sample to recalculate the solution using the same procedure as explained above. If we therefore assume that we are transforming coordinates for cluster members only, hence not including non-members with high proper motions, then the best accuracy we can achieve is determined by the intrinsic instrumental uncertainty found when constructing the WFC3 master catalog. This is indeed the case, as can be seen in Figure 2.4, where we confirm that the dispersion is about the same as in Figure 2.3. We then fit a 4th-degree polynomial to the residuals and use it to correct for small lower-frequency systematics, which are still remaining in the transformation, likely caused by CTE effects that were not completely erased. This results in symmetric residuals independent of the physical coordinates on the camera detectors. This is illustrated in Figure 2.5, which demonstrates that we now have every WFC3 master catalog mapped into the ACS coordinate frame with an average uncertainty of $\sim 0.02 - 0.03$ pix.

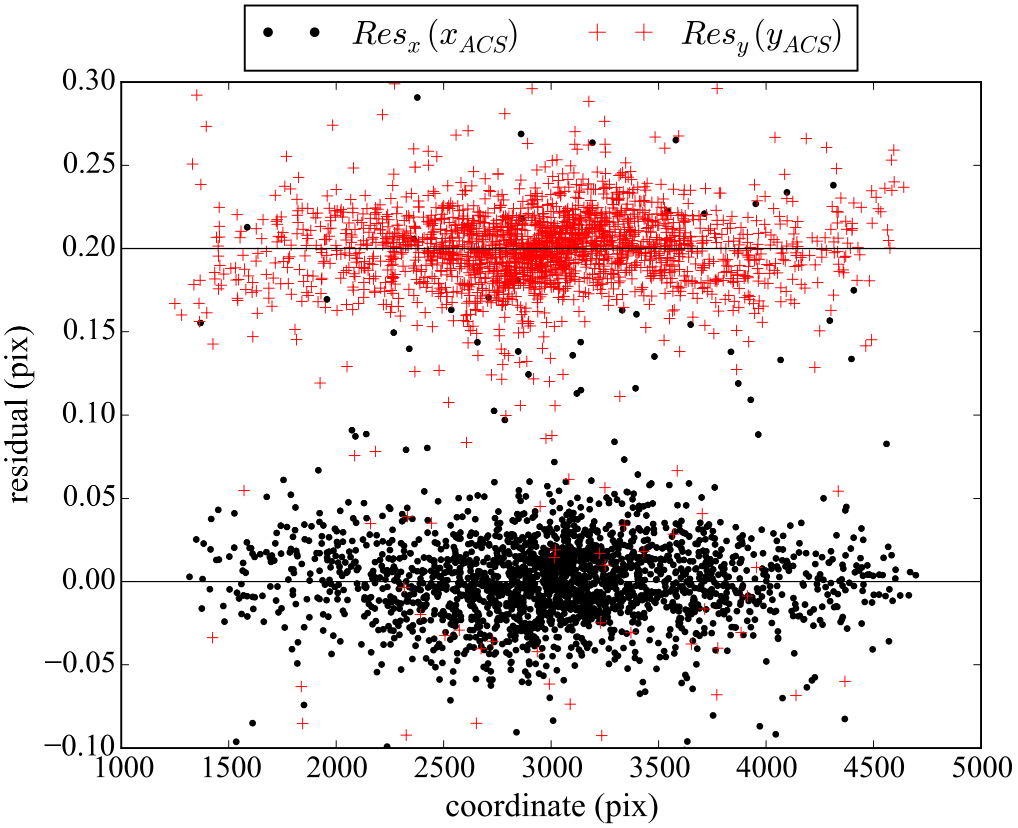

Figure 2.5: Same as Fig. 2.4 after correcting for the polynomial fits from Fig. 2.4.

2.3.3 Second Source Detection in WFC3 frames

The WFC3 master catalog coordinates are of the best accuracy we can obtain. This is because we use the positions of detected sources in every F336W frame that is available, i.e. we require a detection to be present in all F336W frames of a given target field. However, this inevitably leads us to miss any star that happens to fall within the chip gap in any given exposure, even when this same star is detected in all other exposures of the same target field, not to mention failed detections due to source overlap with cosmic rays, bad pixels, and detector artifacts. This is why we choose to perform a second detection procedure using now an $N-1$ detection condition, where N corresponds to the number of available F336W sub-exposures for a given target cluster. For most GCs, we have at least four available sub-exposures, except for NGC 6341 and NGC 6366, where only two F336W frames are available for photometry. For these two GCs we do not perform the second selection and coordinate measurement. For all the other GCs in our sample, we obtain new catalogs based on this new procedure, and redo the steps described in this section above in order to obtain new coordinate measurements, which will be of slightly lower accuracy than the ones previously measured with the full set of frames, as there is one less data point to measure the average position of each star in a given target field. This new catalog is combined with the original catalog in the sense that only sources that were not included before will get added, hence not affecting the astrometry of starts that were already measured. This method allows us to augment our proper-motion catalogs by $\sim 30 - 50\%$.

2.3.4 Proper-Motion Vector Diagrams

We use the catalogs obtained above and perform a source cross-match against the ACS reference frame using a matching tolerance of one pixel. This procedure automatically removes from our final catalog all stars with proper motions larger than one pixel, which is acceptable given that those will most likely be foreground field stars, since the GC proper motions are expected to be significantly smaller. We now define the relative proper motion values as:

$$\delta_x = X_{\mathrm{WFC3}} - X_{\mathrm{ACS}} \quad \text{and} \quad \delta_y = Y_{\mathrm{WFC3}} - Y_{\mathrm{ACS}}$$

and obtain relative proper motions in pixel units for every matched stellar source in the catalogs. We construct vector point diagrams by plotting δ_x against δ_y for every cluster in our sample, which are shown in Figure 2.6 for every sample GC. The cluster members scatter around the zero value by construction, as our method defines the GC proper motion as the reference. Note also that the chosen frame of reference, i.e. the ACS Globular Cluster Survey catalogs, are constructed to have x coordinates aligned with the right ascension (Ra) axis, and the y coordinates aligned with the declination (Dec) axis, which of course serves nicely to obtain proper motion values in the standard axis of Ra and Dec.

We use the proper motion information to select cluster members by studying the vector point diagram of stars at different luminosities. The underlying assumption is that more luminous (more massive) stars have, on average, different proper motions relative to less luminous stars. In particular, one expects from energy equipartition that more luminous stars have lower velocity dispersion than lower luminosity stars. Because of this, one needs to study the vector point diagram at different luminosity ranges. We divide each of the clusters catalog into four magnitude bins across the range of F606W magnitudes and construct their corresponding vector point diagrams (see Figure 2.6). For each subsample, we find an adequate selection criterion based on the observed dispersion of the vector point diagram. Because of the presence of very high proper motion stars, the measured dispersion can be unreliable, if measured directly, and therefore a more robust method must be applied in order to probe the true dispersion of the cluster stars. We choose to proceed as follows:

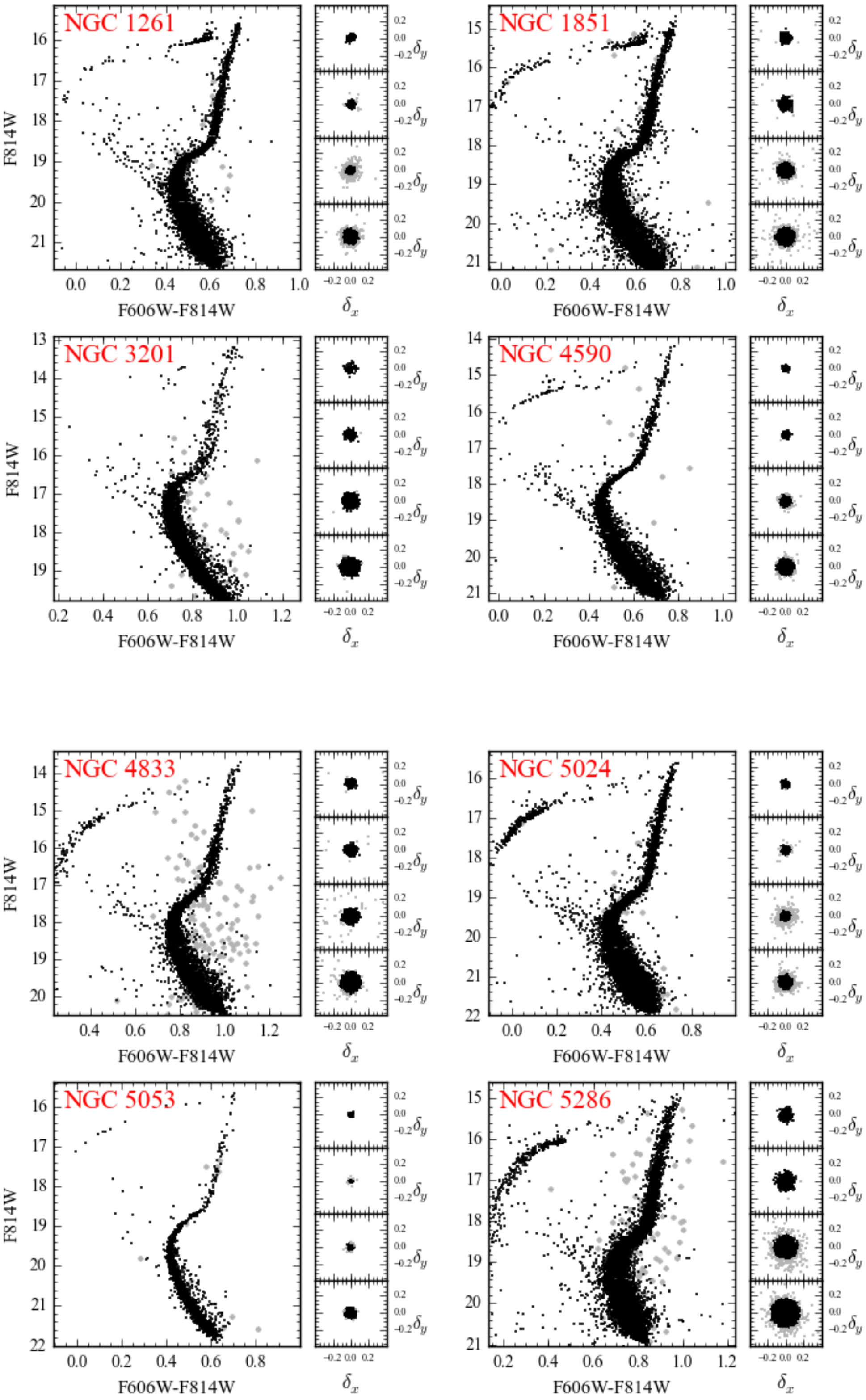

Figure 2.6: Color magnitude diagrams (CMDs) and relative proper motion distributions for our sample GCs. The vector point diagrams are shown in the smaller panels for four different magnitude ranges. Black points mark cluster member stars and grey points are non-members.

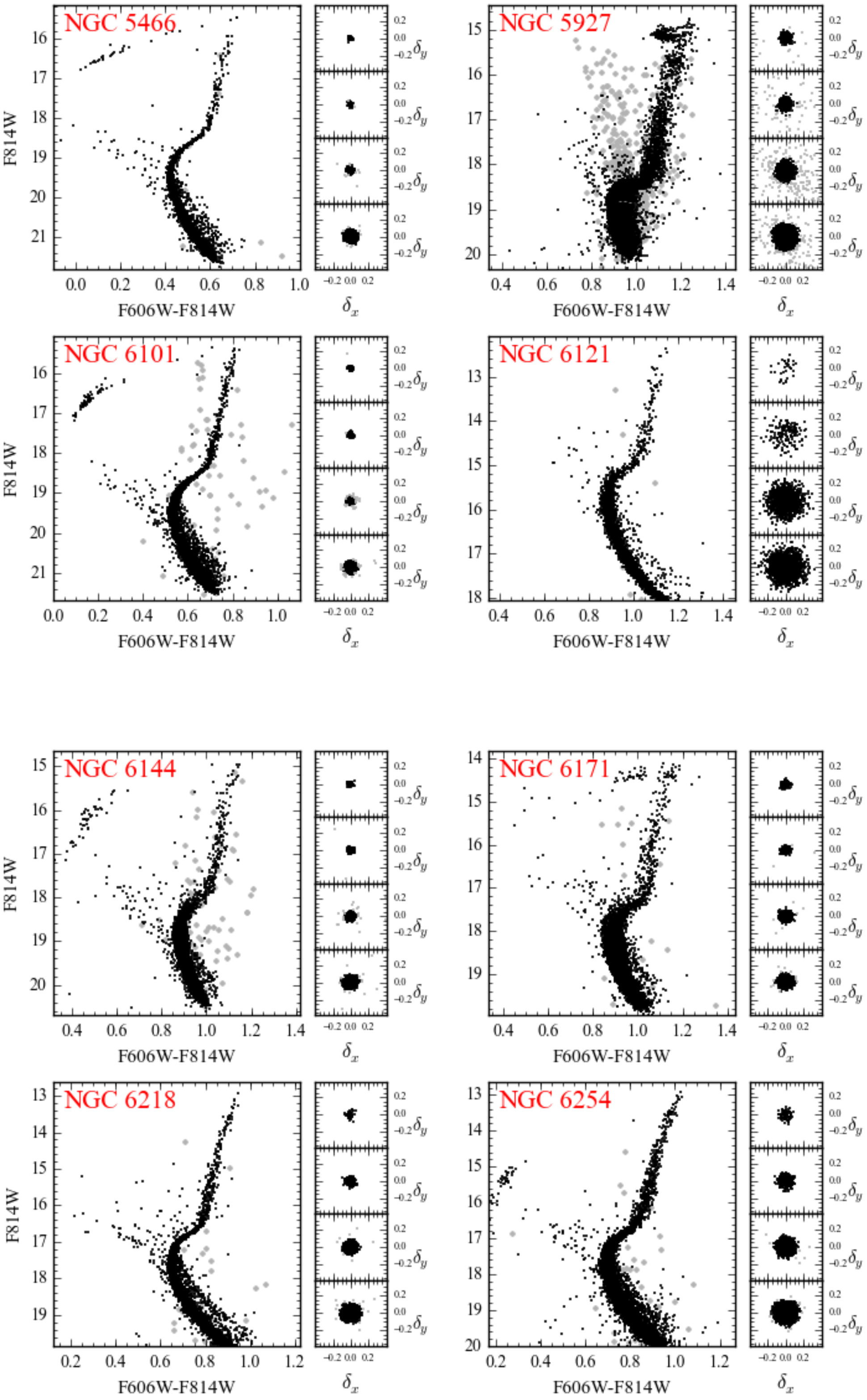

Figure 2.6: continued

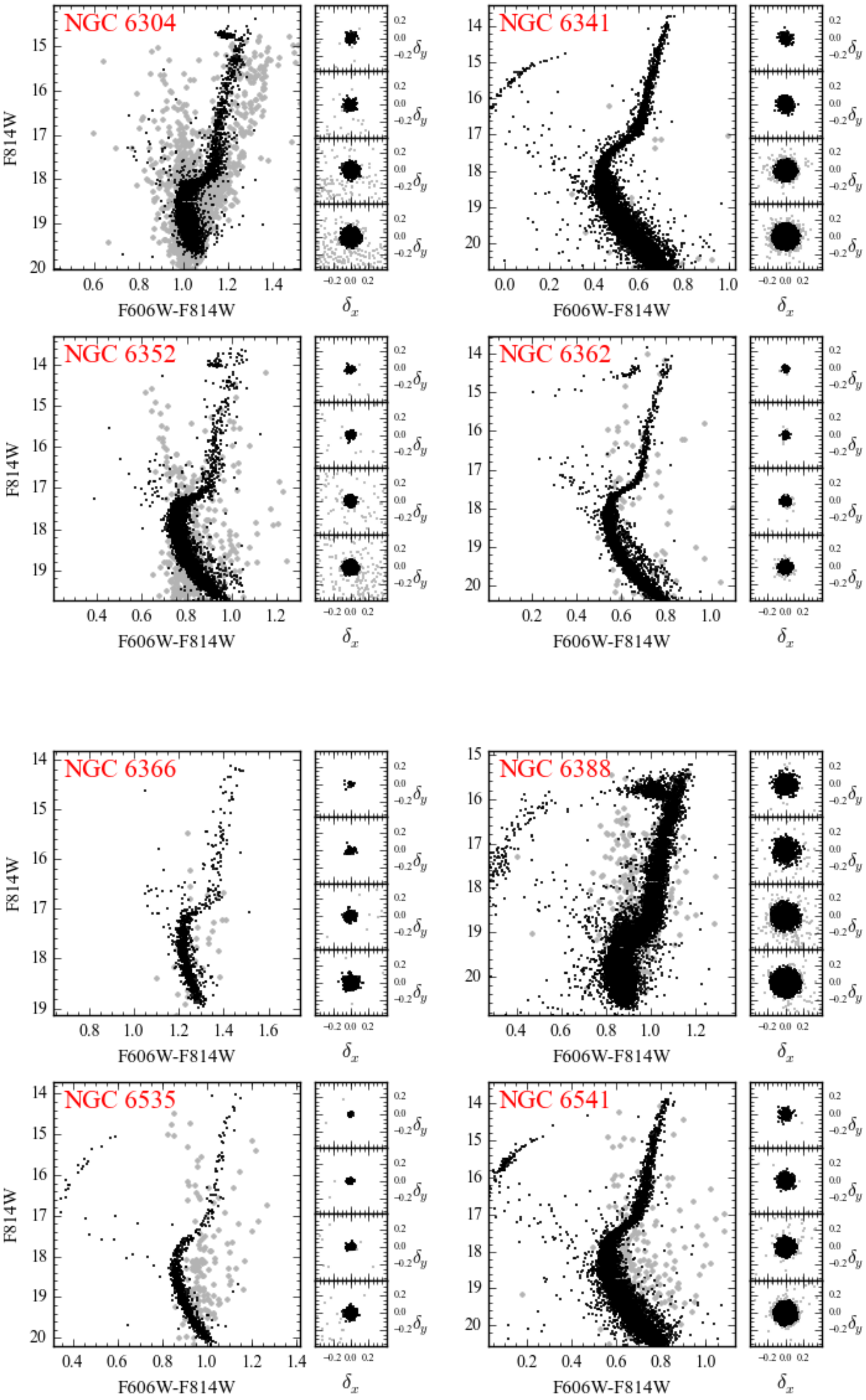

Figure 2.6: continued

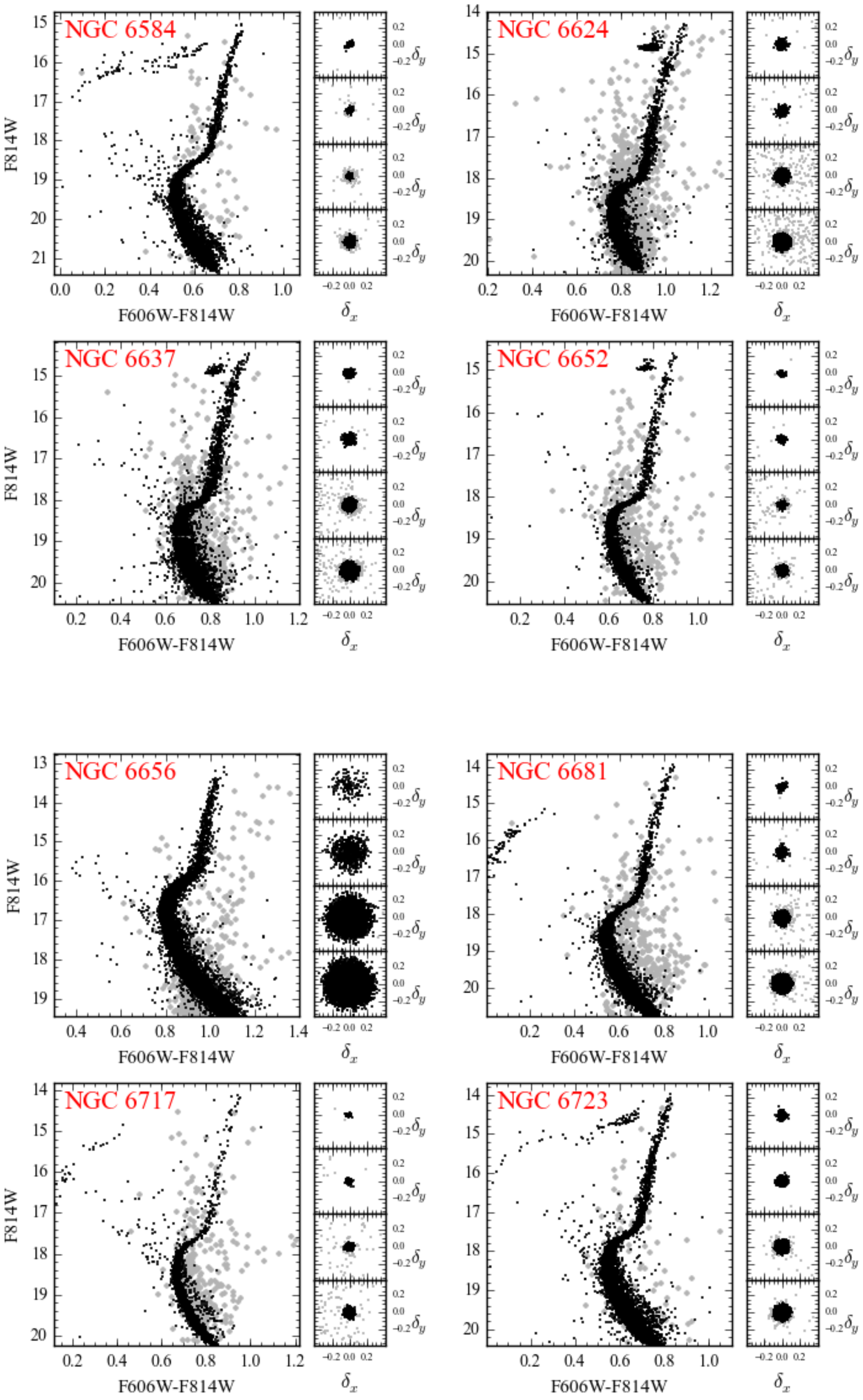

Figure 2.6: continued

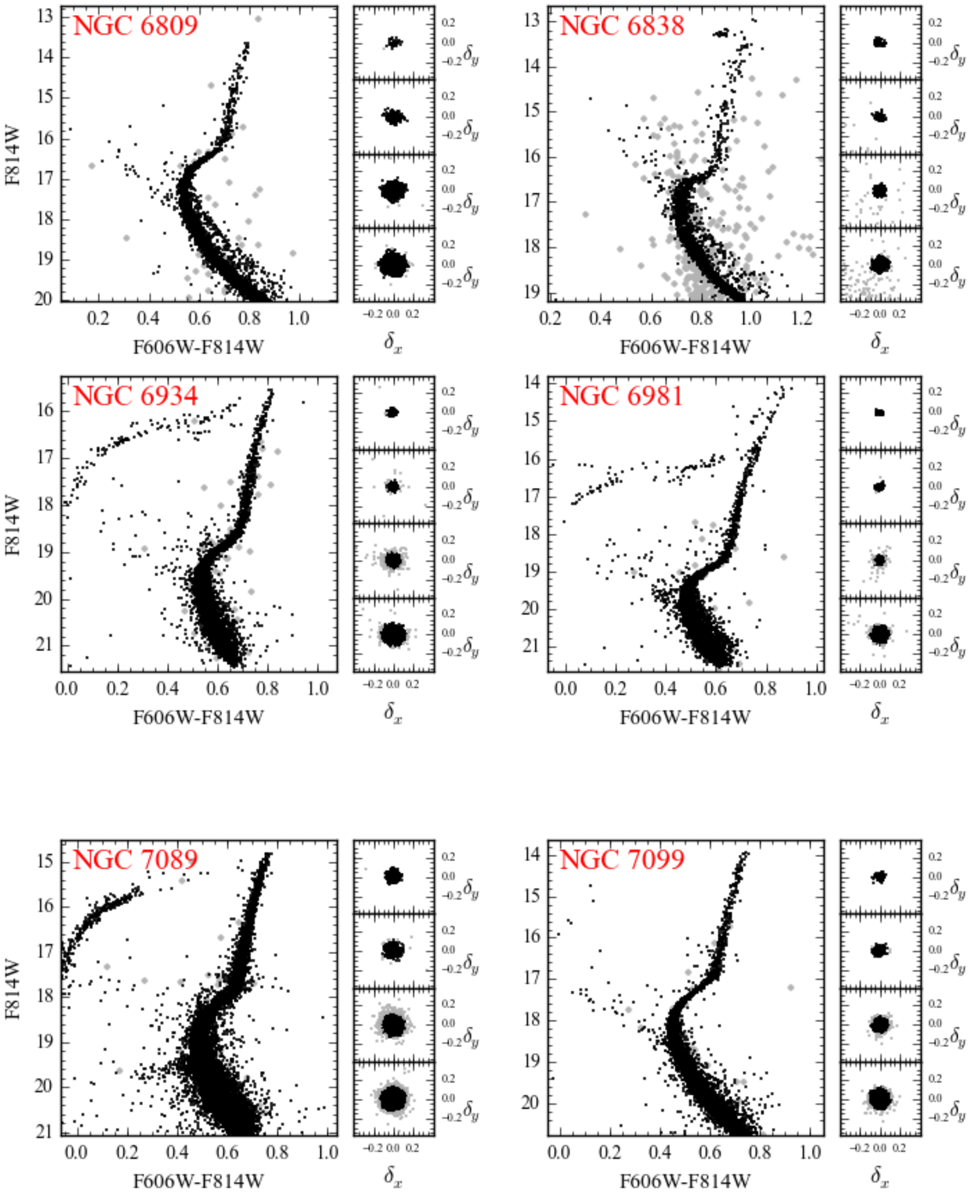

Figure 2.6: continued

1. We select stars with $R = \sqrt{\delta_x^2 + \delta_y^2} < 0.4$ pixels and calculate the standard deviation of R for the particular subsample.
2. We remove stars with R larger than 4.5σ and recalculate the standard deviation.
3. We iterate the process until the standard deviation changes by less than 4%. This usually takes 3-4 iterations.
4. We classify stars as cluster members which have $R < 6.5\sigma$.

It is important to note that when changing the threshold of the selection criterion, the stars inside the classical BSS region do not experience any significant fluctuations in their membership fraction (except for GCs with high contamination above the sub-giant branch). This reduces the possibility of accidentally removing BSSs with relative high proper motions values, which is very important since we do expect them to exist from dynamical interactions involving binaries. Figure 2.6 shows the CMDs of cluster member and non-member stars along with their vector point diagrams for every of our sample GCs.

The CMDs show that our proper-motion decontamination is very efficient at removing the scatter in the diagrams, whether it is due to noisy photometry or actual foreground/background star removal. Most notoriously, the proper-motion cleaning is able to successfully remove the stars usually contaminating the region above the sub-giant-branch (SGB). These objects are considered likely disk stars and are sometimes referred to as the "blue plume". This is very evidently shown for example in the CMDs of NGC 5927, NGC 6304 and NGC 6652 (see Figure 2.6). Our proper-motion cleaning method facilitates, therefore, a pure selection of a rich sample of BSSs in the classical CMD region, i.e. brighter and bluer than the cluster main-sequence turn-off (MSTO) point, as well as above the SGB, where most previous studies usually failed to select BSSs, due to the significant field star contamination.

2.4 Analysis

2.4.1 Understanding the Errors

It is important to test the posterior accuracy of our proper-motion measurements and their reliability when trying to associate these measurements to real dynamical information. The first instrumental error that we introduce to our measurements stems from the WFC3 master catalog, described in Section 2.3.1. We calculate the average coordinates from multiple sub-exposures for each GC, and the final star coordinates in the WFC3 master catalogs are expected to carry an error caused partly by the motion of stars in the time span between the individual sub-exposures (up to ∼10 months for a few clusters). However, this is likely a negligible effect as we expect *(i)* these motions to be intrinsically less than[3] 0.006 pix, and *(ii)* the minimum measurable proper-motion vector to be defined by much larger instrumental limitations (i.e. the camera spatial resolution, the focus drift of each observation, etc.; see also Kozhurina-Platais & Anderson, 2015).

We show in Figure 2.7 the positional error distributions in the X and Y coordinates of the WFC3 catalogs for all GCs in our sample. The errors are calculated by taking the standard deviation of the different position measurements for stars down to one magnitude fainter than the MSTO in each cluster field. The figure shows that the measured coordinate uncertainty is on average about 0.015 pixels for WFC3 coordinates, although we must note that the peak of the error distribution is a value $\sim 20-30\%$ smaller, but the long tail due to the more abundant faint main-sequence stars causes the average value to increase significantly. We still adopt the mean as a representative error to be as conservative as possible. This uncertainty in the position of each star is the fundamental lower limit in our analysis and is inevitably carried over into the transformed coordinates in the mapped catalogs described in Section 2.3.2. Considering the difference in pixel size between ACS/WFC (0.05"/pix) and WFC3/UVIS (0.04"/pix), we expect the measured positions and proper motions in the ACS frame coordinates to have, in general, an inherent error of about 0.01-0.02 pixels. This uncertainty has an impact on our proper motion measurements depending on the cluster distance and the projected motions of stars, i.e. for more distant clusters the mapping error becomes increasingly more dominant compared to the smaller stellar proper motions. This is best seen in Figure 2.8 where the black lines show the expected proper motion dispersion as measured in ACS pixel units, as a function of distance, assuming four different velocity dispersions and a time baseline of seven years. We also show explicitly the average position error (see Figure 2.7) in ACS pixel units for each of our target sample GCs as a function of distance. The color shading of the symbols encodes the expected velocity dispersion value (see Section 2.4.2). The black lines hence illustrate the maximum position error allowed to robustly measure the corresponding velocity dispersion value in a GC. For example, the GCs that in the diagram lie above their corresponding maximum error, for a given velocity dispersion, would most likely show a larger proper motion dispersion than what is expected. This can be directly tested by estimating the central velocity dispersion for our cluster sample based on the measured proper motion dispersions.

---

[3] This assumes an average 0.3 mas/yr GC velocity dispersion (Watkins et al., 2015a), considering the time span between exposures and the ACS pixel size.

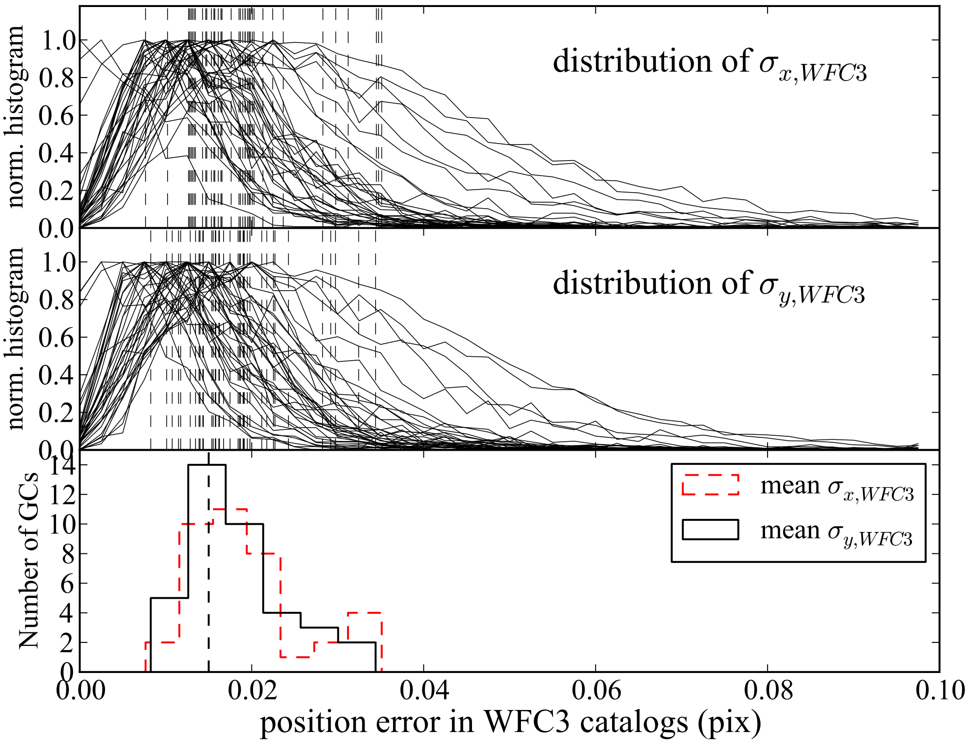

Figure 2.7: Normalized distributions of the standard deviation of different WFC3 coordinates of the cross-matched sources, when combining all different sub-exposure catalogs. The distributions are shown for the standard deviation of X and Y coordinates (top and middle panels, respectively) in every cluster of our sample, for stars down to one magnitude below the MSTO (i.e. each GC corresponds to a different solid line). The dashed vertical lines show the mean of the distribution for each GC catalog. The bottom panel shows the histogram of the mean σ_x (red dashed line) and σ_y (solid black line) for the GC sample. The vertical dashed line shows the value 0.015 pix, which is the typical mean error in WFC3 coordinates.

2.4.2 Comparison with Literature Values

For the GCs in our sample we plot in the left panel of Figure 2.9 the dispersion of R (σ_R) from all member stars down to luminosities one magnitude fainter than the MSTO within 10″ from the cluster center (representing the 2-D central velocity dispersion $\sigma_R = \sigma_0\sqrt{2/3}$) versus the expected $\sigma_{\mathrm{R},\star}$ based on the GC luminosity via

$$\sigma_{\mathrm{R},\star} = \sqrt{\frac{\mathcal{M}_\star G}{\beta r_h}},$$

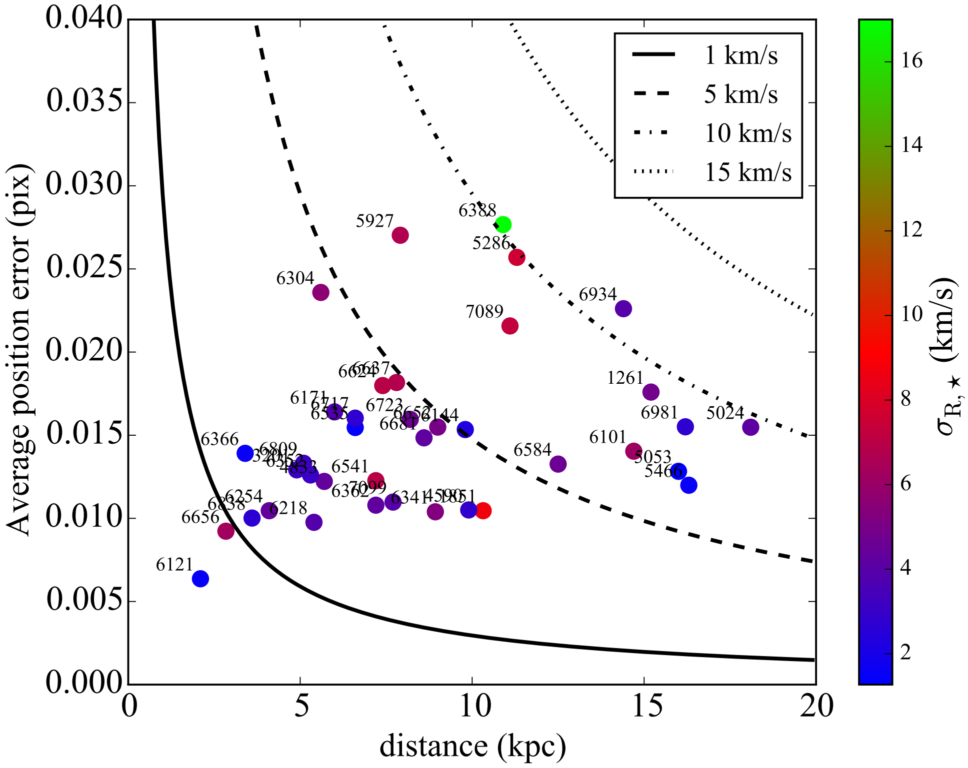

Figure 2.8: Average position error (see Figure 2.7) in ACS pixel units for each of our target sample GCs as a function of the literature distance values from Section 2.4.2. The color shading of the symbols encodes the expected central velocity dispersion ($\sigma_{\mathrm{R},\star}$) described in Section 2.4.2 for each GC. The black curves show the expected proper-motion dispersion value as a function of distance for stellar systems with four different central velocity dispersions. These lines represent the maximum allowed errors to robustly measure the corresponding central velocity dispersion value in a GC (see legend). We calculate these relations assuming a seven-year time baseline.

where $\mathcal{M}_\star$ is the GC stellar mass[4], r_h the GC half-light radius, and β the dynamical scaling parameter, for which we adopt $\beta = 12$ which is generally used for compact stellar systems (see Cappellari et al., 2006, for details).

We transform the projected motions to velocities assuming a seven year time span and the cluster distances given by Watkins et al. (2015b), or by Harris (2010) for those clusters that are not in the former catalog. We find that most of our estimates show a general agreement with the expected values. However, as it was predicted, for the cases where the position error from Figure 2.8 becomes significantly larger than the expected proper motion dispersion, we obtain a systematic overestimation of the velocity dispersion, as it is clearly seen in the GCs with large error bars. The symbols gray

---

[4] The stellar masses were computed from the V-band mass-to-light ratios from the SSP model predictions of Bruzual & Charlot (2003), which were computed for each corresponding GC metallicity assuming a stellar population age of 12 Gyr. The absolute V-band magnitudes and metallicities were taken from Harris (2010).

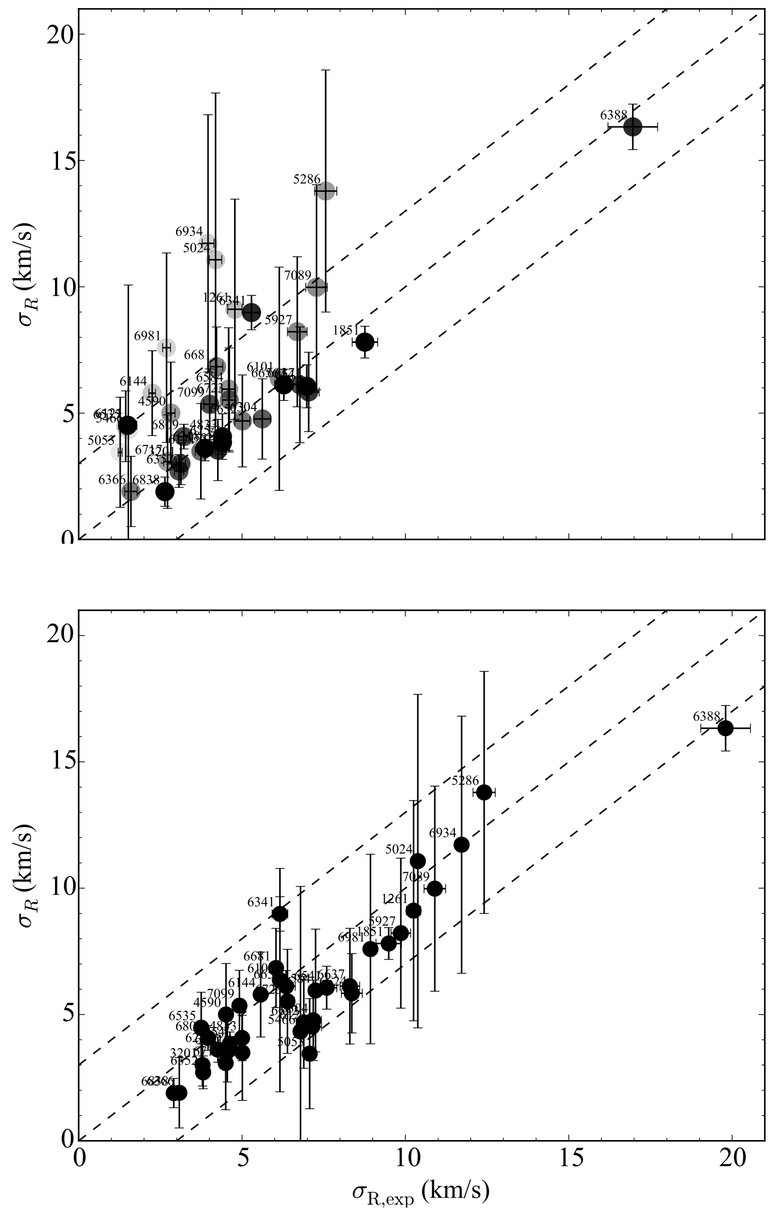

Figure 2.9: *Top*: Central velocity dispersion estimates from our proper-motion analysis (σ_{R}) as a function of the expected velocity dispersion values ($\sigma_{\mathrm{R},\star}$) from photometric considerations (see Section 2.4.2). The error bars are calculated from the individual position errors of each star used in the dispersion estimate, while the errors of the expected values are calculated assuming a 0.1 mag uncertainty in the GC absolute magnitude. The symbol gray shading is scaled to the significance with which the expected velocity dispersion ($\sigma_{\mathrm{R},\star}$) would be measured for each GC given its average position error (see Figure 2.7). Therefore the lighter points with large error bars and systematically above the 1-to-1 relation correspond to GCs that have large mean position errors and are located at a relatively large distance, i.e. in the upper right region of Figure 2.8. *Bottom*: Central velocity dispersion estimates from our proper-motion analysis (σ_{R}) as a function of the expected *observed* velocity dispersion values ($\sigma_{\mathrm{R,exp}}$). The x-axis values are calculated as the combination of the intrinsic velocity dispersion ($\sigma_{\mathrm{R},\star}$) values plus the dispersion broadening coming from the individual GC proper motion errors. The dashed lines show the one-to-one relation as well as the ±3 km/s region which is representative of the scatter expected from the error bars shown.

shading are scaled to $\sigma_{\mathrm{R},\star}$ in pixel units divided by the mean instrumental error for each GC, which basically corresponds to the significance with which the expected velocity dispersion ($\sigma_{\mathrm{R},\star}$) would be measured for each GC given its average instrumental error. Therefore the lighter points show GCs in which the σ_R values should be more affected by the errors. In the right panel of Figure 2.9 we try to recover our measured σ_R, taking now into account how the instrumental errors would artificially broaden the intrinsic velocity dispersion. Hence, we sum in quadrature the average position measurement uncertainty (σ_{pos}) for each GC (see Fig. 2.7), and the $\sigma_{\mathrm{R},\star}$ values. This way we try to mimic an expected *observed*[5] velocity dispersion $\sigma^2_{\mathrm{R,exp}} = \sigma^2_{\mathrm{R},\star} + \sigma^2_{\mathrm{pos}}$. The plot shows good agreement, which means that our assumption that the overestimations in the σ_R values are dominated by the measured positional errors seems valid. This Figure nicely illustrates what considerations must be taken into account when interpreting our measurements, and what kind of accuracy we expect to achieve when comparing it to other similar measurements. Subsequently, we now compare our estimates with the values from the recent study of Watkins et al. (2015a), who homogeneously derived central velocity dispersion values from HST proper motions of stars down to luminosities one magnitude below the MSTO (i.e. the same adopted limit in our study) in 22 GCs, as part of the HSTPROMO collaboration (Bellini et al., 2014). We show the result of this comparison in Figure 2.10 for the ten clusters in common. All of these ten clusters populate a region in Figure 2.8 where we do not expect our measurements to be severely affected by the instrumental errors. Indeed, the Figure shows good agreement between both studies. The scatter is entirely consistent with individual GC measurement errors, which again confirms that we are correctly estimating our uncertainties. We note the case of NGC 7099, which shows a moderate discrepancy. Its position in Figure 2.8 (at ~ 7.5 kpc distance and ~ 0.01 pix average error) puts it slightly above its allowed maximum error for its expected central velocity dispersion ($\sigma_{R,\star} \approx 4$ km/s). This implies that our estimated velocity dispersion should be slightly affected by the measurement uncertainties and needs to be considered an upper limit. Indeed our estimate is $\sim$1 km/s larger than the expected value. Figure 2.10 then suggests that the value from Watkins et al. (2015a) is overestimated by at least 6 km/s. This is actually consistent with their results (see their Figure 13), which shows their estimate to be $\sim$7 km/s larger than previous studies. It is worth mentioning that NGC 7099 is actually the smallest data set from the entire cluster sample in their study, and hence the polynomial fit to their dispersion profile is the poorest out of their entire cluster sample. Considering the above, we conclude that a comparison between both measurements in NGC 7099 has to be taken with care. Nevertheless, the overall agreement with the Watkins et al. (2015a) study

---

[5] The reader should note that this quantity now differs from a realistic velocity dispersion, but is rather a direct attempt to reproduce our proper motion dispersion measurements, by taking into account how the errors would affect the real velocity dispersion.

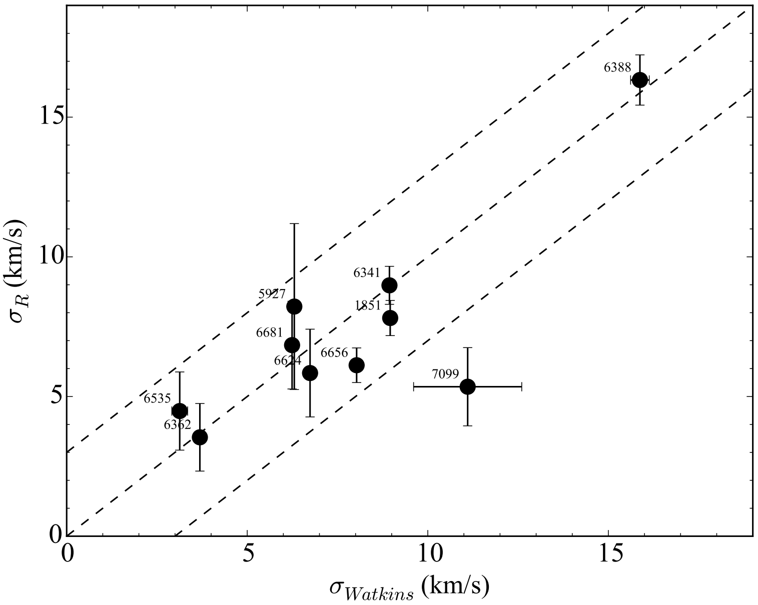

Figure 2.10: Central velocity dispersion estimates from our proper motion data compared to the ones from Watkins et al. (2015a). Their proper motion dispersion values are converted into velocities using the distances from Watkins et al. (2015b).

illustrates that accurate proper motions can be reproduced by different data analysis methods to a very high degree and can be, therefore, used to derive absolute physical properties of the observed GCs, such as dynamical masses. Hence we conclude that, within our expected measurement uncertainties, our proper motion analysis can be used to produce clean BSS catalogs.

2.4.3 Selection of BSS Candidates

We now have stellar catalogs of our sample GCs that are free from fore- and background field stars, which may contaminate the BSS region in the CMDs between the sub-giant branch and the horizontal branch (see Figure 2.11). This is mainly due to the young stellar populations of the Milky Way disk. The next step of the BSS selection process is to homogeneously define a BSS selection function that can be uniformly applied to the CMD of every GC.

We compute the ridge line (RL) of GC stars along the main sequence (MS), sub-giant branch (SGB) and red-giant branch (RGB) directly from the data. We determine the spread in F606W-F814W color around the RL at each F814W magnitude and use it to define a red limit for BSS selection. We define stars within 4.5σ around the RL to be members of the MS, SGB or RGB, while stars falling $> 4.5\sigma$ towards bluer colors are considered BSS candidates. This limits the selection of BSS candidates towards red colors. To set a limit towards bluer colors we then use Dartmouth isochrones (Dotter et

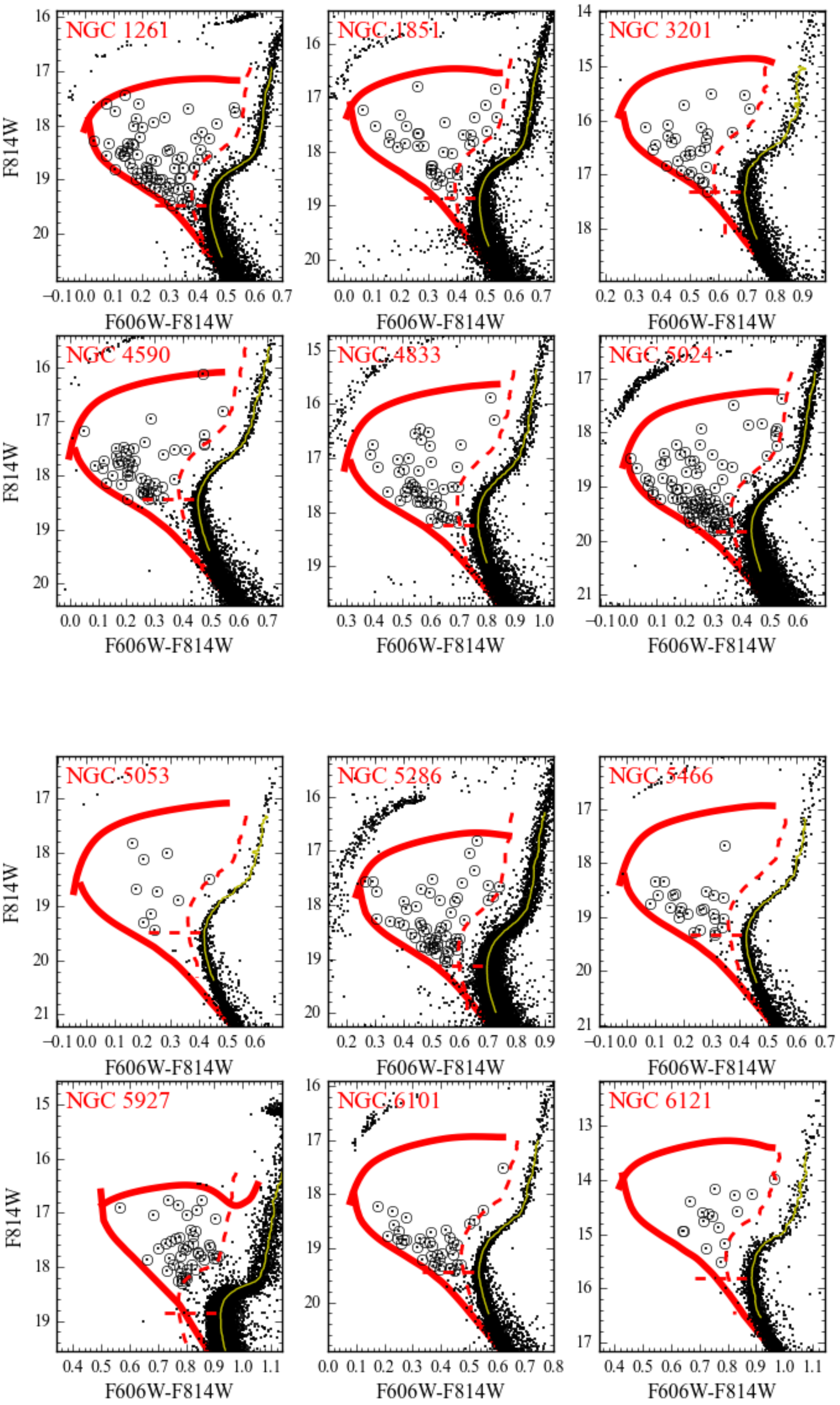

Figure 2.11: Color magnitude diagrams of our globular cluster sample. The selected BSSs are labeled as circles. The red thick lines mark the isochrone-based limits for the BSS selection region. The yellow solid line shows the FL and the red dashed line shows the FL-based red limit for the BSS selection region. The horizontal red dashed line marks the empirical MSTO, as measured from the FL.

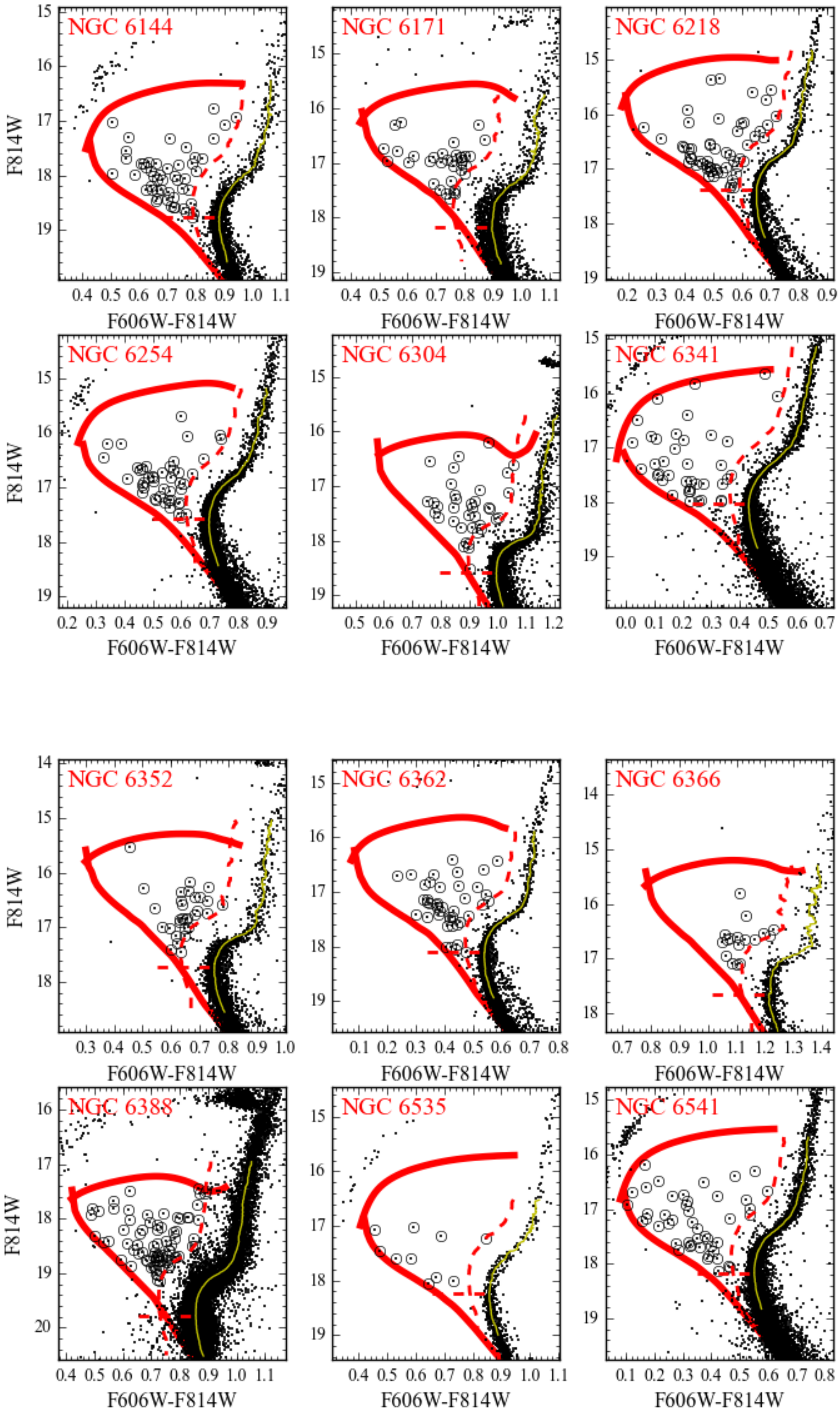

Figure 2.11: continued

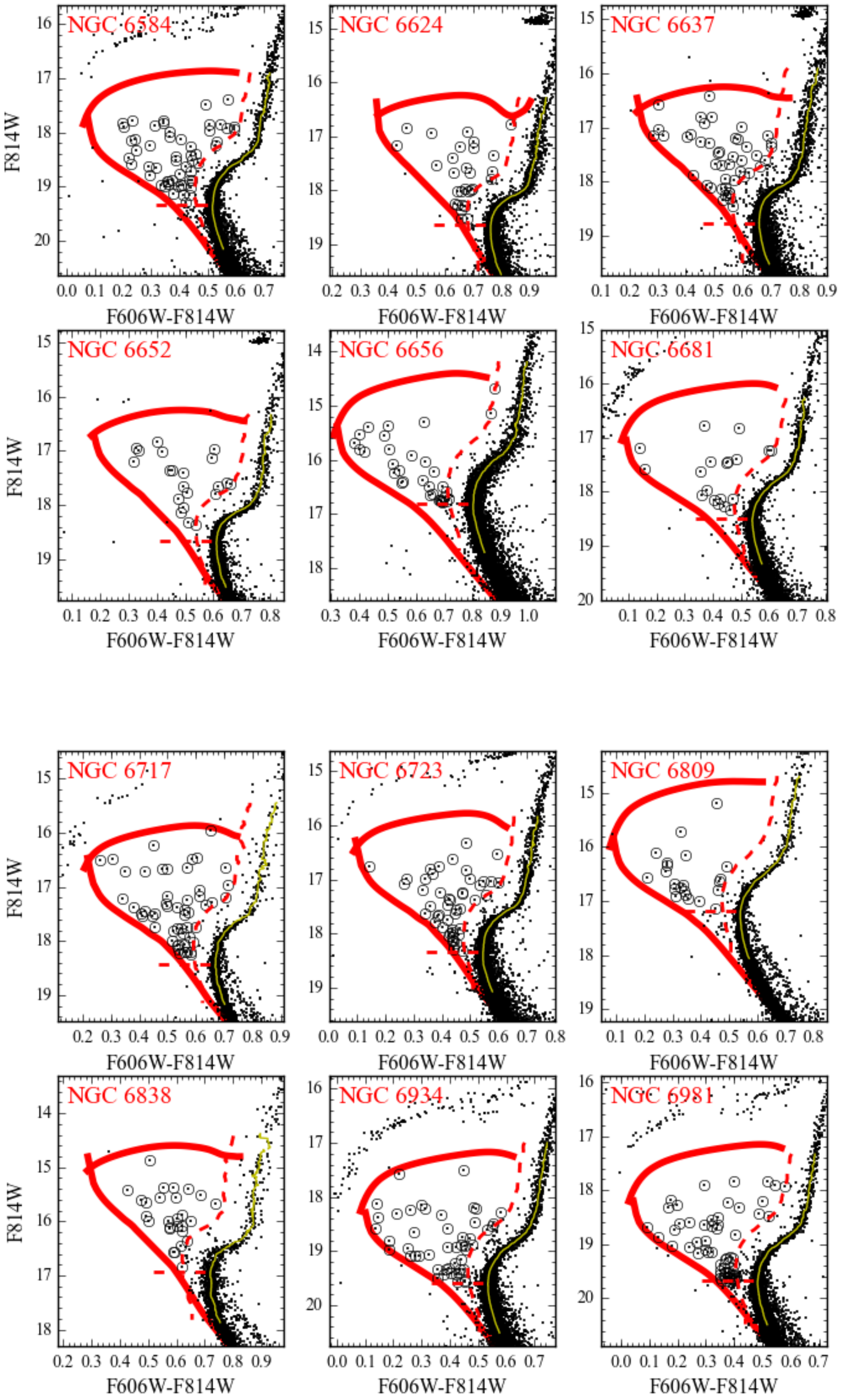

Figure 2.11: continued

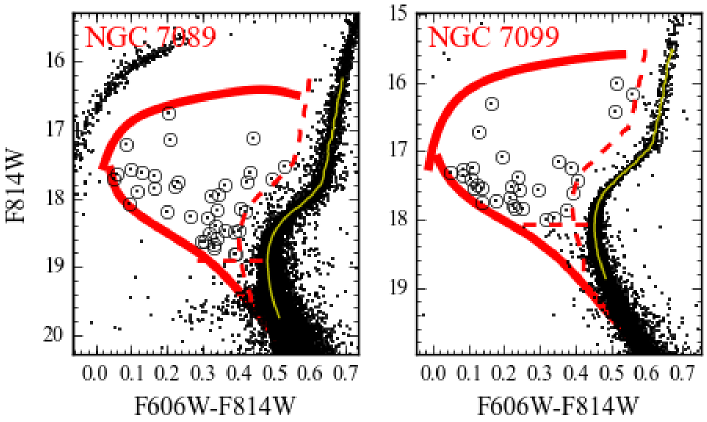

Figure 2.11: continued

al., 2008) with the GC stellar population parameters found by Dotter et al. (2010) or from the McMaster catalog (Harris, 2010) for GCs which are not listed in the former catalog. We use a 1-Gyr old isochrone at an α enhancement of 0.2 dex for all GCs to define the bluest limit for our BSS selection. For most GCs, such an isochrone intersects in its SGB part with portions of the horizontal branch (HB) GC stellar population. We, therefore, use a copy of the 1-Gyr isochrone which is shifted 1 mag to fainter luminosities to limit our BSS selection at the bright end. The combination of these three curve sections outlines a closed parameter space region in the F814W vs. F606W-F814W CMD and defines our BSS candidate selection function (see Figure 2.11). Additionally, we require for the selected BSSs to be brighter than the empirical MSTO magnitude, defined as the bluest point of the RL. We point out that previous works used similar HST data to derive their BSS catalogs (e.g. Leigh et al., 2011a), while restricting their chosen BSS selection criteria to the classic BSS sub-population. Their definitions were using semi-empirically chosen polygons in the corresponding CMDs that were motivated by earlier studies (de Marchi et al., 2006; Ferraro et al., 1997; Leigh et al., 2007) and were avoiding the so-called yellow straggler star sub-populations (e.g. Hesser et al., 1984; McGahee, 2014; McClure et al., 1985). Our definition is entirely data-based and includes the main BSS as well as the yellow straggler locus. We note that this CMD region is also commonly contaminated by young disk stars – a feature usually referred to as the blue plume. This is clearly seen for example in NGC 5927, NGC 6304, NGC 6352, NGC 6388, and NGC 6624 as the high concentration of grey points above the SGB (see Fig. 2.6). Our proper motion decontamination shows that most GCs have at least some contamination in this region. The BSS selection presented here can, therefore, safely include stars in this region. This is actually a critical point for measurements such as the BSS fraction. In a recent paper, Salinas et al. (2016) showed that previous claims of M 80 having a notably large BSS fraction were most likely affected by a severe contamination of such young disk stars and/or blends. Their results actually put the BSS fraction of M 80 at a normal value for GCs. We highlight the importance of the stars red of the classical BSS locus because possible interpretations for their existence may include: (i) the possibility of them being evolved BSSs, i.e. older BSSs that are currently evolving through the Hertzsprung gap, and (ii) the possibility that they are recent collision products in the process of contracting back down to the ZAMS, i.e. extremely young BSSs.

2.4.4 Potential contaminants in the BSS sample

We need to consider the possibility of remnant contaminants that passed our selection function. Foreground and background stars are effectively removed by the proper motion technique, therefore they can be safely considered non-existent in our sample. The possibility of star blends deserves some discussion. For example, random alignments between very hot stars, e.g. blue horizontal branch stars (BHBs), and cooler stars can easily mimic optical BSS colours. This is indeed very problematic for BSS selection with ground-based seeing-limited imaging data. For this reason, early HST studies (Ferraro et al., 1997) combined near-UV and optical imaging to exclude such contaminants. In purely optical CMDs, such blends between BHB+cooler stars (i.e. MSTO, SGB, and RGB stars), can fall in the classical BSS and yellow straggler locus. Blends between MSTO and SGB/RGB stars preferentially populate the yellow straggler region (Salinas et al., 2016, see their Figure 8). Since BSSs are truly hotter SEDs than MSTO/SGB/RGB blends, combining near-UV+ optical imaging will effectively identify such blends and select only genuine BSSs with the appropriate near-UV flux and near-UV+optical color. Blends between BHB+cooler stars are distinguished by their significantly bluer near-UV+optical colors than genuine BSSs. In our study, the fact that proper motions are derived from combined near-UV-optical data, already mitigates this issue. In particular, in the scenario of stellar blends with different temperature components, the measured centroids can easily be influenced differently when seen in the near-UV or in the optical. Given the approximate FWHM size of ACS ($\sim 2-3$ pixels), any chance alignment of stars at smaller distances would either get rejected by our initial QFIT threshold filtering (due to the imperfect PSF fitting in such cases) or by the proper-motion selection itself, as such blends will likely be cataloged as high-proper motion stars (considering that our typical maximum proper motion is $\sim$0.1$-$0.2 pixels for selected members, see Figure 2.6). We still consider the possibility that blends might contaminate our BSS sample, and hence we have built F336W-F814W CMDs and directly inspected all BSS samples. We found a very small amount ($\sim 10 - 20$ in our entire BSS library) of potential BHB/MSTO/SGB/RGB blends based on their position in these near-UV+optical CMDs and have flagged and removed them from the samples. Such low contamination fractions demonstrate the power of proper-motion based BSS selection functions and reassure the purity of our final BSS sample.

2.4.5 Proper Motion Cleaned BSS Catalogs

The result of this work are proper motion cleaned, homogeneously selected, HST photometric catalogs of BSSs in the inner $\sim 3' \times 3'$ of 38 Milky Way GCs (see Table 2.1). In Table 2.2, we provide the location, photometry, and proper motions for the first 30 BSSs candidates in NGC 1261. For completeness, the proper motion values have been converted to mas/yr units, assuming a 7 year baseline and the ACS/WFC pixel size (0.05"/pix). The full list of catalogs for each of our sample GCs is available electronically and can also be obtained via this web link[6].

2.5 Summary

We present a comprehensive proper-motion analysis based on Hubble Space Telescope (HST) observations of 38 Galactic GCs obtained by two public treasury surveys (" *The ACS Globular Cluster Survey*", GO-10775 and " *The HST Legacy Survey of Galactic Globular Clusters: Shedding UV Light on Their Populations and Formation*", GO-13297). We used WFC3/UVIS imaging data and apply the reduction routines developed by the STScI in order to derive precise astrometric catalogs of the inner $\sim 3' \times 3'$ GC regions. We combine those catalogs with calibrated ACS photometric catalogs and use these data to measure precise relative proper motions of stars in our sample GCs and perform a subsequent cluster membership selection. We study the accuracy of our proper motion measurements using estimates of the central velocity dispersion in each of our clusters and find very good agreement with previous similar studies in the literature. Finally, we construct homogeneously defined BSS selection criteria in order to derive proper-motion cleaned BSS catalogs in all 38 GCs. The proper motion decontamination allows the unambiguous selection of yellow stragglers in the CMD, which had been previously not possible in most of the past BSS studies given the high field star contamination in those CMD regions. These BSS catalogs and their proper motion information can be used to study the dynamical state of BSSs in general and put them in the context of the GC dynamical evolution. The results from these studies will be presented in Chapter 3.

---

[6] http://www.astro.puc.cl/~msimunov/research.html

Table 2.1: Properties of the target GC sample. Columns 1-7 were taken from Harris (2010). Column 8 is the calculated expected central velocity dispersion described in Section 2.4.2.

NGC	Name	RA(J2000) [hr:min:sec]	DEC(J2000) [deg:min:sec]	[Fe/H] [dex]	$M_{\rm V}$ [mag]	r_h [arcmin]	$\sigma_{\rm R,\star}$ [km/s]
NGC 1261		03:12:16.21	−55:12:58.4	−1.27	−7.80	0.68	4.78 ± 0.23
NGC 1851		05:14:06.76	−40:02:47.6	−1.18	−8.33	0.51	8.76 ± 0.41
NGC 3201		10:17:36.82	−46:24:44.9	−1.59	−7.45	3.10	3.13 ± 0.15
NGC 4590	M 68	12:39:27.98	−26:44:38.6	−2.23	−7.37	1.51	2.82 ± 0.13
NGC 4833		12:59:33.92	−70:52:35.4	−1.85	−8.17	2.41	4.40 ± 0.21
NGC 5024	M 53	13:12:55.25	+18:10:05.4	−2.10	−8.71	1.31	4.19 ± 0.20
NGC 5053		13:16:27.09	+17:42:00.9	−2.27	−6.76	2.61	1.27 ± 0.06
NGC 5286		13:46:26.81	−51:22:27.3	−1.69	−8.74	0.73	7.56 ± 0.36
NGC 5466		14:05:27.29	+28:32:04.0	−1.98	−6.98	2.30	1.52 ± 0.07
NGC 5927		15:28:00.69	−50:40:22.9	−0.49	−7.81	1.10	6.69 ± 0.32
NGC 6121	M 4	16:23:35.22	−26:31:32.7	−1.16	−7.19	4.33	1.50 ± 0.07
NGC 6101		16:25:48.12	−72:12:07.9	−1.98	−6.94	1.05	6.14 ± 0.29
NGC 6144		16:27:13.86	−26:01:24.6	−1.76	−6.85	1.63	2.25 ± 0.11
NGC 6171	M 107	16:32:31.86	−13:03:13.6	−1.02	−7.12	1.73	3.74 ± 0.18
NGC 6218	M 12	16:47:14.18	−01:56:54.7	−1.37	−7.31	1.77	3.87 ± 0.18
NGC 6254	M 10	16:57:09.05	−04:06:01.1	−1.56	−7.48	1.95	4.40 ± 0.21
NGC 6304		17:14:32.25	−29:27:43.3	−0.45	−7.30	1.42	5.62 ± 0.26
NGC 6341	M 92	17:17:07.39	+43:08:09.4	−2.31	−8.21	1.02	5.29 ± 0.25
NGC 6352		17:25:29.11	−48:25:19.8	−0.64	−6.47	2.05	3.07 ± 0.14
NGC 6366		17:27:44.24	−05:04:47.5	−0.59	−5.74	2.92	1.60 ± 0.08
NGC 6362		17:31:54.99	−67:02:54.0	−0.99	−6.95	2.05	4.26 ± 0.20
NGC 6388		17:36:17.23	−44:44:07.8	−0.55	−9.41	0.52	16.96 ± 0.8
NGC 6535		18:03:50.51	−00:17:51.5	−1.79	−4.75	0.85	1.44 ± 0.07
NGC 6541		18:08:02.36	−43:42:53.6	−1.81	−8.52	1.06	6.98 ± 0.33
NGC 6584		18:18:37.60	−52:12:56.8	−1.50	−7.69	0.73	4.59 ± 0.22
NGC 6624		18:23:40.51	−30:21:39.7	−0.44	−7.49	0.82	7.04 ± 0.33
NGC 6637	M 69	18:31:23.10	−32:20:53.1	−0.64	−7.64	0.84	6.77 ± 0.32
NGC 6652		18:35:45.63	−32:59:26.6	−0.81	−6.66	0.48	5.01 ± 0.24
NGC 6656	M 22	18:36:23.94	−23:54:17.1	−1.70	−8.50	3.36	6.28 ± 0.30
NGC 6681	M 70	18:43:12.76	−32:17:31.6	−1.62	−7.12	0.71	4.22 ± 0.20
NGC 6717	Pal 9	18:55:06.04	−22:42:05.3	−1.26	−5.66	0.68	2.72 ± 0.13
NGC 6723		18:59:33.15	−36:37:56.1	−1.10	−7.83	1.53	4.61 ± 0.22
NGC 6809	M 55	19:39:59.71	−30:57:53.1	−1.94	−7.57	2.83	3.22 ± 0.15
NGC 6838	M 71	19:53:46.49	+18:46:45.1	−0.78	−5.61	1.67	2.64 ± 0.12
NGC 6934		20:34:11.37	+07:24:16.1	−1.47	−7.45	0.69	3.96 ± 0.19
NGC 6981	M 72	20:53:27.70	−12:32:14.3	−1.42	−7.04	0.93	2.69 ± 0.13
NGC 7089	M 2	21:33:27.02	−00:49:23.7	−1.65	−9.03	1.06	7.28 ± 0.34
NGC 7099	M 30	21:40:22.12	−23:10:47.5	−2.27	−7.45	1.03	4.01 ± 0.19

Table 2.2: Properties of selected Blue Straggler Stars in NGC 1261. Columns 1-5 are taken from the original ACS catalogs from Sarajedini et al. (2007). Columns 6 and 7 correspond to the proper motion values in sky coordinates, taking into account the cos(Dec) correction. They have been converted to mas/yr units, assuming a 7-year baseline and the ACS/WFC pixel size (0.05"/pix).

ID	R.A. (J2000)	DEC (J2000)	$F606W$ [mag]	$F606W-F814W$ [mag]	μ_{RA}cos(Dec) [mas/yr]	μ_{Dec} [mas/yr]
25341	48.0822474	−55.2259794	18.285	0.53	−0.004	0.182
29884	48.0734013	−55.2210313	18.485	0.165	−0.043	−0.082
30687	48.0726997	−55.2208797	18.425	0.466	0.011	0.001
25466	48.0823863	−55.2190322	17.57	0.139	0.091	0.06
31914	48.0707694	−55.2174152	18.425	0.083	0.012	−0.039
65969	48.0761793	−55.2168233	18.468	0.147	0.013	0.003
70287	48.0693072	−55.2160585	18.531	0.411	−0.059	0.235
76977	48.0592317	−55.2158611	18.637	0.391	0.069	0.168
67539	48.0739587	−55.2157406	17.671	0.075	0.023	−0.046
81943	48.0498728	−55.2149442	18.686	0.439	−0.061	−0.009
76627	48.0594802	−55.214196	18.17	0.239	0.013	0.126
72106	48.06711	−55.2135349	17.846	0.107	−0.041	0.055
81984	48.0501694	−55.2131204	18.525	0.172	−0.019	−0.141
68014	48.0733391	−55.2127941	18.323	0.032	−0.007	−0.009
67728	48.0739974	−55.2096186	18.182	0.526	0.13	−0.191
74845	48.0628007	−55.2085887	18.243	0.2	0.011	0.001
73043	48.0655777	−55.2073627	18.409	0.191	−0.061	0.065
8755	48.0655993	−55.2368193	18.176	0.172	0.055	0.094
32865	48.0687891	−55.2225572	18.135	0.282	0.142	−0.043
34733	48.065501	−55.2201113	18.044	0.18	−0.061	−0.02
69581	48.0709143	−55.2121116	18.053	0.366	−0.02	0.107
96886	48.0733873	−55.2002784	17.787	0.19	−0.004	0.05
5315	48.0808075	−55.2349835	19.146	0.347	0.066	0.152
12844	48.0469911	−55.2331005	19.498	0.264	−0.09	0.007
34871	48.0652367	−55.2287238	18.898	0.249	−0.014	0.075
30492	48.0723216	−55.2275608	19.315	0.338	0.157	−0.002
32394	48.0693159	−55.226576	18.926	0.105	0.01	0.139
27018	48.0788222	−55.2257367	19.796	0.346	0.013	−0.088
28759	48.0758134	−55.2254191	18.87	0.232	0.03	0.073
36170	48.0632261	−55.224378	18.957	0.325	0.042	0.282

Bibliography

Baggett, S., Gosmeyer, C., Noeske, K., 2015, WFC3 Instrument Science Report 2015-03: WFC3/UVIS Charge Transfer Efficiency 2009–2015, http://www.stsci.edu/hst/wfc3/documents/ISRs/WFC3-2015-03.pdf

Bellini, A., Anderson, J., van der Marel, R. P., et al. 2014, The Astrophysical Journal, 797, 115

Bruzual, G., & Charlot, S. 2003, Monthly Notices of the Royal Astronomical Society, 344, 1000

Cappellari, M., Bacon, R., Bureau, M., et al. 2006, Monthly Notices of the Royal Astronomical Society, 366, 1126

Davies, M. B. 2015, Ecology of Blue Straggler Stars, 203

de Marchi, F., de Angeli, F., Piotto, G., Carraro, G., & Davies, M. B. 2006, Astronomy & Astrophysics, 459, 489

Dotter, A., Chaboyer, B., Jevremović, D., et al. 2008, The Astrophysical Journal Supplement Series, 178, 89-101

Dotter, A., Sarajedini, A., Anderson, J., et al. 2010, The Astrophysical Journal, 708, 698

Ferraro, F. R., Paltrinieri, B., Fusi Pecci, F., et al. 1997, Astronomy & Astrophysics, 324, 915

Ferraro, F. R., Beccari, G., Dalessandro, E., et al. 2009, Nature, 462, 1028

Ferraro, F. R., Lanzoni, B., Dalessandro, E., et al. 2012, Nature, 492, 393

Ferraro, F. R., Lanzoni, B., Dalessandro, E., Mucciarelli, A., & Lovisi, L. 2015, Ecology of Blue Straggler Stars, 99

Harris, W. E. 2010, arXiv:1012.3224

Hesser, J. E., McClure, R. D., Hawarden, T. G., et al. 1984, Publications of the Astronomical Society of the Pacific, 96, 406

Hills, J. G., & Day, C. A. 1976, The Astrophysical Journal Letters, 17, 87

Leigh, N., Sills, A., & Knigge, C. 2007, The Astrophysical Journal, 661, 210

Leigh, N., Sills, A., & Knigge, C. 2011a, Monthly Notices of the Royal Astronomical Society, 415, 3771

Leigh, N., Sills, A., & Knigge, C. 2011b, Monthly Notices of the Royal Astronomical Society, 416, 1410

Leigh, N., Knigge, C., Sills, A., et al. 2013, Monthly Notices of the Royal Astronomical Society, 428, 897

Knigge, C., Leigh, N., & Sills, A. 2009, Nature, 457, 288

McGahee, C. E. 2014, Ph.D. Thesis, Clemson University

Kozhurina-Platais V. & Anderson, J. 2015, WFC3 Instrument Science Report 2015-02: Standard Astrometric Catalog and Stability of WFC3/UVIS Geometric Distortion, http://www.stsci.edu/hst/wfc3/documents/ISRs/WFC3-2015-02.pdf

McClure, R. D., Hesser, J. E., Stetson, P. B., & Stryker, L. L. 1985, Publications of the Astronomical Society of the Pacific, 97, 665

McCrea, W. H. 1964, Monthly Notices of the Royal Astronomical Society, 128, 147

Mucciarelli, A., Lovisi, L., Ferraro, F. R., et al. 2014, The Astrophysical Journal, 797, 43

Piotto, G., De Angeli, F., King, I. R., et al. 2004, The Astrophysical Journal Letters, 604, L109

Puzia, T. H., Saglia, R. P., Kissler-Patig, M., et al. 2002, Astronomy & Astrophysics, 395, 45

Sarajedini, A., Bedin, L. R., Chaboyer, B., et al. 2007, The Astronomical Journal, 133, 1658

Salinas, R., Contreras Ramos, R., Strader, J., et al. 2016, arXiv:1605.06517

Watkins, L. L., van der Marel, R. P., Bellini, A., & Anderson, J. 2015a, The Astrophysical Journal, 803, 29

Watkins, L. L., van der Marel, R. P., Bellini, A., & Anderson, J. 2015b, The Astrophysical Journal, 812, 149

Chapter 3

Dependence of Global BSS Properties on Cluster Environment

3.1 The Velocity Dispersion Profiles of BSSs

The proper motion information derived from the analysis presented in Chapter 2 can be used to measure the velocity dispersion of BSSs with respect to the one of its parent stellar population. The underlying assumption is that two-body relaxation effects should efficiently remove kinetic energy from BSSs during their lifetime. Studies show that BSSs have typical masses of 1.0−1.2 $M_\odot$ (Fiorentino et al., 2014; Stępień & Kiraga, 2015), whereas a star of the MSTO has a mass usually around ∼0.8 $M_\odot$ in a typical GC. Therefore equipartition dictates that BSS velocities will decrease, compared to the rest of the cluster population, as the GC approaches full relaxation. This suggests that the relative difference in velocity dispersion between the BSS population and, for example, the MS population, must depend somewhat on the degree of relaxation of the parent cluster.

We use the BSS samples and proper motions from Chapter 2 and construct velocity dispersion profiles in the following way:

1. For all GCs, we only use stars that have an estimated position error smaller than $\sigma_{\mathrm{R},\star}$, which are the expected central velocity dispersion, in ACS pixel units, as calculated in Section 2.4.2 (see also Figure 2.8).
2. We divide the cluster spatial sampling in 4 radial bins for the case of BSSs, and 7 radial bins for the case of MS stars.

3. We calculate the proper motion velocity dispersion (σ_R) in each radial bin and assign an error defined by $\sigma_R/\sqrt{N}$, where N is the number of stars in the corresponding radial bin.

After removing the GCs that had MS stars with position errors too large to accurately build a dispersion profile, we end up with 28 GCs where we can construct velocity dispersion profiles for both MS and BSSs. We show the velocity dispersion profiles for the selected GC sample in Figure 3.1. The velocity dispersion in each bin is shown in red and grey points, for BSSs and MS stars respectively. The core radius and half-light radius are shown in vertical dashed lines. A fast inspection to the velocity dispersion profiles suggests that, despite of the observable scatter, we still find that as expected for a more massive population, the BSSs have lower σ values than MS stars. This is only the second study in which velocity dispersions of BSSs have been presented for such a large number of GCs, while also showing them to be dynamically cooler systems, with respect to MS stars. Recently, Baldwin et al. (2016) used HST proper motion measurements from the HSTPROMO project and constructed velocity dispersion profiles for BSSs in 19 GCs. We find good agreement between the measured dispersion profiles of the few GCs in common, and further strengthen their result that BSSs have typically lower velocity dispersions than MSTO stars.

The expected behaviour of the σ_{BSS}/σ_{MS} ratio is that it should become increasingly smaller as the GC approaches full equipartition. Therefore, in order to gain perspective on the global BSS velocity dispersions, we plot the σ_{BSS}/σ_{MS} ratio as a function of the cluster concentration from the Harris (2010) catalog and core dynamical age, for different maximum radial distances. The core dynamical age is calculated as the chronological age from Dotter et al. (2010) divided by the core relaxation time from Harris (2010). The corresponding plots are shown in Figure 3.2. The sub-panels in both Figures show the values for BSS and MS samples with increasing maximum cluster-centric distance. The first sub-panel shows values from stars within $0.8r_c$, while the subsequent (inferior) sub-panels show a larger portion of the cluster, as well as the values from the consecutive previous inner sample (grey points). This way one can see exactly how the σ_{BSS}/σ_{MS} ratios change between consecutive sub-samples at different cluster-centric distances. The σ_{BSS}/σ_{MS} ratio seems to generally scatter around the value ~0.8.

We can also observe from these plots that the average σ_{BSS}/σ_{MS} ratio increases when expanding the maximum cluster-centric distance of the sample, i.e. the previous inner sub-sample (grey points) always appear to have smaller σ_{BSS}/σ_{MS} ratios. Also, this effect seems to be stronger for the more concentrated GCs, i.e. the GCs with large concentration parameter. This result confirms what we had expected based on equipartition principles. However, there still exists the possibility that, apart from the

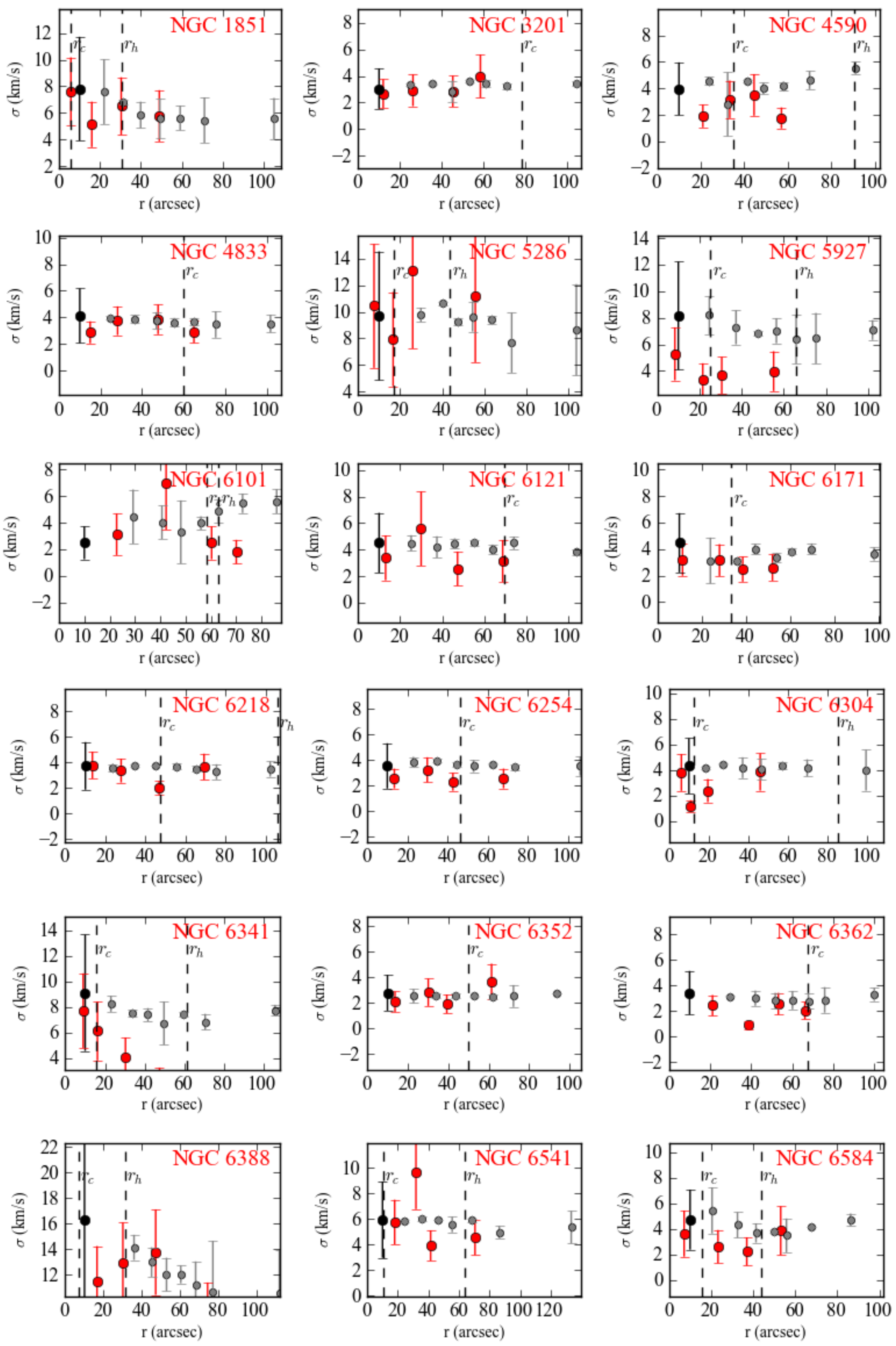

Figure 3.1: Proper motion velocity dispersion profiles using the proper motion catalogs from Chapter 2. The velocity dispersion in each bin is shown in red and grey points, for BSSs and MS stars respectively. The σ value at 10 arcsec are calculated using all GC stars down to 1 mag below the turnoff, but excluding stars with position errors larger than the expected velocity dispersion. The core radius and half-light radius are shown in vertical dashed lines for each GC.

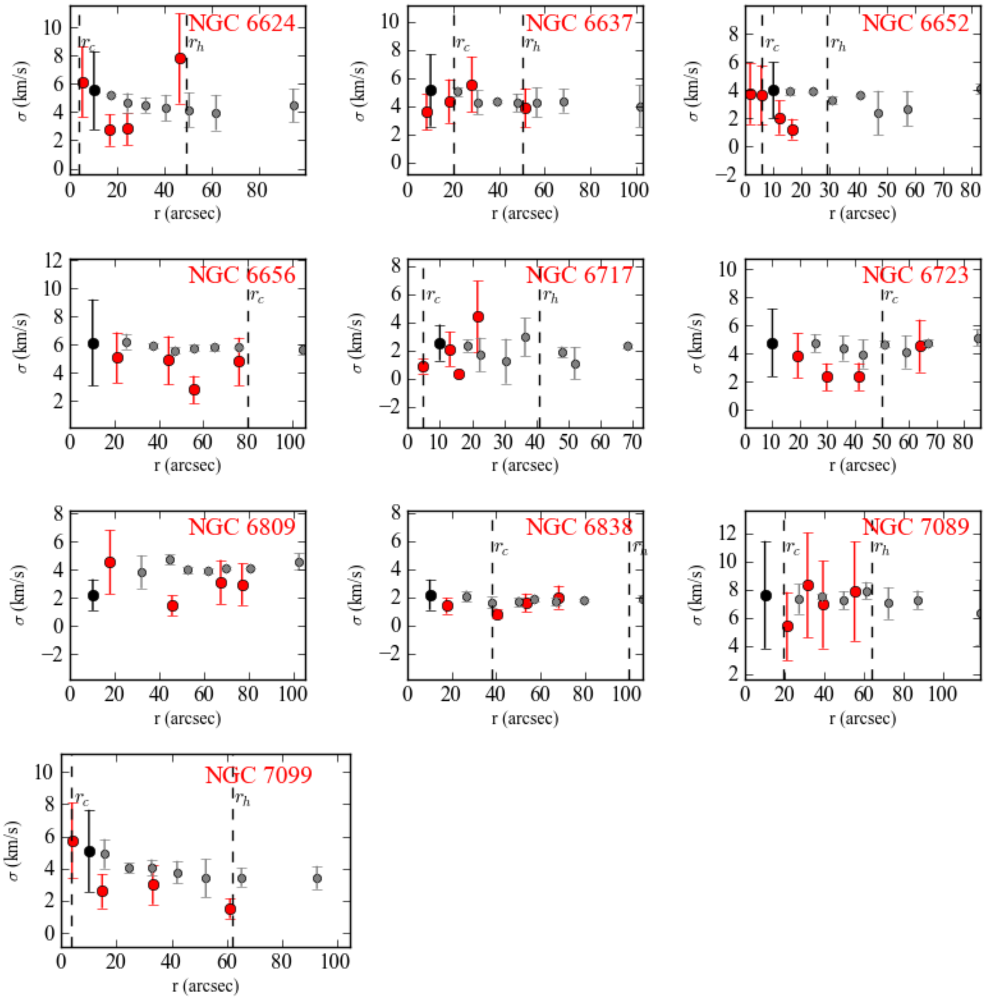

Figure 3.1: continued

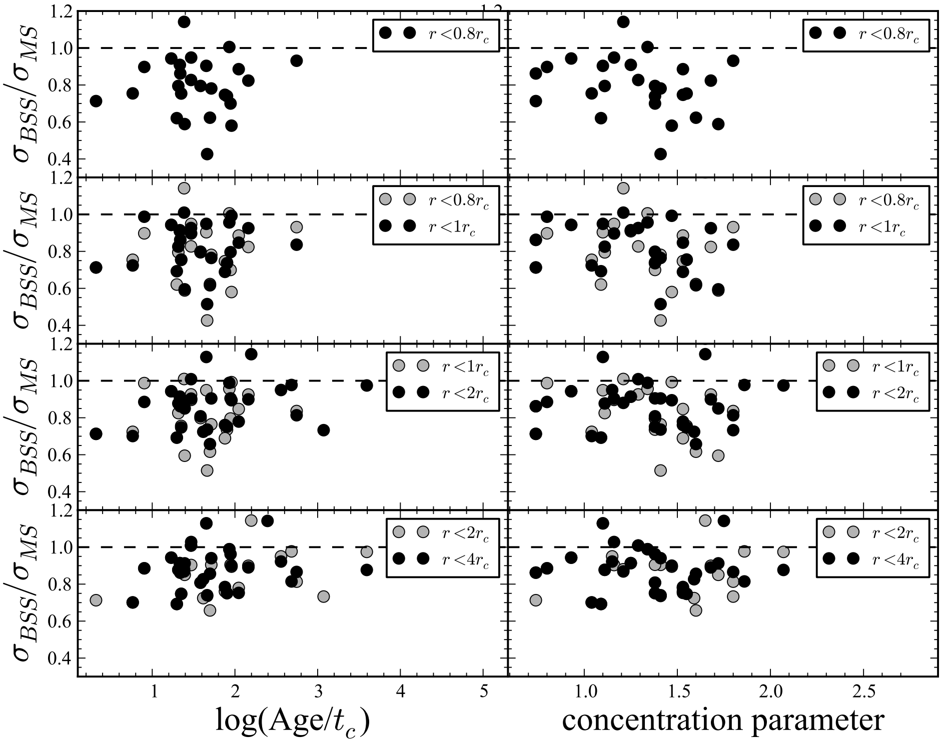

Figure 3.2: *Left*: The σ_{BSS}/σ_{MS} ratio as a function of $\log(age/t_c)$, where *age* is the GC chronological age and t_c is the core relaxation time. The sub-panels show the values for BSS and MS samples with increasing maximum cluster-centric distance. The first sub-panel shows values from stars within $0.8r_c$, while the subsequent sub-panels show a larger portion of the cluster, as well as the values from the consecutive previous inner sample (grey points). This way one can see exactly how the σ_{BSS}/σ_{MS} ratios change between consecutive sub-samples at different cluster-centric distances. We only plot the σ rations for the radial sub-samples that contain more than 15 BSSs. *Right*: Same as in the Left Figure, but the σ ratios are plotted as a function of cluster concentration parameter.

dynamical cooling of BSSs because of two-body relaxation, the BSS populations themselves are physically different (e.g. different average mass) between the inner regions of dynamically older GCs versus the dynamically younger GCs, which could also be linked to their dominant formation mechanisms.

3.2 Photometric Mass Estimates for BSSs

Motivated by the results from Section 3.1 we investigate further on the individual physical properties of our BSS samples. In particular, the available high-resolution and high-signal-to-noise photometry from the BSS catalogs allows us to estimate stellar masses and ages for BSSs, based on their measured optical colours and magnitudes with respect to a set of appropriate isochrones. This approach has been used already by previous studies (Lanzoni et al., 2007; Lovisi et al., 2012) in an attempt to characterize the BSS physical properties in individual GCs, but has never been performed in a systematic and homogeneous way for a large sample of GCs. The proper motion cleaned HST catalogs of BSSs from our work, gives us the unique opportunity to take this technique to its furthest capabilities.

3.2.1 Isochrone Interpolation Method

We use the set of Dartmouth isochrones (Dotter et al., 2008) and adopt the corresponding cluster parameters of reddening E(F606W-F814W), metallicity and distance modulus from the values reported in Dotter et al. (2010). For the GCs not present in such study, we adopt the parameters from Harris (2010). We convert the galactic extinction factors given in Harris (2010) to the ACS/WFC filter system by using the transformations from Sirianni et al. (2005). For all GCs, we adopt a representative value of 0.2 for the alpha-enhancement.

The BSS selection method for our catalogs described in Section 2.4.3 used the 1 Gyr old isochrone as the blue limit for the BSS region, therefore we use a set of isochrones with a range in ages from 1 to 9 Gyr as the stellar library grid that fully encompasses the BSS region in the CMD. The detailed steps during the interpolation can be described as follows:

1. We shift all isochrones to the corresponding apparent luminosity and reddening, and plot them in the F814W vs F606W−F814W mag space.
2. For each BSS, we find the two nearest isochrones in (mag,mag) space, i.e. one bluer and one redder than the BSS position. We can refer to them as isochrones A and B.
3. The isochrones are discrete set of points in the CMD (each representing a specific stellar mass), an hence for both isochrones, we find the two points from each isochrone that are closer to the BSS position in the CMD. By construction, this means a brighter and a fainter isochrone point with respect to the BSS position. We can refer to them as A1,A2 and B1,B2.
4. We interpolate between A1 and A2 and find $A_\star$, the point that has the same F814W magnitude as the BSS. We do the same for B1 and B2 and find $B_\star$.
5. We calculate the interpolated mass values of $A_\star$ and $B_\star$, and interpolate now in F606W−F814W space and obtain an interpolated mass and age for the corresponding location of the BSS.

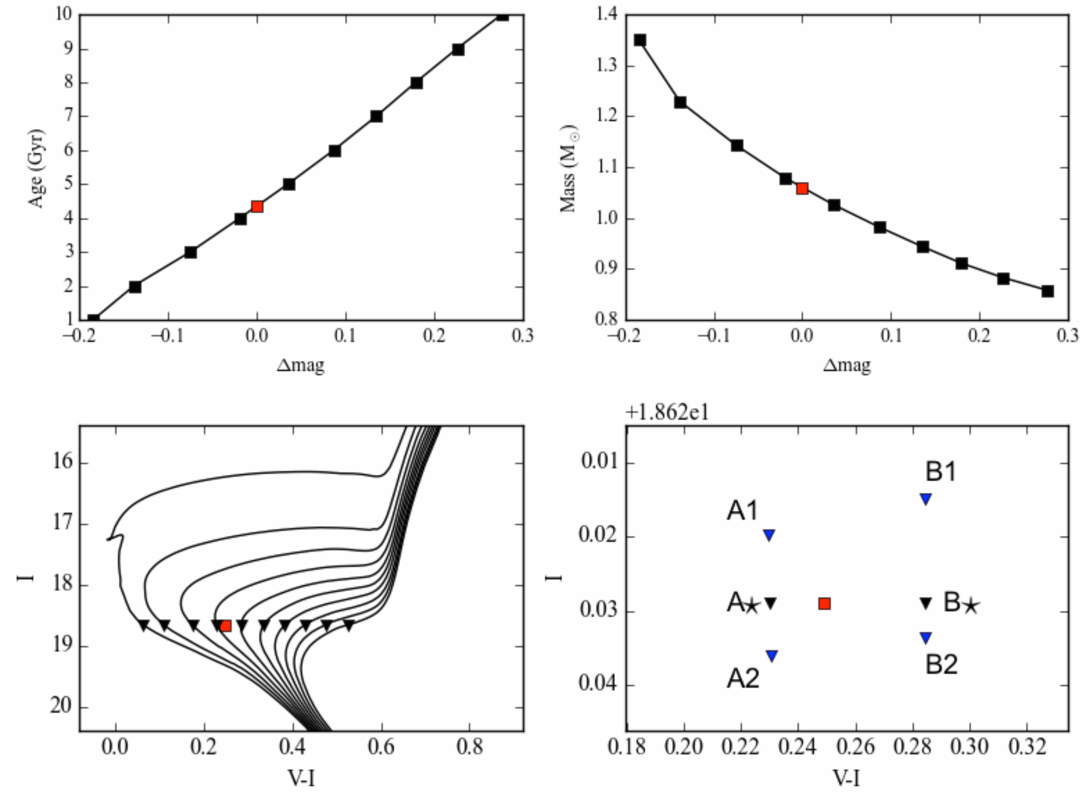

Figure 3.3: Example of the steps described in Section 3.2.1 for a BSS in NGC 1261. The lower-left panel shows the position of the BSS in the CMD (red square), along with all isochrones and all the nearest points to each isochrone (black triangles). The points from the two closest isochrones (i.e. A1,A2 and B1,B2) are zoomed in the CMD in the lower-right panel. The interpolated $A_\star$ and $B_\star$ points are labeled accordingly. The two top panels show the mass and age interpolation for this particular BSS.

6. We adopt these interpolated mass and age values as the estimates for each BSS. We refer to them as the photometric BSS mass and age.[1]

We show in Figure 3.3 an example of the steps described above for a BSS in NGC 1261. The lower-left panel shows the position of the BSS in the CMD, along with all isochrones and all the nearest points to each isochrone (black triangles). The points from the two closest isochrones (i.e. A1,A2 and B1,B2) are shown in the lower-right panel. The interpolated $A_\star$ and $B_\star$ points are labeled accordingly. The two top panels show the mass and age interpolation for this particular BSS. We also show in Figure 3.4 the entire BSS population of NGC 1261 plotted in the CMD along with the corresponding set of isochrones. The lower-left panel shows the BSS mass as a function of the BSS age. The top panels show the histograms of BSS mass and age for the NGC 1261 sample.

---

[1] In the rest of this work, we use the terms BSS mass and BSS photometric mass interchangeably. Please note that they refer to the interpolated values, unless stated otherwise.

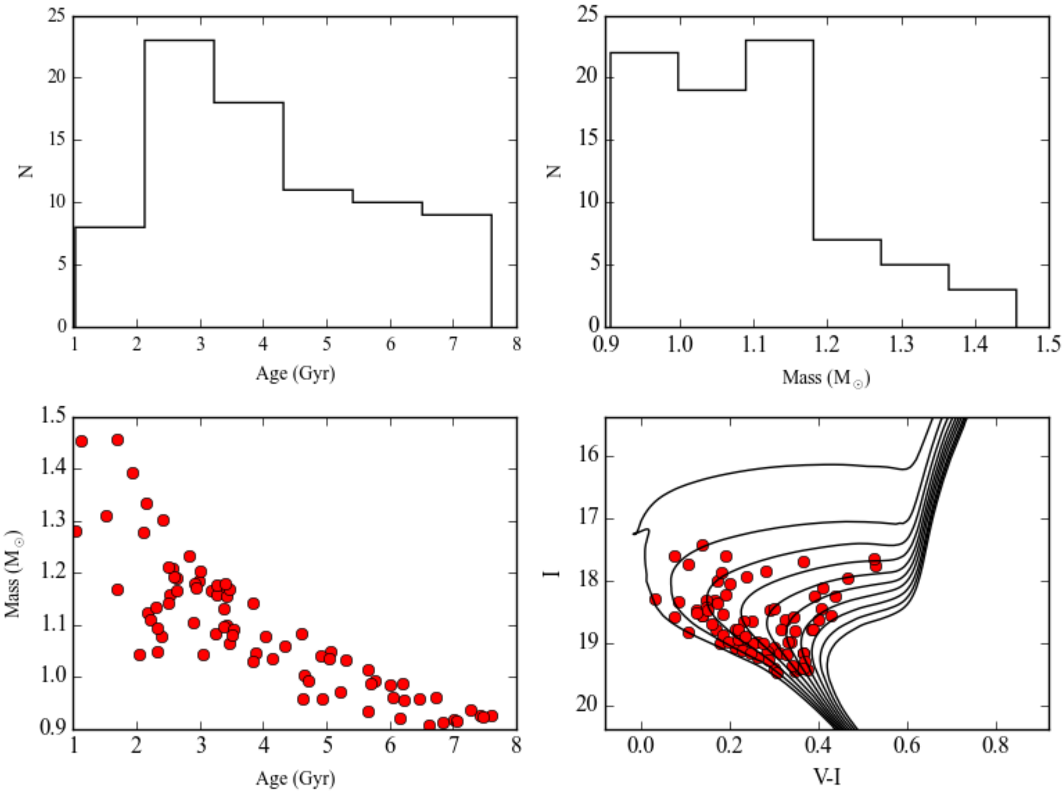

Figure 3.4: The lower-right panel corresponds to the entire BSS population of NGC 1261 plotted in the CMD along with the corresponding set of isochrones. The lower-left panel shows the BSS mass as a function of the BSS age. The top panels show the histograms of BSS mass and age for the NGC 1261 sample.

3.2.2 BSS Photometric Mass Distribution

We apply this interpolation method to the entire library of catalogs from Chapter 2 and obtain photometric masses for all BSSs. In the literature, masses of binary BSSs have been derived from the solution of the eclipsing light curves and radial velocity curves (Geller & Mathieu, 2011). Not a lot has been done for masses of single BSSs. In a recent work, Fiorentino et al. (2014) used the pulsation properties of BSSs that belong to the variable type SX Phe in NGC 6541 and derived pulsation model masses for nine BSSs. They found the pulsation model masses to be in good agreement with the photometric masses derived from stellar tracks. In another work, Stępień & Kiraga (2015) studied the evolution of 975 models of close binaries with different initial parameters. Their models included mass exchange between components and realistic mass and angular momentum loss due to stellar winds. Their models created a large number of BSSs during binary mergers and mass-transfer interaction. In particular, their merger-products are found to be mostly single BSSs and they provide the stellar mass for 67 of them. We plot in Figure 3.5 the single BSS masses from Fiorentino et al. (2014) and Stępień &

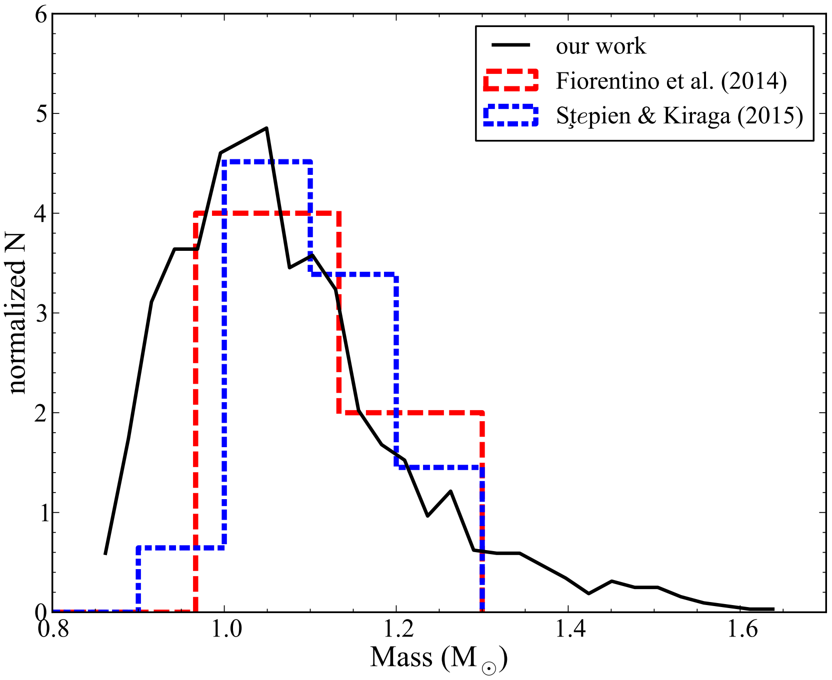

Figure 3.5: Histogram of BSS mass estimates from studies in the literature. The distribution of the photometric BSS mass estimates is shown in the solid black line, which includes all BSSs from the entire GC sample.

Kiraga (2015) and the photometric mass distribution of our entire BSS library. The Figure shows a reasonable agreement between all studies for the peak BSS mass. Both Fiorentino et al. (2014) and Stępień & Kiraga (2015) find the peak BSS mass to be $\sim$1$-$1.1 M$_\odot$, while our distribution peaks at $\sim$1 M$_\odot$. We must note, however, that the steep drop in the mass distributions of Fiorentino et al. (2014) and Stępień & Kiraga (2015) for BSS masses below $\sim$1 M$_\odot$ might suggest a selection bias, instead of a real physical absence of such stars. This can be understood if we consider the fact that most BSS selection methods in the literature avoid CMD regions too close to the MSTO, since contamination can be very severe at such low luminosities. We therefore believe that our selection technique, on the contrary to most previous studies, is able to robustly sample BSSs at these lower luminosities, because of the accurate decontamination of our BSS samples. Another interesting result is that the BSS mass function slope between $\sim$1$-$1.3 M$_\odot$ seems very consistent in all studies. The shape of the BSS mass function can likely be used to put constraints on the BSS formation models, as it should strongly depend on the binary mass-ratio and period distributions (Hypki & Giersz, 2016a,b), as well as on the likelihood of particular stellar masses in 2 or 3-body interactions. The detailed analysis of the BSS mass function is beyond the scope of this work, and hence we limit ourselves to a more qualitative analysis.

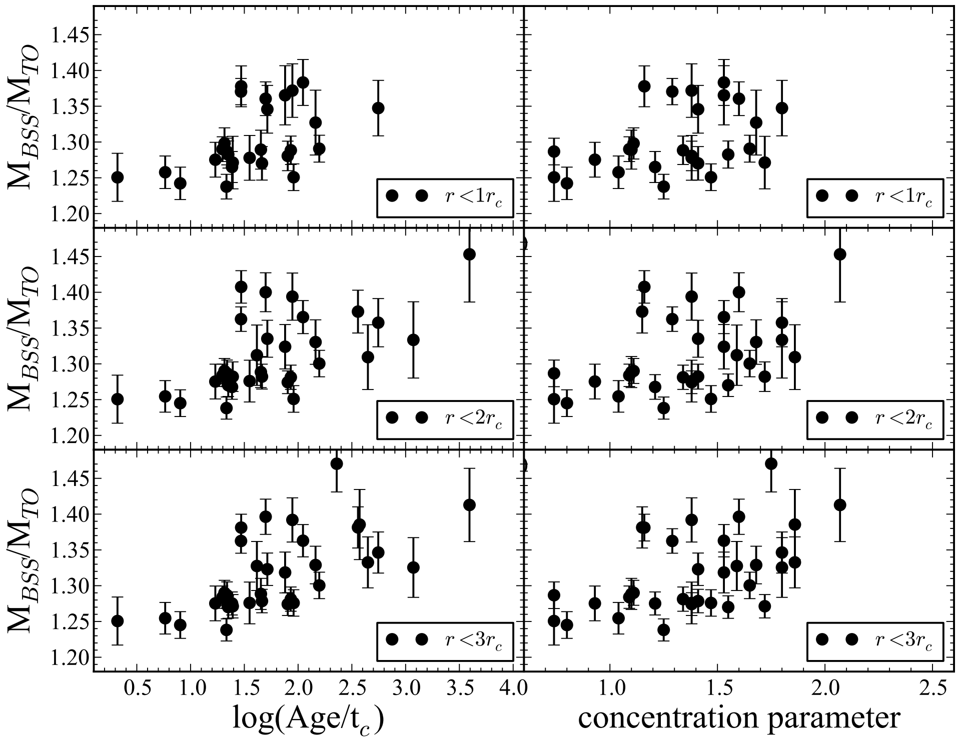

Figure 3.6: The average BSS mass, normalized to the MSTO mass, as a function of core dynamical age (left panel) and cluster concentration (right panel), for BSS samples at different cluster-centric distances. We only plot BSS samples larger than 10 stars in the corresponding radial limit.

3.3 BSS Mass Dependence on the Cluster Environment

We wish to better understand the results from Section 3.1 and look for a potential correspondence of the BSS velocity dispersions with BSS stellar mass. The σ_{BSS}/σ_{MS} ratios showed to undergo an "evolution" towards higher values (i.e. dynamically warmer BSS populations) in a given GC when looking at star samples at larger cluster-centric distances. Therefore, there seems to be an underlying principle affecting the dynamics of BSSs and their positions within the cluster. Indeed, a recent work by Ferraro et al. (2012) suggests that two-body relaxation is the most important aspect of this problem, and that the dynamical age of the cluster should unequivocally determine the radial segregation of BSSs. Such proposal also predicts that more massive BSSs will sink into the cluster's core more rapidly than less massive BSSs, as their relaxation timescales should be shorter. The core would then be progressively populated by more massive BSSs, hence inducing a mass segregation within the BSS population, as the GC gets dynamically older.

We plot the average BSS mass, normalized to the MSTO mass[2], as a function of core dynamical age (left panel) and concentration (right panel) in Figure 3.6, for BSS samples at different cluster-centric distances. We only plot GCs with BSS samples larger than 10 stars in the corresponding radial limit. The Figure shows a very strong correlation between the average BSS mass and the core dynamical age. Correspondingly, the concentration parameter also correlates with average BSS mass, but shows a larger scatter. Additionally, the trend of increasing average BSS mass seems to hold true for all BSS samples at different maximum cluster-centric distances. This is a striking result, particularly because we did not expect such a strong dependence of the BSS mass with the dynamical age of the cluster. We don't see any hints of the average BSS mass changing with increasing cluster-centric distances, therefore making unclear if BSSs are mass segregated at these innermost regions. The observed increase in average BSS mass with the cluster dynamical age can still be explained by mass segregation if we consider what is the expected radius of avoidance (r_{avoid}) for the GCs in our sample. The radius of avoidance is a quantitative physical scale that corresponds to the radius below which a star more massive than a certain mass, is expected to have had enough time to be affected by two-body relaxation and sink to the GC center (Hypki & Giersz, 2016b). The value of r_{avoid} for BSSs increases with the dynamical age of the cluster, and can be lower than $r_{avoid} \lesssim 10r_c$ for only the more dynamically younger GCs (i.e. $\log(age/t_c)\lesssim 2$, see Ferraro et al. (2012)). Unfortunately, these are the GCs with the most extended cores and therefore, because of our limited field of views, we can't probe the regions immediately outside the core where we would expect the absence of higher mass BSSs. On the other hand, the GCs with $\log(age/t_c)\gtrsim 2$ should have $r_{avoid} \gtrsim 10r_c$ (Ferraro et al., 2012), which is a cluster-centric distance too large for our data to be able to detect a significant evolution of the average BSS mass. We note however that for such higher r_{avoid} values in dynamically older GCs, our BSS catalogs would be well within the segregated region and hence an increase in the average BSS mass with dynamical age would also be expected. Lastly, we note that Figure 3.6 shows an abrupt increase in BSS mass for our GCs with concentration $c \gtrsim 1$. Therefore this can naturally explain the lower σ_{BSS}/σ_{MS} ratios in the inner-most ($r < 0.8r_c$) samples of GCs with $c \gtrsim 1$ (see Figure 3.2), based on the BSS relaxation principles discussed above.

3.4 Probability Density Functions of the CMD of BSSs

In the previous sections we have studied the BSS velocity dispersions and the BSS masses in the context of the dynamical state of the parent GC. At this stage of our study, our results support a scenario in which dynamical friction effectively sinks heavy

---

[2] The MSTO mass is calculated from isochrone interpolation similarly as the BSS mass

BSSs towards the inner cluster regions. Additionally, we showed in Section 3.1 that in the vast majority of the GC sample, the BSS populations have smaller velocity dispersion than MS stars, hence implying that these BSS systems have probably become relaxed at the cluster-centric regions sampled by our data.

Thus far, there is still no clear indication for particular formation mechanisms, since the rather relaxed dynamical state of our BSS samples effectively *erase* the initial information of the orbits from the BSS progenitors. However, the strong correlation between the average BSS mass and the core dynamical age motivates a study of the CMD properties of BSS for GCs of different dynamical state. Ideally, we want to quantify the effective density of BSSs within CMD and try to recover and identify the mass function evolution that is driving the results from Section 3.3.

3.4.1 Dependence of the BSS CMD on Metallicity

In order to gain statistical information from the density of BSS within the CMD, we need first to identify any general dependence of the GC CMD with global parameters. Such a case is true for the cluster metallicity. Basically, the iron content in the atmosphere of stars changes their opacity, which allows them to reach hydrostatic equilibrium with a cooler nucleus, thereby extending their main-sequence lifetime and also making the star cooler than a metal-poor star of the same mass. This translates as metal-rich GCs appearing redder in the CMD than a metal-poor GC. Similarly, this will also affect the relative position of BSSs with respect to the MSTO. In Figure 3.7 we show 2-dimensional Probability Density Functions (PDFs) of stacked BSS population CMDs, for different metallicity bins. Each bin includes 7-8 GCs that fall inside the metallicity bin (see Table 2.1 and Figure 2.1). The mean metallicity of each GC group is shown in each panel of the Figure. The metallicity increases from top-left to bottom-right. The 2-dimensional PDF shows a consistent structure for all metallicities. In particular, the BSS PDF is characterized by a low luminosity peak and an elongated elliptical surface that contains much of the BSS population. Also, the BSS PDF is very extended because of yellow stragglers and bright hot BSSs. The major axis of the elliptical surface rotates clock-wise with increasing metallicity, as expected from the similar change in stellar evolutionary tracks at higher metallicities.

3.4.2 Evolution of the BSS CMD with Dynamical Age

We decide to separate the entire 38 GC sample into 3 definitive metallicity groups. We name these groups as the Metal-Poor (MP) which has [Fe/H]<-1.7, the Metal-Intermediate (MI) which has -1.7<[Fe/H]<-1.0, and the Metal-Rich (MR) which has

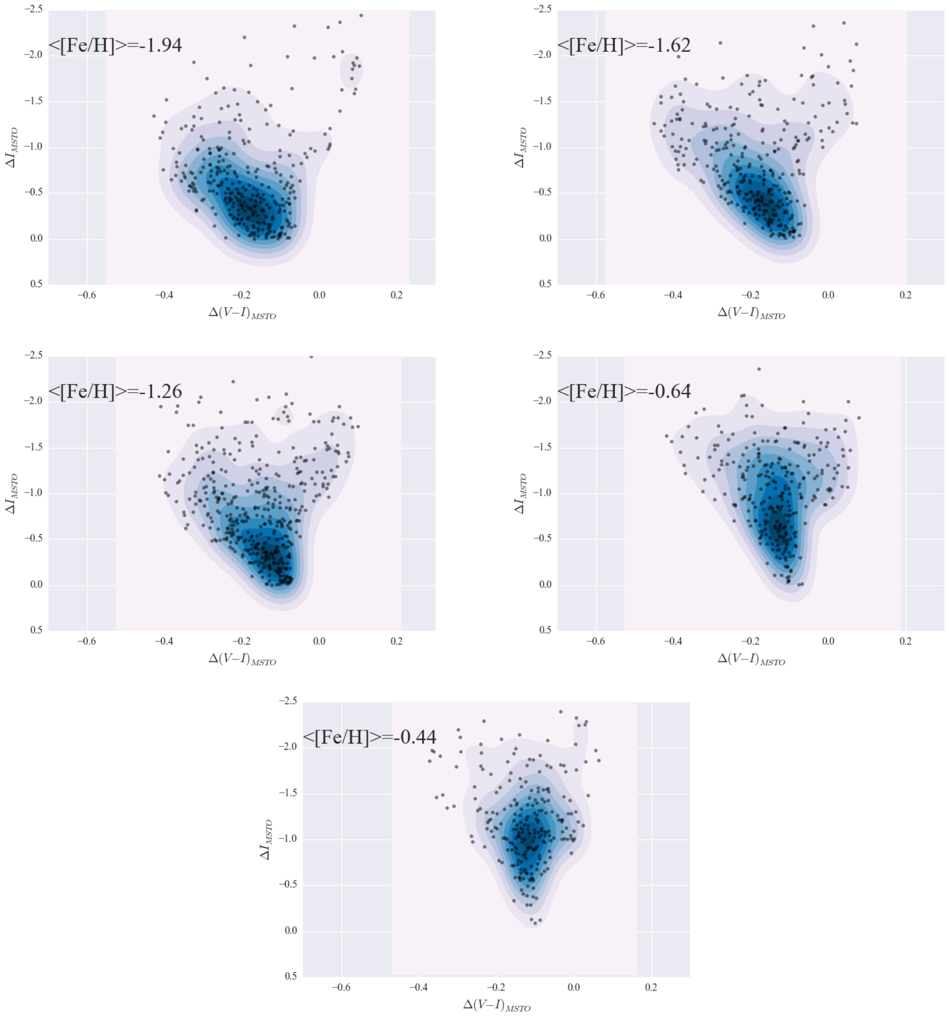

Figure 3.7: 2-Dimensional probability density functions of stacked BSS population CMDs. Each panel corresponds to a group of GCs of similar metallicity (see Table 2.1 and Figure 2.1). The mean metallicity of the GC group is shown in each panel. The mean metallicity increases from top-left to bottom-right.

[Fe/H]>-1.0. This way we can construct stacked BSS population CMDs for each group and study the "evolution" of the BSS PDF versus cluster properties. The assumption is that because we are using similar-metallicity GCs in each group, we won't introduce fluctuations in the BSS PDF induced by its dependence on metallicity, as observed in Figure 3.7. We proceed now to sort all GCs by their core dynamical age ($\log \mathrm{Age}/\mathrm{t}_c$) in each, the MP, MI, and MR groups. Then we separate them in three sub-groups of equal size (when possible) and define a Dynamically Old (DO), Intermediate (DI), and Young (DY) sub-group. This means we have separated the entire GC sample in 3 groups, each having 3 sub-groups. The total sample contains 38 GCs, therefore each sub-group has $38/(3\times3)\approx4$ GCs. The BSS PDFs for DO, DI and DY clusters are shown in Figure 3.8, Figure 3.9 and Figure 3.11 for the MP, MI and MR groups, respectively.

3.4.2.1 Analysis of MP GCs

The BSS PDFs for the MP group are shown in Figure 3.8. The three columns show the BSS PDFs of DY, DI and DO clusters, respectively. The fourth column shows the normalized histograms of the BSS mass for each of the three BSS sub-groups. Each of the colours used in the histogram correspond to the sub-group of the corresponding colour in the three left columns, i.e. black for the DY clusters, red for the DI clusters and green for the DO clusters. The five descending rows show the corresponding BSS PDFs for increasing cluster-centric distances, which is very important because there exist the risk that the stacked BSS samples at the inner-most regions (i.e. where we suffer from low number statistics) could be dominated and hence biased by one or two GCs in the sub-group. By considering distances out to $5r_c$ we should be able to end up with stacked samples representative of the entire population. We also note that, as we will show below, we find that the BSS PDFs don't change dramatically when considering larger cluster-centric distances, ergo excluding a strong bias due to a single or two individual clusters.

We observe a clear "evolution" of the BSS PDF between the three dynamical states. In particular, if we limit the analysis only to the first row (the $r < 1r_c$ sample), the BSS PDF of the DY clusters is narrower than in the other two cases, showing also a distinct peak in BSS concentration at the bluer $(V-I)$ colours. The BSS PDF of the DI clusters shows a lot more BSS contribution in the brighter range while also still conserving the elongated concentration of BSSs peaked at low luminosities. The BSS PDF of the DO clusters suffers from low number statistics but still is sufficient to observe the absence of the higher BSS concentration at bluer colours. Contrary to the DY case, the BSS PDF seems more flat. More notorious is the significant absence of BSSs at $\Delta(V-I) \approx -0.2$ mag and $\Delta I \approx 0$--0.5 mag, which are instead highly present in the DY and DI cases. These differences in the BSS PDFs are also notorious in the BSS mass histograms, which show that the BSS masses of the DO clusters have more relative contribution of high mass BSSs and a significant lower contribution of low mass BSSs. On the other hand, the BSS mass distribution in DY clusters is peaked at the lowest BSS masses and decreases steeply after $\sim$1 $M_\odot$. The BSS mass distribution of the DI clusters show an apparent intermediate case between the other two. Interestingly, the stacked GC CMDs suggest that the sharp cut at low masses for the DY and DI histograms could be a selection effect, since we observe a cloud of stars that nicely follow the BSS sequence and merges with the MS of the GCs[3]. These plots then suggest that such BSS sequence is less significant in the DO clusters.

---

[3] These stars were not considered as BSS candidates given our selection method described in Section 2.4.3, which excluded stars below the MSTO magnitude.

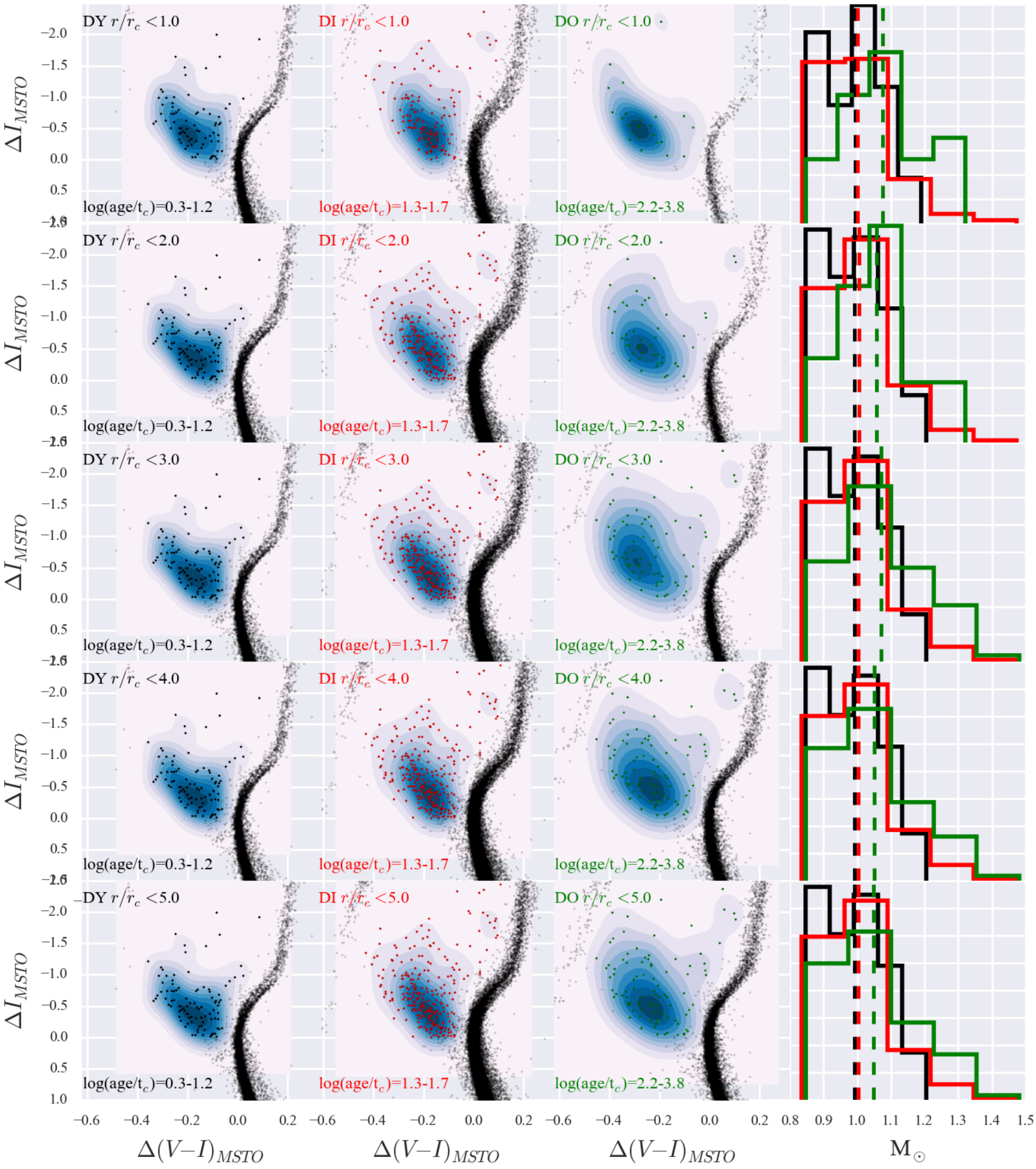

Figure 3.8: The BSS PDFs of the metal-poor group clusters. The columns show the BSS PDFs of DY, DI and DO clusters, respectively. The last column shows the normalized BSS mass histograms for each sub-group. The average mass value is shown as a vertical dashed line. The colours represent the same sub-groups in all columns, i.e. black for the DY clusters, red for the DI clusters and green for the DO clusters. The five descending rows show the corresponding BSS PDFs for increasing cluster-centric distances, as shown in the top-left of each panel. The range in log(age/t$_c$) of each sub-group is shown in the bottom-left of each panel. The full GC populations inside each radial limit are also stacked in order to better illustrate the relative position of BSSs in the CMD. Note that each panel contains between 3-5 stacked GCs which nicely overlap.

The BSS PDFs at larger cluster-centric distances remain very self-consistent within each sub-group. Even when considering BSSs out to $5r_c$, the BSS PDF of the DO clusters is notoriously different than the one of DY clusters. In a more general view, dynamically older GCs are more abundant in yellow stragglers and show a much more extended and more flat PDF, while DY clusters are characterized by a strong BSS sequence that seems to follow the cluster's MS and a higher concentration of BSSs at lower luminosities. For the DO clusters, this translates into a relative under-abundance of low mass BSSs and a larger contribution of high mass BSSs, as it is seen in the BSS mass histograms at all cluster-centric distances.

We consider the possibility that our observations above are biased because of the different number of BSSs inside each panel. For this reason, we redo the analysis by calculating the number of BSSs in the least populated BSS PDF (which is usually on DO clusters) and resample the other two sub-groups by choosing random BSSs until we match that maximum number. We do this for all cluster-centric distances. This test shows that the newly derived BSS PDFs don't change their shapes significantly, and therefore the qualitative differences observed between them are unlikely to be the result of the individual samplings.

3.4.2.2 Analysis of MI GCs

The BSS PDFs for the MI group are shown in Figure 3.9. We observe interesting differences between the sub-groups. The BSS PDF of the DY clusters at $r < 1r_c$ is much wider than the one from the MP group in Figure 3.8, but we note that the MP-DY clusters included a range in $\log(\mathrm{age}/\mathrm{t}_c) = 0.3{-}1.2$, while the MI-DY clusters have $\log(\mathrm{age}/\mathrm{t}_c) = 1.3{-}1.5$, which results in slightly different dynamical states and hence makes it difficult to directly compare both BSS PDFs. The BSS PDF at $r < 1r_c$ for the MI-DI clusters is very similar to the one of DY clusters. For both cases, we observe a strong concentration of BSSs and a corresponding PDF peak at $\Delta(V - I) \approx -0.1$ mag and $-0.5 < \Delta I < 0$ mag. On the other hand, the BSS PDF at $r < 1r_c$ for the DO clusters shows no such feature. Like in the case of the MP-DO clusters, the MI-DO clusters also have a more flat PDF and a relative higher abundance of bright BSSs. The BSS mass histograms are however not able to reproduce this observed difference between the BSS PDFs. They show a similar BSS mass distribution for all three sub-groups. We observe that the described differences between the DY, DI and DO sub-groups are also consistent at all cluster-centric distances. Similarly to the previous case of MP clusters, the general view is that the BSS PDF ”evolves” from a dominant diagonal structure with a peak at low luminosities, into a lesser defined structure that seems more flat and lacks the relative abundance of low luminosity BSSs.

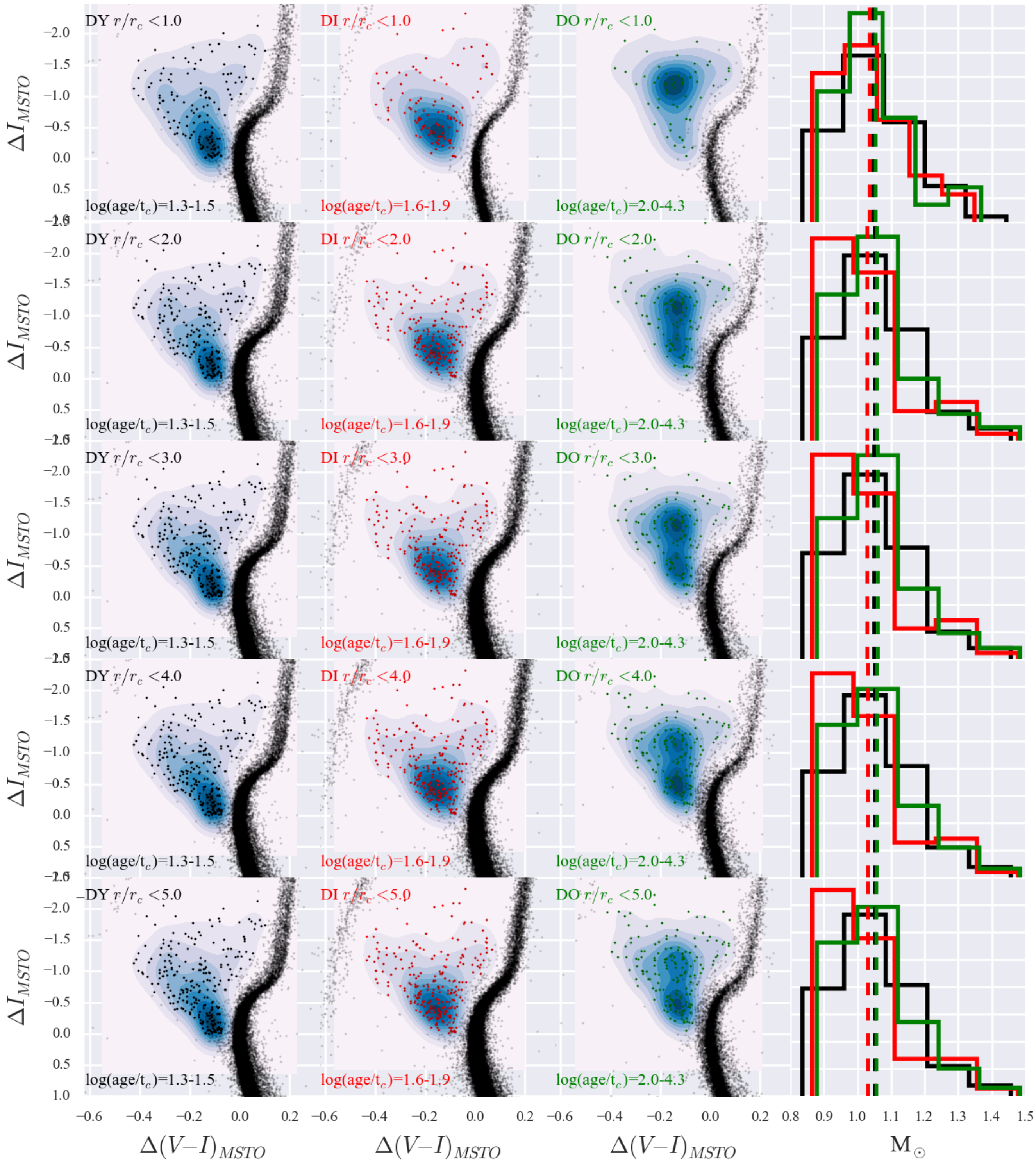

Figure 3.9: Same as Figure 3.8, but for the metal-intermediate GCs.

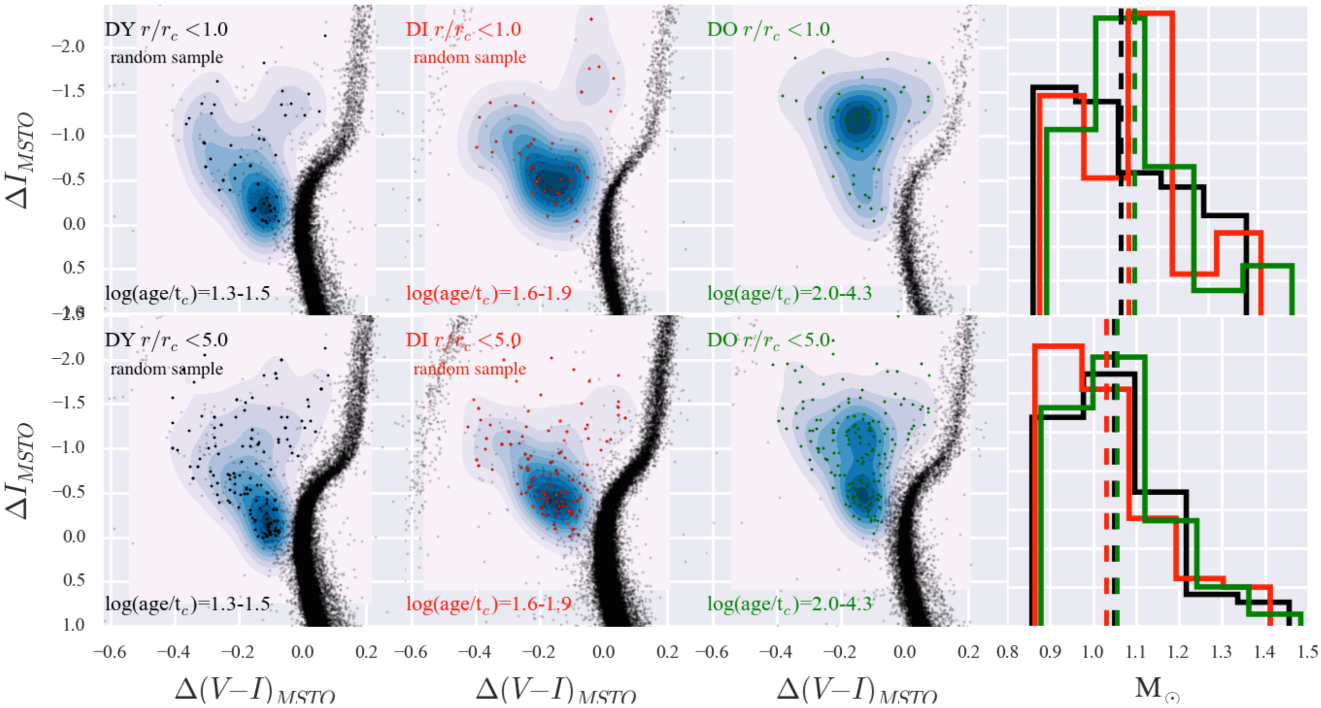

Figure 3.10: Same as Figure 3.9, but using a random resampling of the BSS populations in the DY and DI sub-groups, limited to the size of the DO BSS sample.

Based on the description above we should expect some differences on the BSS mass distributions, and the fact that they seem similar is puzzling. In order to understand this complexity, we recalculate the BSS PDFs for the inner-most and outer-most samples (i.e. $r < 1r_c$ and $r < 5r_c$) using a random resampling of the BSS populations in the DY and DI sub-groups, limited to the size of the DO BSS sample. The result is shown in Figure 3.10. Using this random resampling, we find that the peaks of the mass distribution do change for the $r < 1r_c$ BSS samples. In effect, the peak for DY clusters is at ∼0.9 M$_\odot$, while the peak for DI and DO clusters is at ∼1.0−1.1 M$_\odot$. However, the mean values remain similar mostly because the DY clusters have a high abundance of high mass BSSs (i.e. the bright BSSs well above the PDF peak at low luminosities) and no steep decrease in the distribution like it was observed for the BSS masses of MP-DY clusters. On the other hand, the $r < 5r_c$ BSS PDFs do not show a significant change with the new random samples, which suggests that, for this particular MI GC sample, the difference in BSS masses should be more pronounced for the inner-most regions[4]. Nevertheless, the overall ”evolution” of the features in the PDFs remains valid for this random samples.

---

[4] We think this is an observational effect instead of a real physical property.

3.4.2.3 Analysis of MR GCs

The BSS PDFs for the MR group are shown in Figure 3.11. The analysis for this group of PDFs is very similar to the ones of the MP clusters. Indeed, while comparing the DY, DI and DO PDFs, we observe an overall evolution, at all cluster-centric distances, from a more narrow and concentrated structure peaked at low luminosities, into a less defined and more extended structure. We also observe that DI and DO clusters are more abundant in BSSs with $\Delta I \lesssim -1.5$. These differences translate nicely in the BSS mass distributions. Here we observe that the BSS mass distribution of DY clusters is strongly peaked at around ~1 $M_\odot$ and drops rapidly at M>1.1 $M_\odot$. The mass distribution for DI and DO clusters have instead an over-abundance of high mass BSSs, which drives the mean masses well above the mean BSS mass of DY clusters.

In summary, we are able to nicely link the observed BSS mass vs dynamical age correlation, to their observed luminosities and positions within the CMD. We note that we have not found in the literature any other studies that showed physical properties of BSSs (such as their stellar mass) translating into distinct features in the CMD. The exception is maybe for the isolated case of M 30 (Ferraro et al., 2009).

3.5 The Interpretation of the Low Luminosity Peak

The analysis of the BSS PDFs gave us some very interesting insights about the dependence of average BSS mass with the cluster dynamical age. Our general view is that DY clusters share similar properties of their BSS PDFs. In particular, they generally show a high concentration of BSSs populating a peak in the PDF at low luminosities (which usually translates into a low mass peak in the BSS mass distribution). Also, this structure tends to be more diagonal and elongated for MP and MI clusters (see Figure 3.8 and Figure 3.9), which is a result of the intrinsic shape of the stellar evolutionary tracks at such metallicities. The second important observation is that this structure seems less dominant as the clusters become more dynamically evolved. In DO clusters, we see a second extended component becoming more dominant. In Figure 3.12 we show a simplistic schematic illustration of what we have observed. The figure illustrates how the two different components become less and more dominant with dynamical age. The MP group BSS PDFs shown in Figure 3.8 are probably the most representative of this scheme, since they span the widest range in log(age/t_c) (i.e. dynamical age). On the other hand, the DY clusters from the MI and MR groups are all dynamically older than the DY clusters in the MP group, and that needs to be considered when comparing all dynamical age sub-groups.

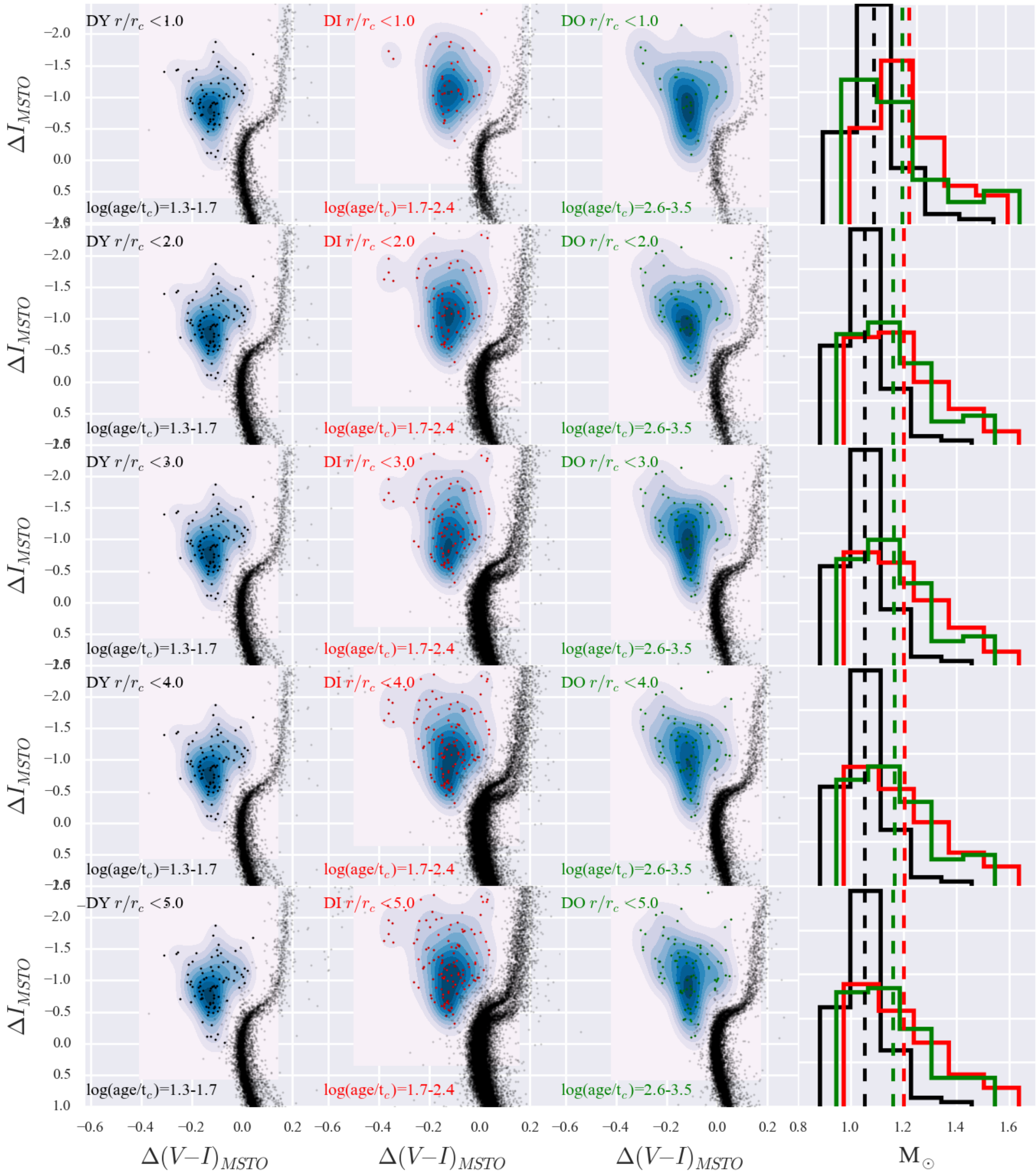

Figure 3.11: Same as Figure 3.8, but for the metal-rich GCs.

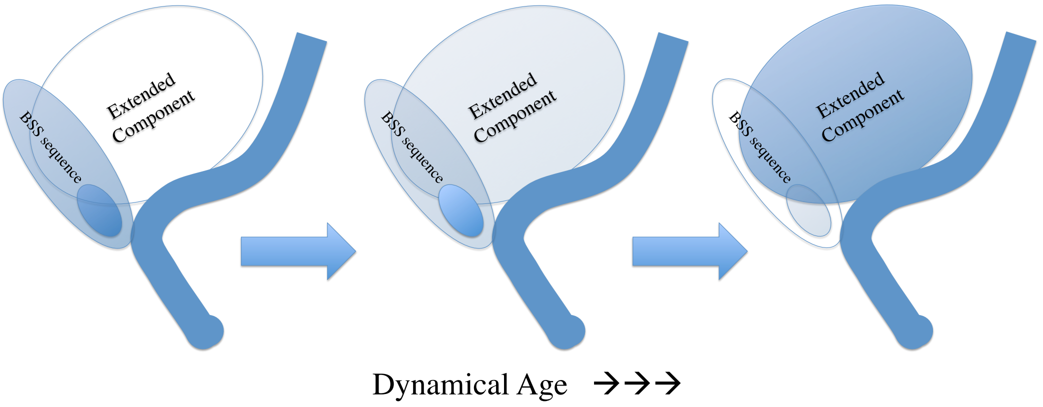

Figure 3.12: A simplistic schematic illustration of how BSSs seem to populate the CMD in the inner regions of our GC samples. There is a strong BSS sequence with a low luminosity peak that dominates early in the dynamical age, but becomes weaker as a second more extended component becomes dominant for dynamically older GCs.

In a recent work, Hypki & Giersz (2013) presented a large set of simulations of BSS formation using MOCCA (Giersz & Heggie, 2011) , which is a powerful code that combines the Monte Carlo method for the cluster evolutions with the FEWBODY (Fregeau et al., 2004) code to perform scattering experiments. They simulated the evolution of GCs and followed the dynamical interactions involved in BSS formation. One of their many results was that BSSs formed predominantly through an evolutionary channel (i.e. binary evolution resulting in a merger, and binary evolution resulting in Roche-Lobe overflow mass-transfer), and through the dynamical channel (i.e. dynamical encounters of binary+binary or binary+single). They found that the evolutionary channel is usually the more dominant and produces significantly more BSSs compared to the dynamical channels. Their simulations also predicted that the mass distribution of BSSs produced in both channels are very different. We show in Figure 3.13 a plot taken directly from their paper (Figure 6 in Hypki & Giersz (2013)). The plot shows the mass distribution of BSSs, normalized to the MSTO mass, for evolutionary merger products (EM, in red), evolutionary mass-transfer products (EMT, black) and for the combined sample of single+binary and binary+binary collisions (CBS+CBB, in blue). The key point here is that evolutionary BSSs have mass distributions that are strongly peaked at low masses, but drops to near zero for masses higher than $\sim$1.4 M_{MSTO} (i.e. $\sim$1.1 $M_\odot$ for M_{MSTO} =0.8 $M_\odot$). On the other hand, dynamical BSSs show a flat mass distribution. They explain that any MS star can be involved in CBS or CBB interactions, and therefore any mass is equally probable. They also find that the BSSs produced through the evolutionary channels come mostly from primordial unperturbed binaries. Such binaries would have to be in a tight orbit and have a mass ratio $q = M_1/M_2 \approx$1 in order to produce a BSS that is near twice the MSTO mass. These are actually very rare, and

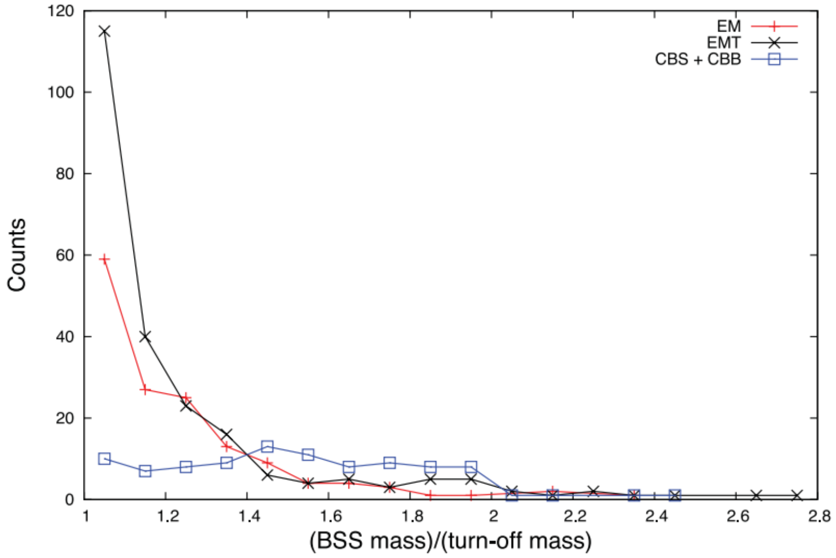

Figure 3.13: The mass distribution of MOCCA simulated BSSs, normalized to the MSTO mass, for evolutionary merger products (EM, in red), evolutionary mass-transfer products (EMT, black) and for the combined sample of single+binary and binary+binary collisions (CBS+CBB, in blue). The figure is taken directly from Figure 6 in Hypki & Giersz (2013).

instead most hard-binaries have lower mass-ratios, which results in a preference for BSS masses slightly above the MSTO mass.

We propose this scheme as an explanation for the low luminosity (and low mass) peak in the BSS PDFs. In other words, we propose that binary evolution is the major channel contributing to the observed low luminosity peak in the BSS PDFs. There are two major aspects that support this scenario: (i) The BSSs that populate the low luminosity peak also tend to produce a mass distribution strongly peaked at low masses. This is exactly what you would expect for a binary-evolution BSS population, according to the results of MOCCA. For the MP and MR clusters (see Figure 3.8 and Figure 3.11), we found that such distributions drop dramatically for M$\gtrsim$1.1 M$_\odot$ ($\sim$1.4 M$_{MSTO}$ for M$_{MSTO}$ =0.8 M$_\odot$). This is in good agreement with the approximate mass where EM and EMT BSSs become insignificant, according to the MOCCA results (see Figure 3.13). (ii) The low luminosity peak of the BSS PDFs becomes less dominant for dynamically older GCs, which also explains why the average BSS mass increases with dynamical age. If these BSSs are dominated by binary-evolution products, then DO clusters should be less efficient at producing BSSs from primordial binaries. In fact, studies show that GCs with denser cores have lower binary fractions, which suggests they get disrupted during the more frequent dynamical encounters (Milone et al., 2012).

In the current literature, the most complete census of binary fractions is the one of Milone et al. (2012). They used HST WFC/ACS data and calculated binary fractions

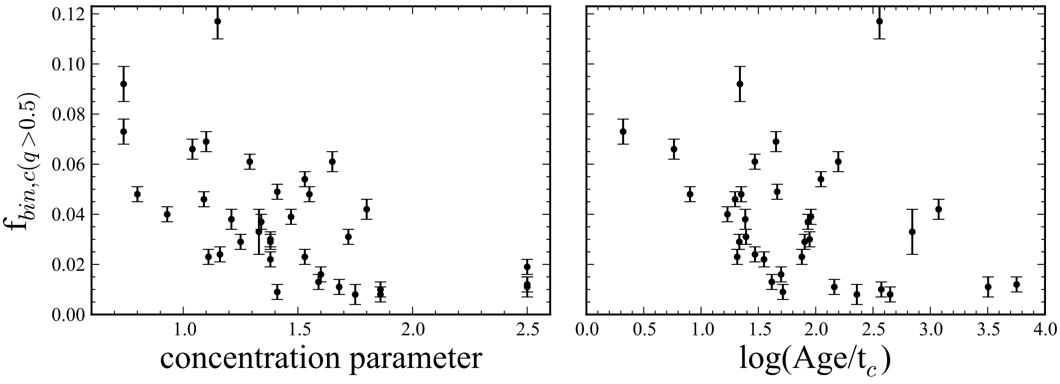

Figure 3.14: The core binary fractions for q >0.5 from Milone et al. (2012) versus the cluster concentration parameter (left panel) and the core dynamical age (right panel). We plot the 36 GCs from our sample that are also in the Milone et al. (2012) data set.

in 59 GCs by studying the binary-sequence on the MS as a function of radial location within the cluster, from the central core to beyond the half-mass radius. We show in Figure 3.14 the core binary fractions from Milone et al. (2012) versus the cluster concentration parameter (left panel) and the core dynamical age (right panel) for all GCs in common between our sample and the Milone et al. (2012) data set. The Figure confirms that the core binary fraction anti-correlates with the dynamical age. In summary, we conclude that there is a significant amount of evidence to suggest that the low luminosity peak observed in the BSS PDFs is dominated by binary-evolution products. Additionally, our results suggest that this feature becomes less abundant inside the inner regions of dynamically older GCs, because of their low binary fractions. Considering the predicted flat mass distribution of dynamical BSSs (see Figure 3.13) and the observed mass distributions from Section 3.4.2, we find more appropriate to say that binary-evolution products cannot be fully absent in DO clusters, and instead they only seem to become less dominant compared to dynamical BSSs.

3.6 The BSS Formation Channels versus Dynamical Age

We consider now the two-component scheme described in Figure 3.12 and asses the possibility that the dynamical channels are a significant contribution to the proposed extended component. We use the single+single core collision rates from Leigh et al. (2011). These rates represent the inverse of the average time for any two single stars to experience a direct collision in the cluster core. We note that single+single collisions are actually the least probable dynamical encounter, as you expect many more collisions involving binaries because of their larger cross sections. We should consider therefore

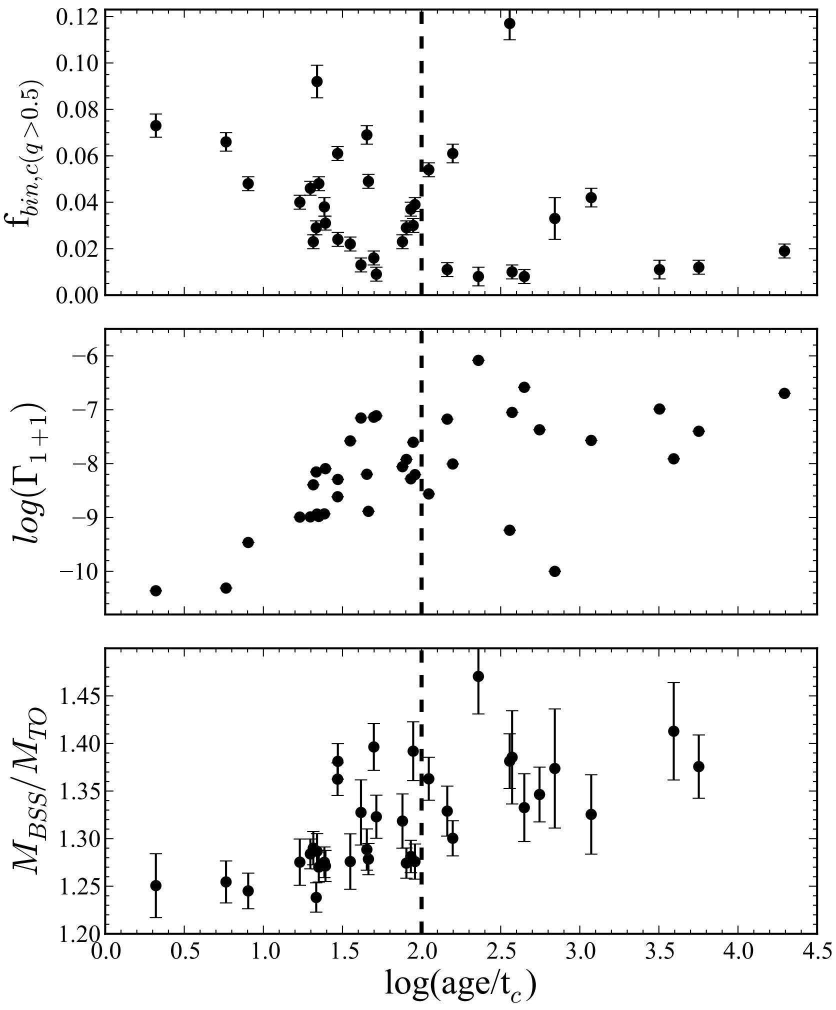

Figure 3.15: *Top*: The core binary fractions from Milone et al. (2012) versus the cluster dynamical age for the GCs in common with our sample. *Middle*: The single+single collision rates from Leigh et al. (2011) versus dynamical age for all GCs in our sample. *Bottom*: The average normalized BSS mass for samples inside $3r_c$ versus dynamical age for GCs with more than 8 BSSs in the radial bin. The vertical dashed line marks the value log(age/t$_c$)=2.0, which approximately corresponds to the dynamical age where binary fractions become small and collisions rates become important.

that single+single collision rates are somewhat of a lower limit for the collision rates of binary+single and binary+binary, yet they should still be appropriate to use a a proxy.

We plot in Figure 3.15 the core binary fractions, the core collisions rates, and the average normalized BSS mass for the $r < 3r_c$ sample. The vertical dashed line marks the value log(age/t$_c$)=2.0, which approximately corresponds to the dynamical age where binary fractions become small and collisions rates become important. A simple qualitative corollary from the MOCCA simulation BSS mass distributions of Figure 3.13 is that reducing binary products while increasing dynamical products should smoothly increase the average BSS mass. This is in perfect agreement to what we observe in the bottom panel of Figure 3.15. We believe that if primordial binary-evolution were the only important formation channel, then you cannot explain the increase in average BSS mass for GCs with low binary fractions. Figure 3.13 then strongly supports the contribution of dynamical BSSs within the cores of these GCs. We note that, as always in science, correlations are not necessarily indicating causation and in particular these correlation in the plot have to be taken with serenity. Nevertheless, we think that our conclusions are reasonable and in fact very robust. The binary channel is widely accepted or at least considered by many authors to be one of the dominant BSS formation scenarios (Geller & Mathieu, 2011; Knigge et al., 2009; Leigh et al., 2013). Yet, there is no strong consensus on whether different formation channels are dominant in *different* clusters, or whether different formation channels act simultaneously *within the same* clusters. In particular, our results suggest that both channels act simultaneously and that the dynamical channel becomes more significant in the cores of DO clusters.

Bibliography

Baldwin, A. T., Watkins, L. L., van der Marel, R. P., et al. 2016, arXiv:1606.00836

Dotter, A., Chaboyer, B., Jevremović, D., et al. 2008, The Astrophysical Journal Supplement Series, 178, 89-101

Dotter, A., Sarajedini, A., Anderson, J., et al. 2010, The Astrophysical Journal, 708, 698

Ferraro, F. R., Beccari, G., Dalessandro, E., et al. 2009, Nature, 462, 1028

Ferraro, F. R., Lanzoni, B., Dalessandro, E., et al. 2012, Nature, 492, 393

Fiorentino, G., Lanzoni, B., Dalessandro, E., et al. 2014, The Astrophysical Journal, 783, 34

Fregeau, J. M., Cheung, P., Portegies Zwart, S. F., & Rasio, F. A. 2004, Monthly Notices of the Royal Astronomical Society, 352, 1

Geller, A. M., & Mathieu, R. D. 2011, Nature, 478, 356

Giersz, M., & Heggie, D. C. 2011, Monthly Notices of the Royal Astronomical Society, 410, 2698

Harris, W. E. 2010, arXiv:1012.3224

Hypki, A., & Giersz, M. 2013, Monthly Notices of the Royal Astronomical Society, 429, 1221

Hypki, A., & Giersz, M. 2016, arXiv:1604.07033

Hypki, A., & Giersz, M. 2016, arXiv:1604.07054

Knigge, C., Leigh, N., & Sills, A. 2009, Nature, 457, 288

Lanzoni, B., Sanna, N., Ferraro, F. R., et al. 2007, The Astrophysical Journal, 663, 1040

Leigh, N., & Sills, A. 2011, Monthly Notices of the Royal Astronomical Society, 410, 2370

Leigh, N., Knigge, C., Sills, A., et al. 2013, Monthly Notices of the Royal Astronomical Society, 428, 897

Lovisi, L., Mucciarelli, A., Lanzoni, B., et al. 2012, The Astrophysical Journal, 754, 91

Milone, A. P., Piotto, G., Bedin, L. R., et al. 2012, Astronomy & Astrophysics, 540, A16

Sirianni, M., Jee, M. J., Benítez, N., et al. 2005, Publications of the Astronomical Society of the Pacific, 117, 1049

Stępień, K., & Kiraga, M. 2015, Astronomy & Astrophysics, 577, A117

Chapter 4

Spectroscopic Dynamical Characterization of BSSs in NGC 3201, NGC 5139 and NGC 6218

The rather complex picture of spectroscopic properties of BSSs described in Section 1.4 calls for larger surveys sampling dynamical properties of BSSs with a homogeneous dataset in order to get a wider picture of the BSS formation processes and to improve on the statistical significance of previous results. In that context, we carry out this study to set constraints on the formation mechanisms of BSSs in GCs based on their spectral characteristics. We select three GCs: NGC 3201 ($\alpha_{2000}=$10h17m36.82s, $\delta_{2000}=-$46d24'44.9"), NGC 6218 ($\alpha_{2000}=$16h47m14.18s, $\delta_{2000}=-$01d56'54.7"), and NGC 5139 (ωCen; $\alpha_{2000}=$13h26m47.24s, $\delta_{2000}=-$47d28'46.5"). Their BSS populations have not been previously characterized spectroscopically, except for the case of ωCen as described in Section 1.4.

This Chapter is organized as follows: Section 4.1 describes the observations and data reduction process. Section 4.2 analyzes the radial and rotational velocities of BSSs. In Section 4.3 we discuss the properties of BSSs in the context of our results, and summarize the main result and conclusions in Section 4.4.

4.1 Observations and Data Reduction

4.1.1 Instrumental Setup and Target Selection

The data used in this work were obtained as part of the observing program CNTAC2012A-101 using the multi-slit mode of the IMACS f/4 spectrograph mounted on the 6.5-meter Baade Telescope at Las Campanas Observatory. The observations were performed on the night of March 21st, 2012, with overall good sky conditions and an average seeing of 0.6". Multi-slit masks were cut to obtain spectra of 42, 61 and 34 BSS candidates in NGC 3201, ωCen and NGC 6218, respectively. The slit mask configurations were designed such that the center of each GC was placed near the slit-mask center in order to homogeneously obtain spectra of BSS candidates located at as much as $\sim 10'$ of radial cluster-centric distance. In this manner we radially sampled the targets up to approximately 8.5, 4.6, and 6.8 r_c in NGC 3201, ωCen, and NGC 6218, respectively. The science observations consisted of 20-minute sub-exposures, from which we obtained total exposure times of 1h:40m for NGC 3201 and NGC 6218, and 1h:20m for ωCen, providing a mean signal-to-noise ratio of S/N ≈ 70. Interspersed between the science target observations, we also obtained spectra for two photometric standards, five rotational velocity standards and arc calibration frames. Standard bias and flat-field frames were obtained at the beginning and at the end of the night. The instrumental spectrograph configuration for all multi-object science exposures consisted of 4" long and 0.7" wide slits and the 1200 l/mm grism blazed at 17.45°, which yields a wavelength coverage of ~3600-5200 Å with a spectral resolution of $R \approx 10000$ and a resulting velocity resolution of ~15 km/s. The corresponding instrumental dispersion relation is ~0.2 Å/pix.

The spectroscopic BSS target selection was performed on F606W (~V) and F814W (~I) band photometric catalogs from the *HST/ACS Galactic GC Survey* (Sarajedini et al., 2007) combined with catalogs generated using wide-field imager (WFI) data obtained from the ESO science archive[1] plus a large WFI photometric catalog of ωCen available online (Bellini et al., 2009). The reason for combining HST and WFI catalogs is that the wide field channel (WFC) of the ACS camera samples only the inner $\sim 3' \times 3'$ of the target GCs while the WFI data extends well outside the $\sim 15' \times 15'$ field of view of the IMACS f/4 camera. By combining these two datasets we guarantee homogeneous sampling of the dense core regions and the outskirts of each GC. The BSS candidates were selected from making color and magnitude cuts in the CMDs of each GC. The selection criteria is the one from Leigh et al. (2009) which uses the V and I filter magnitudes to determine regions in the CMD that are exclusive to specific stellar evolutionary phases. These

---

[1] http://archive.eso.org

selection criteria and the physical limits of the mask design, set by the slit length and width, resulted in a final selection of 137 BSS candidates. Figure 4.1 shows the CMDs of all three GCs and the spatial distribution of all photometrically selected BSS candidates using HST/ACS and ESO/WFI data.

4.1.2 Data Reduction

The reduction of the data was performed in different levels in order to obtain 1-dimensional spectra for each individual BSS candidate from the original frames that contain the multi-slit exposures. The major part of this work was performed using the COSMOS reduction software (v2.18)[2], which is a suite of programs dedicated for the reduction of multi-slit spectroscopy data obtained with the IMACS instrument on the Baade Magellan Telescope. Standard bias and flat-field calibration is performed with COSMOS sub-routines.

This package allows for an accurate prediction of the location of spectral features of individual slits thanks to a series of alignment and calibration procedures based on raytracing models of the instrument. These models provide a map that is accurate down to $\sim 2-3$ pixels. The program then uses the arc frames to correct these predictions to an accuracy of a fraction of a pixel, constructing the final field distortion map that is then used for the science data wavelength calibration. The final wavelength solution we obtain is accurate to about $\sim 0.2-0.3$ pixels for all targets. We then apply the corresponding calibrations and subtract the sky through different tasks in COSMOS and get the individual 2-dimensional spectra for each target. These spectra are then resampled to a linear wavelength scale with a dispersion of 0.1 Å/pix. The final 1-dimensional extraction is then performed using IRAF[3] task APALL. We show in Figure 4.2 the Hβ and Mgb triplet spectral regions for different BSSs spanning the representatives values of S/N, as obtained from its distribution shown in Figure 4.3. We discard spectra with S/N<20 and others affected by contamination, resulting in sample sizes of 41, 49 and 32 BSS candidates in NGC 3201, ωCen and NGC 6218, respectively.

---

[2] The routines were obtained through the Carnegie Observatory Software Repository, located at http://code.obs.carnegiescience.edu/cosmos.

[3] IRAF is distributed by the National Optical Astronomy Observatories, which is operated by the Association of Universities for Research in Astronomy, Inc. (AURA) under cooperative agreement with the National Science Foundation

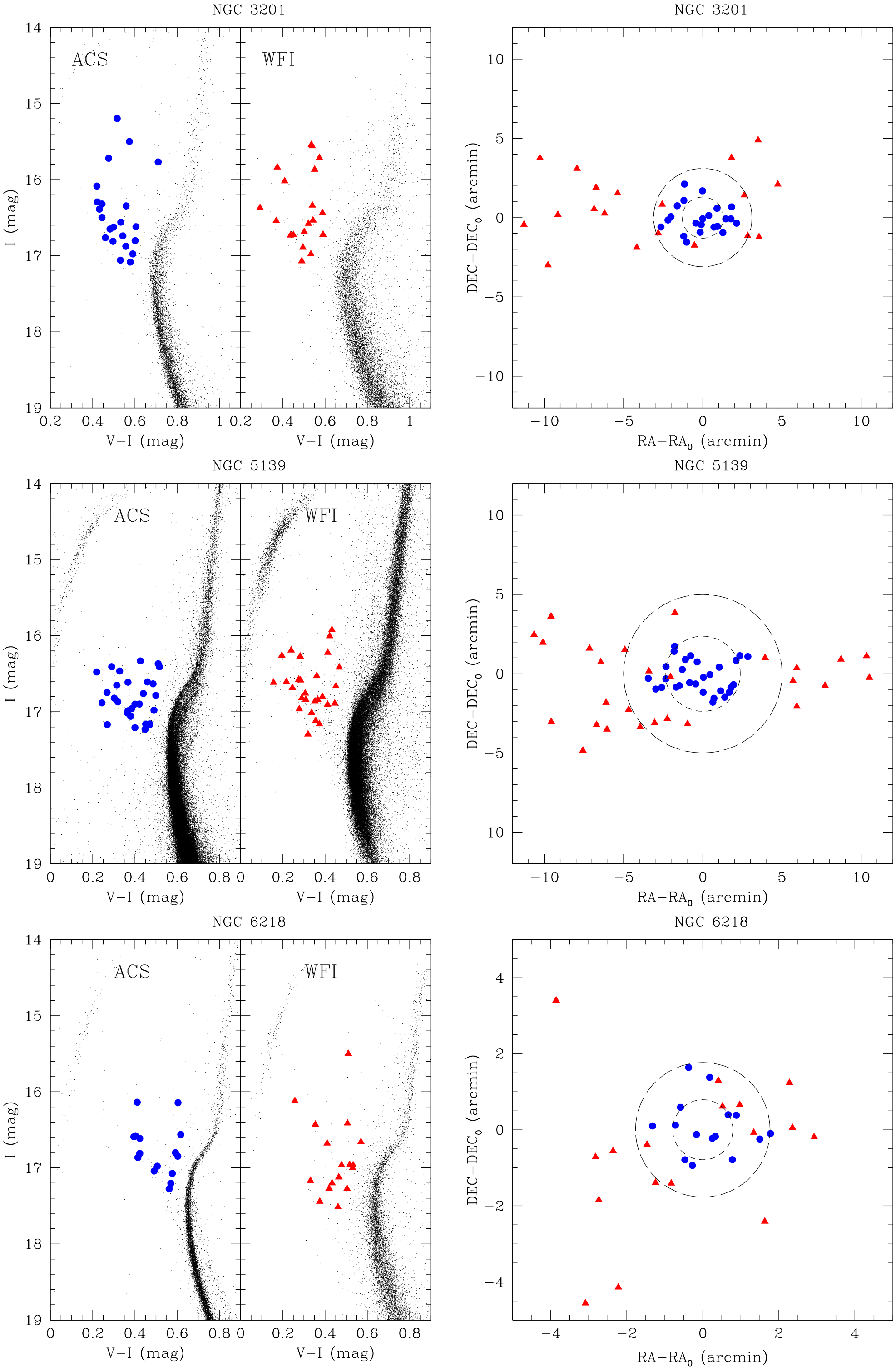

Figure 4.1: (*Left column*): Color-magnitude diagrams (CMDs) of our target clusters NGC 3201 (*top row*), NGC 5139 (*middle row*), and NGC 6218 (*bottom row*) obtained from ACS photometry (*left sub-panels*) and WFI photometry (*right sub-panels*), with the selection of BSS candidates labeled as circles and triangles for the ACS (*blue circles*) and WFI data (*red triangles*), respectively. (*Right column*): Spatial locations of the BSSs in each GC with respect to the cluster center position. Inner and outer dashed circles correspond to the cluster core radius and half-light radius, respectively, as reported in Harris (1996).

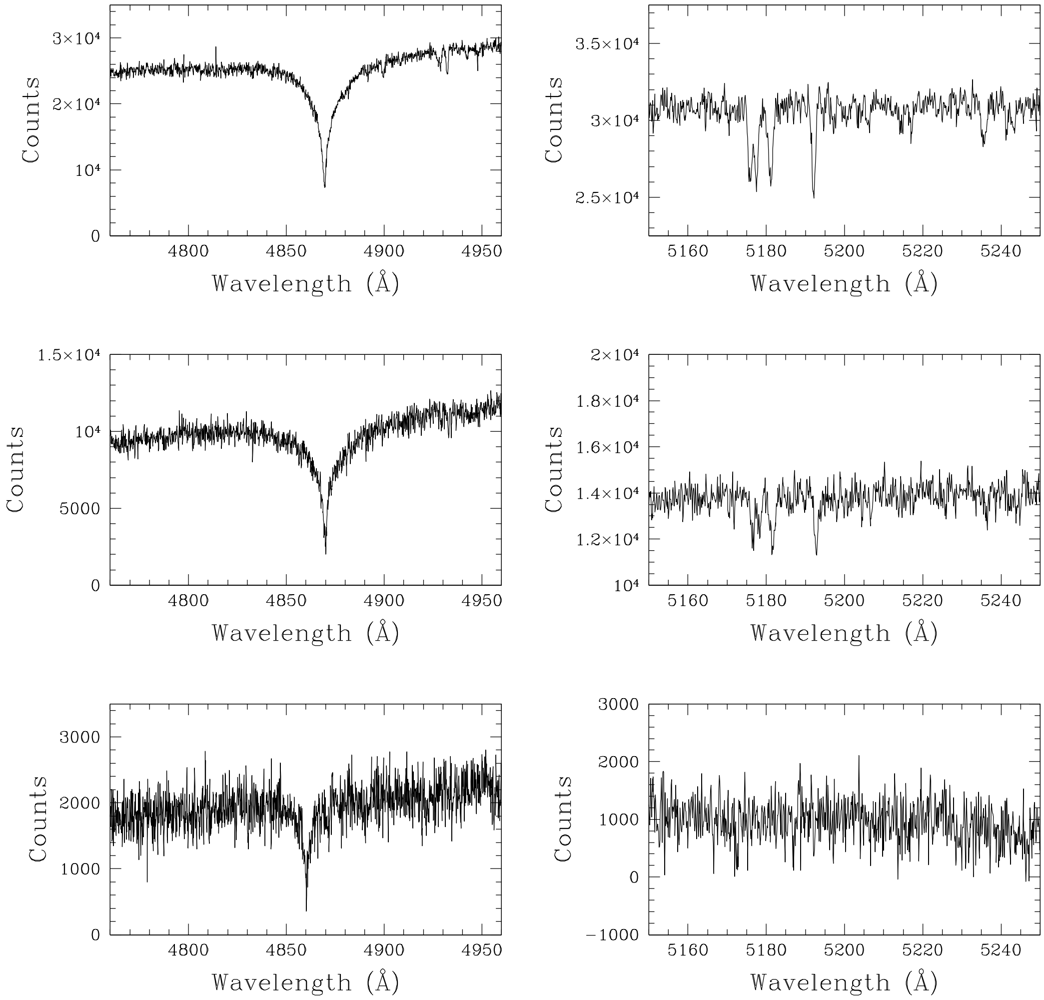

Figure 4.2: Example spectra of BSSs for spectral ranges around Hβ (*left column*) and the Mg*b* triplet (*right column*). We show three representative cases corresponding to approximately the maximum, the median, and the minimum values of the S/N distribution, illustrated in Figure 4.3. The top panels correspond to a S/N≈160, the middle panels are for a S/N≈70 and the bottom panels correspond to a S/N≈20.

4.2 Analysis

4.2.1 Radial Velocities and Cluster Membership

We perform radial velocity measurements for all our spectra in order to study the membership likelihood and to compare our measurements with the GC radial velocity values found in the literature. We use the IRAF task FXCOR (Tonry & Davis, 1979) to compute radial velocities via Fourier cross correlation between the science data and a set of template spectra. As templates we use the high-resolution ($R = 42000$) spectra from

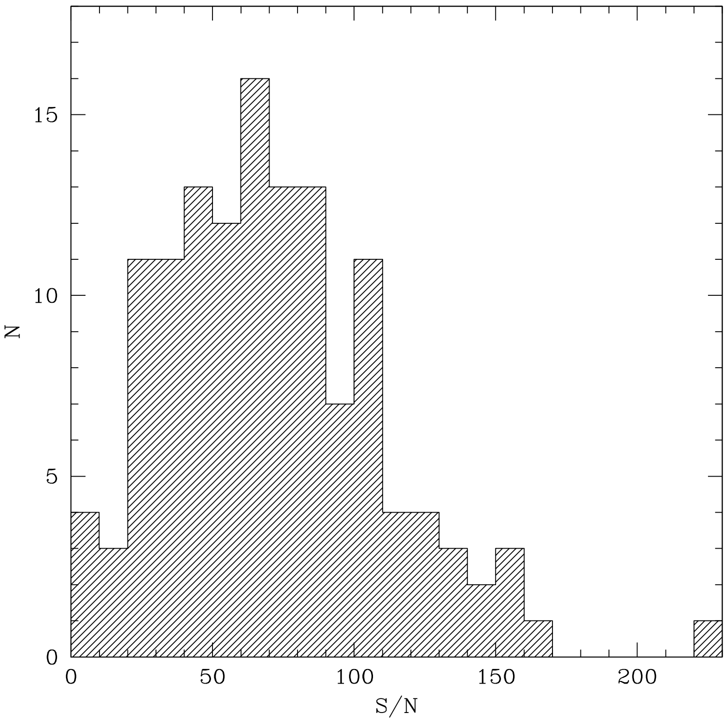

Figure 4.3: The distribution of the median signal-to-noise (S/N) values of all our sample BSS candidate spectra. Approximately half of our spectra have S/N values larger than ~ 70 and 20% of them have S/N > 100.

the ELODIE library (Prugniel & Soubiran, 2001). In most cases, strong absorption regions like the Balmer lines and the Mg*b* triplet region were used in the cross correlation and for all our targets we avoided spectral regions affected by cosmic-ray hits and the CCD inter-chip gaps. The radial velocities obtained are however relative to the frame of reference of the template spectra used in the task FXCOR, therefore we repeat the process with our observed standards stars and compare the radial velocities obtained against those in the literature. This way we can calculate the radial shifts of the templates themselves and use this to calibrate the values obtained for each BSS. The final laboratory restframe radial velocity was calculated by taking the error-weighed mean of five measurements from different templates. We used the IRAF task RVCORRECT to obtain the final heliocentric radial velocities by using the date, location, and sky coordinates of the observations to correct for the Earth's relative velocity against the Sun. The final heliocentric radial-velocity distributions of our sample BSS candidates are shown in Figure 4.4 for each GC.

The corresponding heliocentric radial velocities of NGC 3201, ωCen, and NGC 6218 from Harris (1996) are shown as long-dashed lines while the mean values of our measurements are shown as short-dashed vertical lines. For all GCs, we find mean radial velocity values that are not more than ~4-8 km s^{-1} different from the literature values. We use our mean radial velocities to study the cluster membership of each BSS candidate. These values are $502.4 \pm 11.2, 227.2 \pm 26$, and -44.6 ± 14.2 km s^{-1} for NGC 3201, NGC 5139, and NGC 6218, respectively[4], where the errors correspond to 1σ. We adopt a 3-σ cut and label outliers rather than eliminating them from the sample, in order to individually check their membership likelihood. In Figure 4.4, all outliers are labeled and the non-filled bins show stars with radial velocities off the limits of the figure. After this cut, we are left with 36, 47 and 31 BSSs in NGC 3201, ωCen and NGC 6218 respectively. Overall we find that ~93% of our BSS candidates show radial velocities consistent with the system velocity of their parent GC. This suggests that the field star contamination is low (few %), indicating that BSSs are majorly exclusive elements of dense stellar environments as found in GCs. The outliers found in each sample can be divided arbitrarily into two groups: the ones with radial velocity differences larger than 100 km s^{-1} with respect to the mean value, and the ones in which the difference is less than that. We choose to further include outlier stars from the second group under the criteria that these could be BSSs that formed in strong dynamical events which then transferred large amounts of momentum into kinetic energy. These are star A5 and C1 from NGC 3201 and NGC 6218, respectively, which will be also studied in order to check their role in the final dynamical distribution functions for each GC.

The bulk of the distributions in Figure 4.4 is, in all cases, fairly symmetrically distributed around the mean value, with very few outliers. The width of the distributions is similar for NGC 3201 ($\sigma_{\rm RV} = 11.2$ km s^{-1}) and NGC 6218 ($\sigma_{\rm RV} = 14.2$ km s^{-1}), while ωCen shows about a factor of 2 larger value, i.e. $\sigma_{\rm RV} = 26$ km s^{-1}. This is qualitatively consistent with the central velocity dispersions reported in Harris (1996), i.e. $\sigma_0 = 5.0$ (NGC 3201), 16.8 (NGC 5139), and 4.5 km s^{-1} (NGC 6218). However, the radial velocity dispersions are systematically larger than the central parts of the constituent stellar populations in each GC, which interestingly could be explained by dynamical interactions such as those that might form a BSS, or by the fact that BSSs are likely to be part of binary systems, and therefore their radial velocities could be enhanced by orbital motion. This intriguing result requires confirmation with larger BSS samples testing whether BSSs have different radial velocity dispersion profiles than the rest of the GC stellar population.

4.2.1.1 Field Stars Contamination

The fact that we are including stars such as A5 and C1 into our BSS sample calls for a better understanding of how susceptible our sample is to field stars contamination. In order to get an approximate idea we have checked the radial velocity distributions

---

[4] The corresponding median values are 500.2, 225.5 and -47.3 km s^{-1}, respectively.

of field stars using the galactic model of Robin et al. (2003) and found that the field stars in the line of sight of NGC 3201 and NGC 5139 have radial velocity values ranging $-50 < v_r < 150$ km s^{-1} and $-100 < v_r < 100$ km s^{-1}, respectively. These velocities are clearly distinct from the systemic velocities found for these two globular clusters, and, therefore, the probability of our BSSs being false positives is very low. This is also the case for outliers such as star A5 which is also highly inconsistent with the radial velocity distribution of field stars along that line of sight. For field stars along the NGC 6218 line of sight we find model predicted radial velocities in the range $-150 < v_r < 150$ km s^{-1} (which includes the radial velocity found for star C1), even with a peak in their distribution function around -40 km s^{-1}, which is very similar to what is found for the mean radial velocity of BSSs in NGC 6218. Hence, the BSS radial velocity distribution in this globular cluster requires particular attention. For this we have searched the proper motion data catalog of Zloczewski et al. (2012) and found measurements for 16 out of our 32 BSSs studied in NGC 6218. All of them show proper motions consistent with being cluster members. We then check the radial velocity distribution of these 16 BSSs and find that they populate the entire radial velocity distribution found for the entire sample of 32 BSSs. A Kolmogorov-Smirnov test shows that the sample of proper-motion confirmed BSSs and the entire sample are likely to have identical radial velocity distributions with a p-value > 0.8. This, of course, does not completely rule out the possibility of including field stars in our sample, yet if there happened to be such contaminants, these results suggest that they would consist of a minor fraction. We do not have proper motion information for star C1 and so a final conclusion cannot be drawn concerning its membership probability. We note that this is the innermost star in the sample, which alone favours the cluster membership option. The inclusion of A5 and C1 in the confirmed BSS sample must, therefore, be handled with care.

4.2.2 BSS Rotational Velocities

4.2.2.1 pPXF: The Code

Rotational velocities are obtained for all our sample star spectra by using the penalized pixel fitting algorithm called pPXF, which is an IDL program to extract the kinematics of stellar populations from integrated-light absorption-line spectra of galaxies. This software implements the penalized pixel-fitting method developed by Cappellari & Emsellem (2004) as a way to recover the central velocity, v, and the standard deviation, σ, as well as high-order moments such as skewness and kurtosis from the line-of-sight velocity distribution (LOSVD) through a Gauss-Hermite expansion of the absorption-line

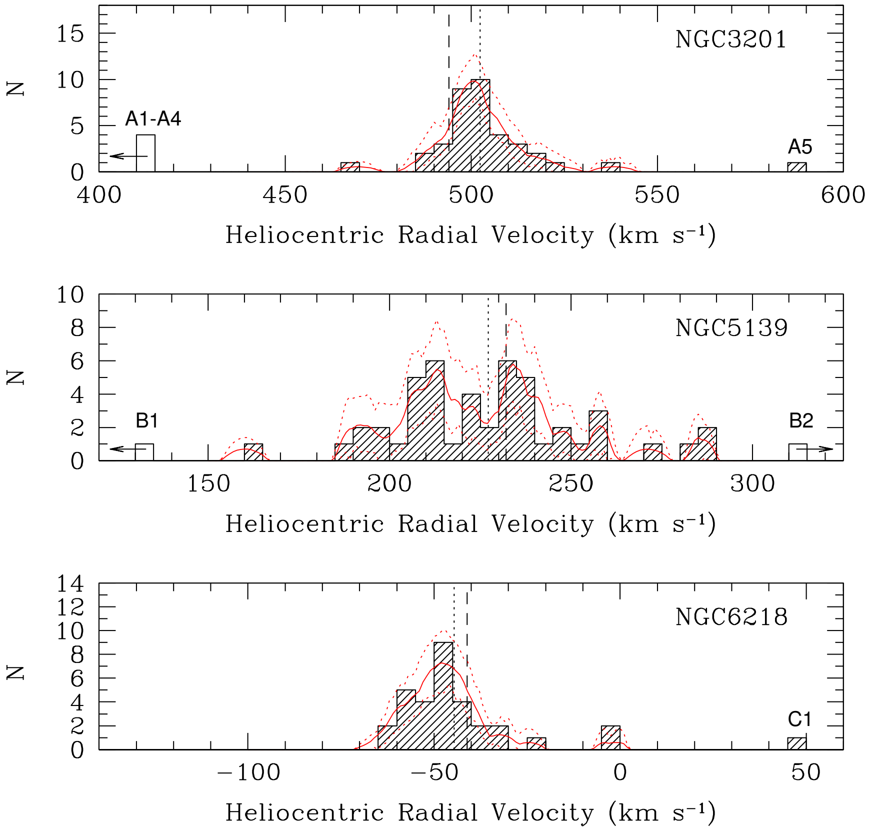

Figure 4.4: Radial velocity distributions of the BSS candidates in each GC. The long-dashed lines mark the values of the GC radial velocities given in Harris (1996), while the short-dashed vertical lines are the median values obtained from our data. The solid red line shows a non-parametric Epanechnikov-kernel probability density estimate with 90% confidence limits represented by the dotted red lines. The BSSs that have odd velocities are labeled in the figure. The non-filled bins correspond to BSS candidates with odd velocities out of the limits of the figure. A1, A2, A3 and A4 have velocities between 25 and 56 km s^{-1}. B1 and B2 have velocities of 15.6 and 360.6 km s^{-1} respectively.

profile of the following form:

$$\mathcal{L}(\nu) = \frac{e^{-(1/2)y^2}}{\sigma\sqrt{2\pi}}\left[1 + \sum_{m=3}^{M} h_m H_m(y)\right] \tag{4.1}$$

where ν is the frequency, $y = (\nu - v)/\sigma$, H_m are Hermite polynomials and $\mathcal{L}(\nu)$ is the LOSVD. The program uses "initial guess" input values of v and σ to convolve template spectra in order to fit the object spectra. The fitting consists of a nonlinear least-squares optimization of the parameters $v, \sigma, h_3, ..., h_M$. The code then uses a penalty function, derived from the deviation of the object line profile from a Gaussian, which is added to the χ^2 of the fit. Therefore, a penalized χ^2 is calculated as:

$$\chi_p^2 = \chi^2(1 + \lambda^2\mathcal{D}^2) \tag{4.2}$$

where $\mathcal{D}^2$ is the penalty function, that according to the authors can be approximated by

$$\mathcal{D}^2 \approx \sum_{m=3}^{M} h_m^2, \tag{4.3}$$

and λ, which is a *bias* parameter chosen by the user. The fitting is iterated until the variance is minimized and the fit converges. This pPXF procedure predisposes the solution with a single Gaussian when the S/N is low, while it is able to recover the higher-order moments of the absorption line spectrum when the S/N is high. For more details on the algorithm the reader is referred to Cappellari & Emsellem (2004).

4.2.2.2 pPXF: Understanding Systematics and Capabilities through Monte-Carlo Simulations

The *bias* parameter described above must be adjusted delicately to prevent the pPXF code from losing the high-order features in the object spectrum. For this we preformed a series of Monte-Carlo simulations in which we used a representative spectrum from our data to inspect the behaviour of the penalty function. First we used pPXF to fit a LOSVD to the object spectrum using no penalty function (*bias*=0) finding the unbiased values of (h_3, h_4). We then used these values as input and ran pPXF several times, each time convolving the object spectrum with a successively larger $\sigma_{\rm LOSVD}$ kernel. We repeated this process for different values of the *bias* parameter and found the maximum penalty value such that, for $\sigma > 3\times$(velocity scale), which is the lower limit at which the program becomes insensitive to any deviation from a Gaussian absorption profile at any S/N (Cappellari & Emsellem, 2004), the mean difference between the output and the input parameters is well within the scatter of the simulation. We then choose this maximum value as the *bias* parameter. This is illustrated in Figure 4.5 for two cases: one with a low penalty (*bias* = 0.1) and one with an overly high penalty (*bias* = 0.4). We observe that, as expected, a too large penalty can make the code lose information on the high-order features of the spectrum, such as h_3 and h_4. Our analysis shows that the value *bias* = 0.2 gives the best results. We use this *bias* value throughout all subsequent pPXF runs.

The next step is to test the stability of the solution when varying the amount of spectral range used by the fit. For this we create an artificial single Gaussian absorption line with a FWHM = 0.3 Å, which corresponds to the instrumental profile of the IMACS spectra, and add poisson noise to obtain S/N = 70 (see Figure 4.3). We then perform the same simulation as above, i.e. we convolve the absorption line to reproduce an arbitrary LOSVD and then try to recover the parameters using the same original artificial line as a template. The key variable here is the amount of pixels (i.e. continuum) that we include

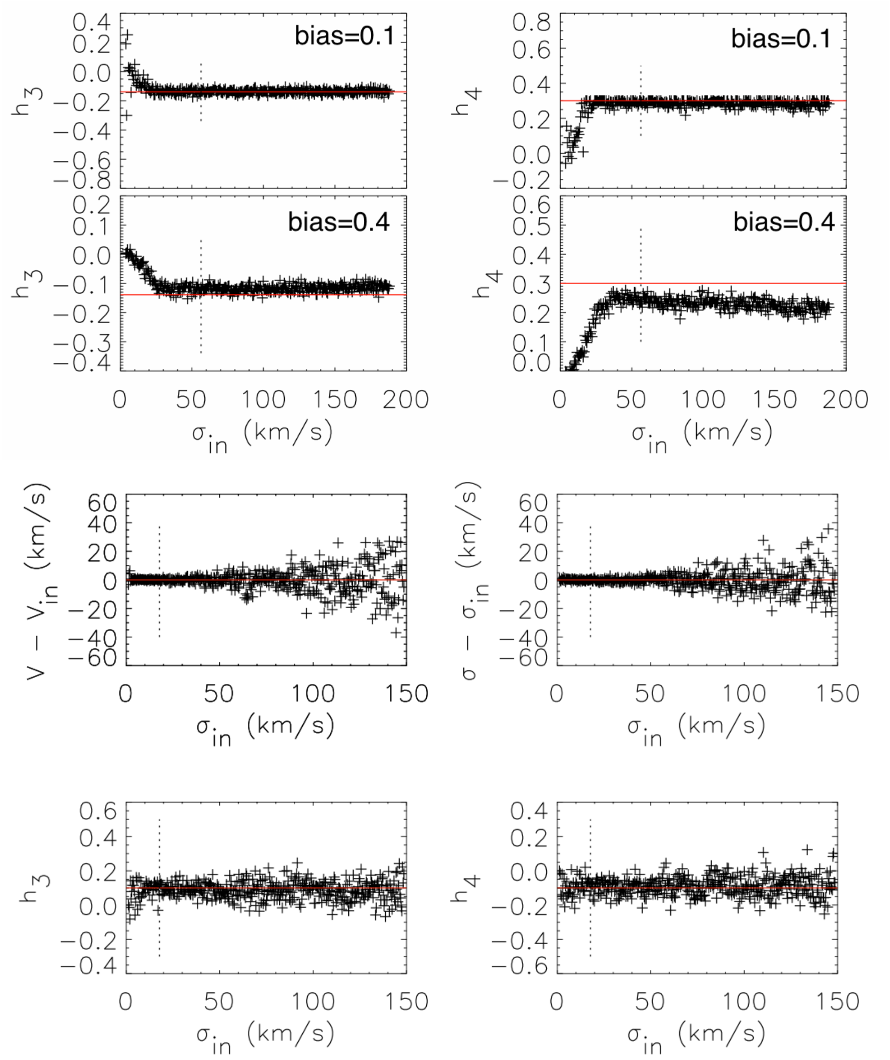

Figure 4.5: (*Top panels*): Monte-Carlo simulations using pPXF for estimating a proper *bias* parameter. Plotted are the recovered Gauss-Hermite moments h_3 and h_4 as a function of the input velocity dispersion $\sigma_{\rm in}$. The upper panels show the results for a low value of the *bias* parameter (0.1), while the bottom panels show the corresponding plots for a high *bias* value (0.4). The code is very efficient in recovering the input values in the case of a low *bias* parameter. The lower plots show the same experiment when using a high value for the *bias* parameter and illustrate clearly that the algorithm underestimates the values of the high-order features if the penalty is too large. In all cases the red line indicates the real value of the LOSVD and the vertical dashed lines mark the 3×(velocity scale) limit, which is the point when the code starts becoming insensitive to any Gaussian deviation. (*Center and bottom panels*): Results of the measurements of the LOSVD parameters (v, σ, h_3, h_4) for different input values of σ. For all plots the red line marks the input values of the LOSVD and the vertical dashed line is the 3×(velocity scale) limit, which is where the code starts becoming insensitive to any Gaussian deviation.

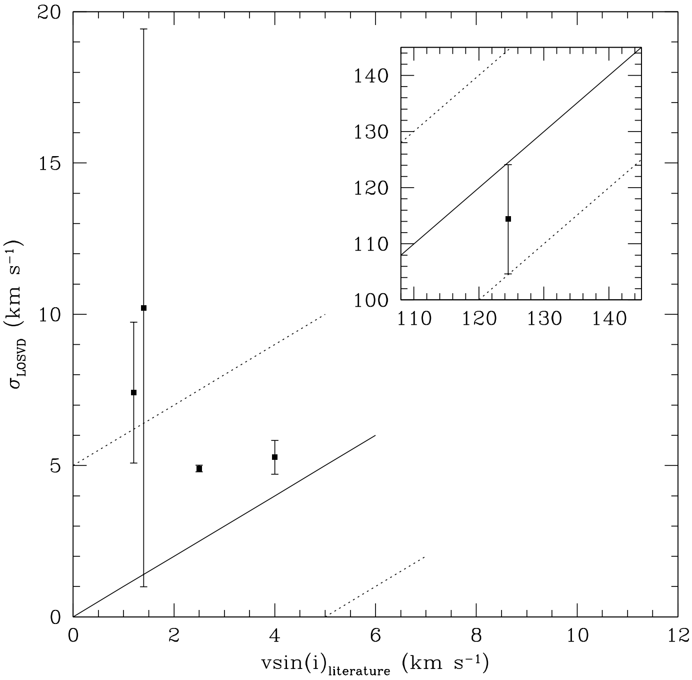

Figure 4.6: Comparison of the σ_{LOSVD} values obtained with pPXF against literature values of $v\sin(i)$ for our rotational velocity standard stars. The solid line shows the unity relation and the dashed lines show the ±5 km s^{-1} typical error range found for low rotational velocities. The small inset panel shows the same comparison for the fastest rotating standard star and the dashed lines show the ±20 km s^{-1} typical error range found for high rotational velocities, i.e. $\sigma > 100$ km s^{-1}.

in the fit. The spectral resolution of our resampled IMACS data is 0.1 Å/pix. Thus, a typical fitting range of 100 pixels corresponds to 10 Å. We find that for different spectral ranges the code is able to recover v and σ to within about ±20 km s^{-1} when the absorption line is broader than $\sigma \geq 120$ km s^{-1}, and to within about ±5 km s^{-1} when the absorption line has $\sigma < 100$ km s^{-1}. The bottom panels in Figure 4.5 show the results from one of these simulations for a spectral range of 100 Å. This result is stable for spectral ranges between approximately 70 and 300 Å. For smaller and larger spectral ranges the code begins to produce uncertainties in v and σ close to ±40 km s^{-1} for absorption lines with $\sigma \geq 100$ km s^{-1}.

4.2.2.3 Measuring $v\sin(i)$ of BSS candidates

The broadening of the absorption lines depends on the stellar rotational velocity and the viewing angle of the rotational axis. Here we calculate the projected rotational velocities by adopting the relation:

$$v\sin(i) = \alpha\cdot\sigma_{\text{LOSVD}} \tag{4.4}$$

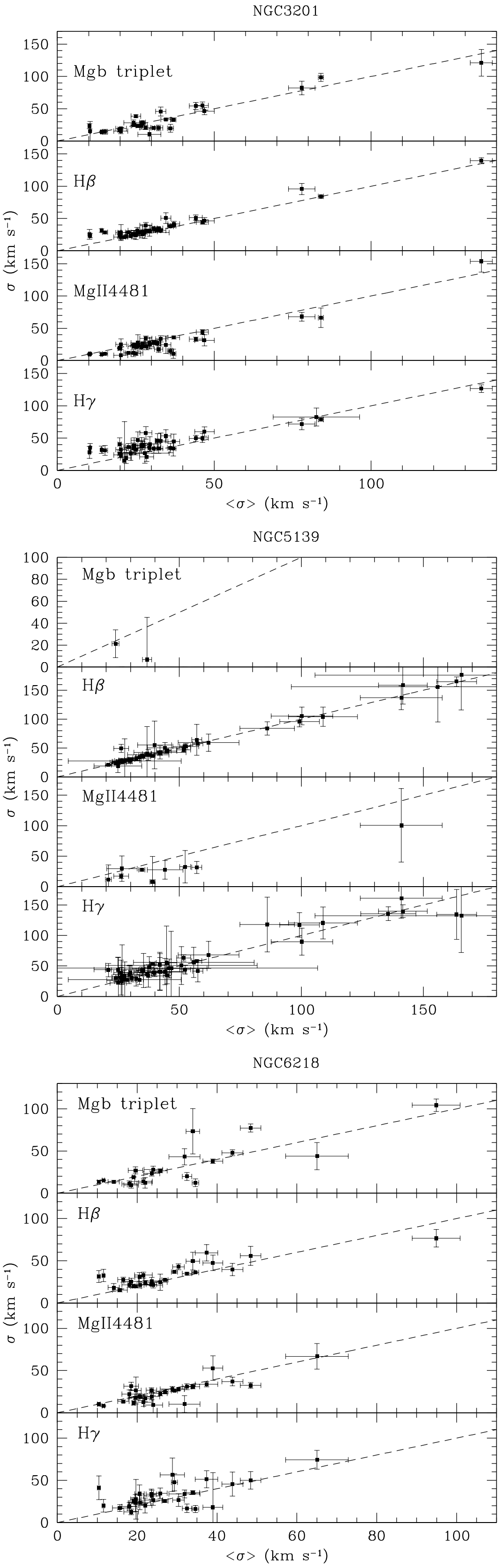

Figure 4.7: Comparison of the final mean $\langle\sigma\rangle$ values versus the individual σ measurements obtained at different spectral regions for all the BSSs candidates in NGC 3201 (*top panel*), NGC 5139 (*middle panel*), and NGC 6218 (*bottom panel*). The dashed lines show the unity relation in all panels.

Table 4.1: Sample properties of observed rotational velocity standards

Star ID	$v\sin(i)$	Spectral Type	Reference
HD69267	4.0 km/s	K4III	Fekel (1997)
HD71155	124.5 km/s	A0V	Royer et al. (2002) Bernacca & Perinotto (1970)
HD131977	1.2 km/s	K4V	Fekel (1997)
HD161096	2.5 km/s	K2III	Fekel (1997)
HD188512	1.4 km/s	G8IV	Fekel (1997)

where $\sigma_{\rm LOSVD}$ is the standard deviation of the line-of-sight velocity distribution function obtained from pPXF and α is a proportionality factor. Although this factor cannot be measured from first principles and determined only statistically, we can calibrate the fidelity to recover the rotational velocities of standard stars. Generally, differential effects related to variations in the micro/macro turbulence as well as temperature broadening are all assumed to be part of this scaling parameter α, to $\mathcal{O}(0)$ independent of the input $\sigma_{\rm LOSVD}$.

During our observations we obtained spectra of five rotational velocity standard stars which are summarized in Table 4.1. The results of the calibration are illustrated in Figure 4.6. Each measurement and error bar corresponds to the mean value and the 1-σ value from four pPXF runs around different spectral regions including Hβ, Hγ, the Mgb triplet, and the MgII4481 line. Each of these four values are in turn the median value of ten pPXF runs which differ in the size of the spectral range around those absorption line features. The dashed lines in Figure 4.6 show the error range expected at these low and high values for $\sigma_{\rm LOSVD}$. In particular we expect a dispersion of about 5 km s^{-1} for low $\sigma_{\rm LOSVD}$ and a dispersion up to 20 km s^{-1} for $\sigma_{\rm LOSVD} > 100$ km s^{-1} (see Section 4.2.2.2). We see that, within the errors, our measurements are consistent with the unity relation and therefore, for simplicity, we will adopt $\alpha = 1$ and consequently, for the rest of this work, we will consider our final $\sigma_{\rm LOSVD}$ measurements equal to $v\sin(i)$.

For our BSS sample we run pPXF using spectra from the ELODIE high-resolution spectral library as templates. We select from this library twelve spectra with high S/N (>100) and spectral types A0V, F0V and G2V in order to sample an appropriate spectral type, i.e. stellar mass range. The selection also requires the templates to have small rotational velocities ($v\sin(i) \simeq 5$ km s^{-1}) in order to avoid an additive bias in the $v\sin(i)$ values and to guarantee enough sensitivity in the slow rotator range. In the same way, we also include template stars with moderate ($v\sin(i) \lesssim 30$ km s^{-1}), fast ($v\sin(i) > 50$ km s^{-1}), and extremely fast ($v\sin(i) > 100$ km s^{-1}) rotational velocities in order to properly fit BSSs with high rotational velocities. Similar to what is described for the standards, we calculate the final $v\sin(i)$ for a star by taking the error-weighed average σ value of the fit of four, or less, spectral regions, depending on each spectra due to chip gaps and the quality of the fit. Each of these values is in turn a median value from ten fits, each of these having different sizes of the spectral range typically between 100 and 300 Å. We plot the measurements from the fittings around each spectral region and compare them with the mean final value, $\langle\sigma\rangle$, to check how well constrained our results are and also to test for any strong dependence with the spectral region of the fit. This comparison is shown in Figure 4.7 for each BSS in each GC. The error bars on the y-axis come from taking the 1-σ deviation in the set of ten values. Given that the wavelength ranges of the fit change in each run, therefore varying the amount of potentially bad pixels (specially close to the chip gaps), we are vulnerable to spurious solutions, which most of the times are left out when taking the median, but that affects the overall statistical uncertainty. The large error bars in ωCen are mainly due to this effect, since these spectra are of the lowest S/N given the high level of crowding and difficult sky subtraction in each slit. For the other two GCs, however, we note that the expected errors can account for most of the dispersion between different measurements, and also the unity relation seems to hold for all spectral ranges in all GCs. This, in turn, rules out the possibility of any strong bias in $v\sin(i)$ introduced by the fit of a particular spectral region. We interpret this last result also in favor of including regions around the Balmer lines as acceptable $v\sin(i)$ estimators even though the Balmer lines themselves are very sensitive to gravity and temperature variations. In fact, we find that if we select a pair of BSSs from the same GC which have very similar colors (therefore we assume similar metallicity and temperature) and different estimated rotational velocities, the spectral profile of the Hβ and Hγ lines are almost identical between a fast and a slow rotating BSS, except for the shape of the bottom of the line, which gets smoothed with fast rotation (see Figure 4.8). The fitting will be, therefore, mostly determined by the finer absorption features and by the shape of the bottom of the Balmer lines. As a final check, we note that the MgII4481 line should be ideal for $v\sin(i)$ measurements in late A type stars given that it is free from strong pressure broadening (Gray, 2008). Therefore, the consistency observed in Figure 4.7 is suggesting that, within the errors, we can use the regions around the Balmer lines as reliable indicators.

The final $v\sin(i)$ distribution for each GC is shown in Figure 4.9, while the values are listed in Table 4.2, Table 4.3 and Table 4.4, for NGC 3201, ωCen and NGC 6218, respectively. The cases of NGC 3201 and NGC 6218 are similar, in the way that both show the peak of the distribution around $\sim 20-30$ km s^{-1}. Approximately 90% of the distributions for these GCs are found in the range of between 10 km s^{-1} and 50 km s^{-1}. The other 10% of BSSs, which have $v\sin(i) > 50$ km s^{-1}, lie in the long tail of the distribution which goes up to ~ 90 km s^{-1} for NGC 6218 and up to ~ 130 km s^{-1} for NGC 3201. Note that in these GCs, the fastest rotating BSSs are outliers in the radial

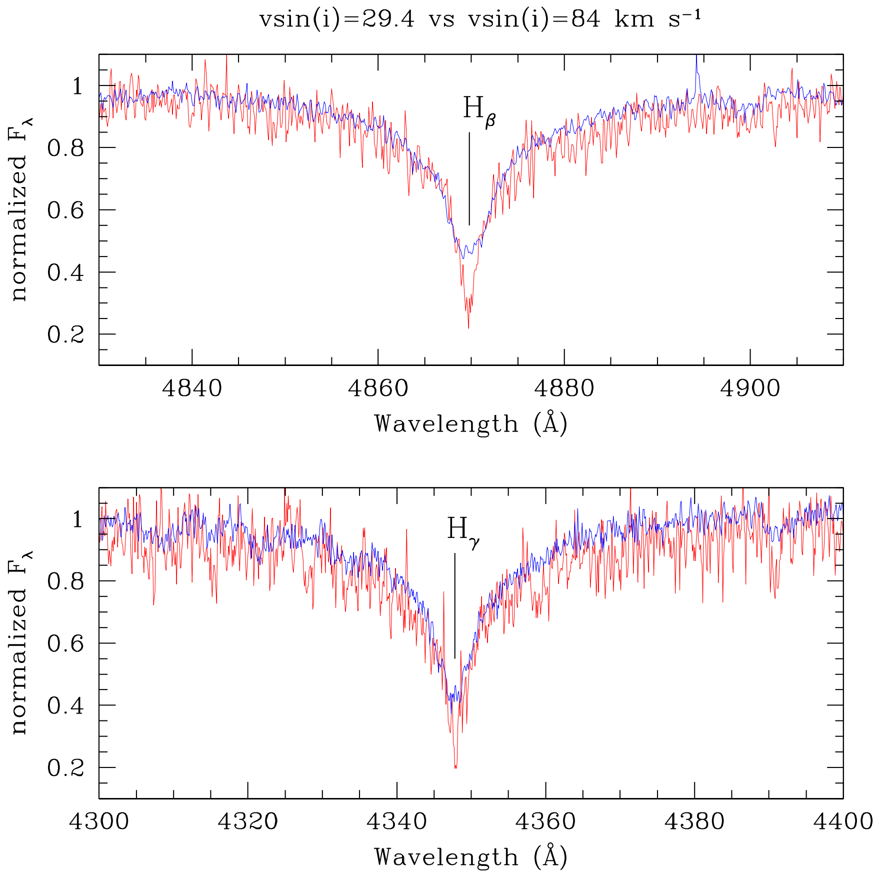

Figure 4.8: Comparison between the spectral profiles of Hβ and Hγ for two BSSs in NGC 3201 with similar atmospheric parameters, particularly BSS2, in blue, and BSS19, in red, as labeled in Table 4.2, where the former has an estimated $v\sin(i)$=84.0 km s^{-1} and the latter shows $v\sin(i)$=29.4 km s^{-1}. The difference in photometric color is $\Delta(V-I)$=0.04 mag, therefore implying very similar effective temperatures. Note how the finer features are smoothed with fast rotation, as well as the bottom of the Balmer lines.

velocity distribution, which could also be a clue to their formation history. The case of ωCen is different since it shows a $v\sin(i)$ distribution slightly shifted towards higher rotational velocities. The bulk of its distribution function is between 20 and 70 km s^{-1}, with a peak around 30 km s^{-1}. This bulk contains 80% of the total sample and the remaining BSSs form a tail of the distribution function with $v\sin(i)$ values up to ~160 km s^{-1}. For this massive GC, the fraction of BSSs with $v\sin(i) > 50$ km s^{-1} corresponds to 30%, in agreement to what was reported in Lovisi et al. (2013a) for their sample.

We note that, contrary to what is normally found, we find no BSSs rotating slower than 10 km s^{-1}, and, in the case of ωCen, no BSSs rotating slower than 20 km s^{-1}. Therefore, we may be systematically overestimating the $v\sin(i)$ for slow rotators. One possible explanation of such a relatively high lower $v\sin(i)$ cut-off might be simply due to our sample selection. Another reason might be that our $v\sin(i)$ calibration (Figure 4.6)

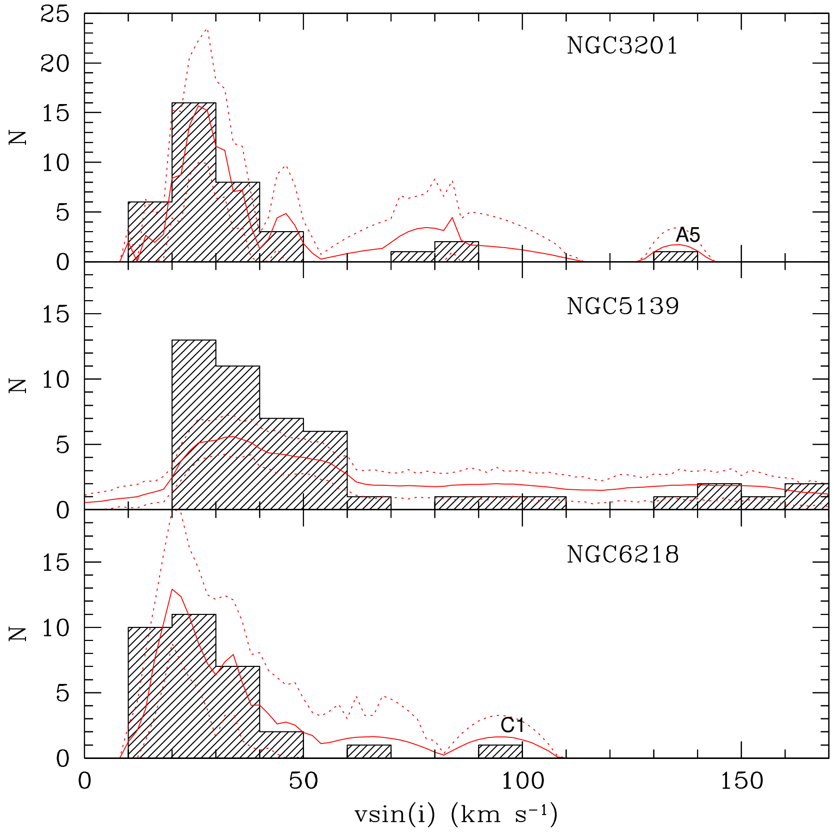

Figure 4.9: Distributions of the $v\sin(i)$ measurements for all BSSs in NGC 3201 (*top*), NGC 5139 (*middle*), and NGC 6218 (*bottom panel*). The red solid curves illustrate non-parametric probability density estimates using an Epanechnikov kernel function together with their 90% confidence limits shown as dotted curves. Note that the probability density estimate takes into account the uncertainties of the individual measurements. Due to the lower S/N of the NGC 5139 measurements the curves appear less peaked than for the other two GCs. The two labeled BSSs (A5 and C1) with extreme $v\sin(i)$ values correspond to those labeled in Figure 4.4.

which is based on late-type stars to fix the slow rotating end of the $v\sin(i)$ parameter space, is affected significantly different than in the hotter target BSSs, probably due to large differences in the micro and macro-turbulence, as well as in the temperature broadening between late and early type stars, which could well be of the order of 10 km s^{-1}. Since we concentrate on distribution functions of slow and fast rotators and only care about distinguishing between them, we do not expect this issue to affect any of our conclusions based on the differential analysis.

4.3 Discussion

4.3.1 BSS Spatial Distribution

One of the strongest clues to understanding the nature of BSSs comes from their spatial distribution in GCs. The radial distribution profiles of the BSS fractions are clearly bimodal for many GCs (Ferraro et al., 1997), but much flatter for others (Dalessandro et al., 2008; Ferraro et al., 2006b). This radial density profile morphology was recently claimed to be tightly related to the dynamical state of the parent GC (Ferraro et al., 2012). At the same time, many ideas were put forward regarding the dependence of this distribution on the environment for different BSS formation channels (Davies et al., 2004; Piotto et al., 2004). In particular, it was claimed that mass transfer BSSs would form preferentially in the loose outskirts of GCs where the low stellar densities would allow binary systems to survive long enough to transfer sufficient stellar material from the donor star, while such binaries would get disrupted much more rapidly in the dense cluster cores. In contrast, BSSs formed through collisions were expected to be found preferentially in GC cores, where the stellar densities are high enough for these relatively rare events to actually occur at significant rates (Ferraro et al., 1997). This scenario has not yet clearly been demonstrated observationally to be at work, and evidence so far is very unclear about the spatially dependent importance of the different BSS formation channels due to the fact that both types of BSS populations are simultaneously present in a GC.

The large spatial coverage of our BSS sample allows us to search for spatial correlations between $v\sin(i)$ and the cluster-centric radius. This may unveil differences in the two populations identified by their $v\sin(i)$ signatures: BSSs that belong to the bulk of the $v\sin(i)$ distribution, i.e. with rotational velocities around $\sim 10-70$ km s^{-1} and rapidly rotating[5] BSSs with $v\sin(i) > 70$ km s^{-1}. In Figure 4.10 we plot the BSS $v\sin(i)$ values against their projected cluster-centric distance in units of the GC core radius, adopting the values $r_c = 1.3', 2.37'$, and $0.79'$ for the core radius of NGC 3201, NGC 5139, and NGC 6218, respectively, taken from the 2010 update of Harris (1996). We find that, with the exception of two BSSs in ωCen, all fast rotating BSSs are significantly concentrated within $\sim 2\,r_c$, while BSSs with $v\sin(i) < 70$ km s^{-1} populate the entire spatial extent of their parent GC. This relation also holds for BSSs with $v\sin(i)$ below and above 50 km s^{-1} (the usual fast rotator limit) in NGC 3201 and NGC 6218. We also show, as vertical dashed lines, the central velocity dispersion of each GC in order to asses the possibility of star blending causing the inner BSSs to appear artificially as fast

---

[5] The term 'fast rotator' will, from now on, be used for BSSs with $v\sin(i) > 70$ km s^{-1}, unless it is stated otherwise.

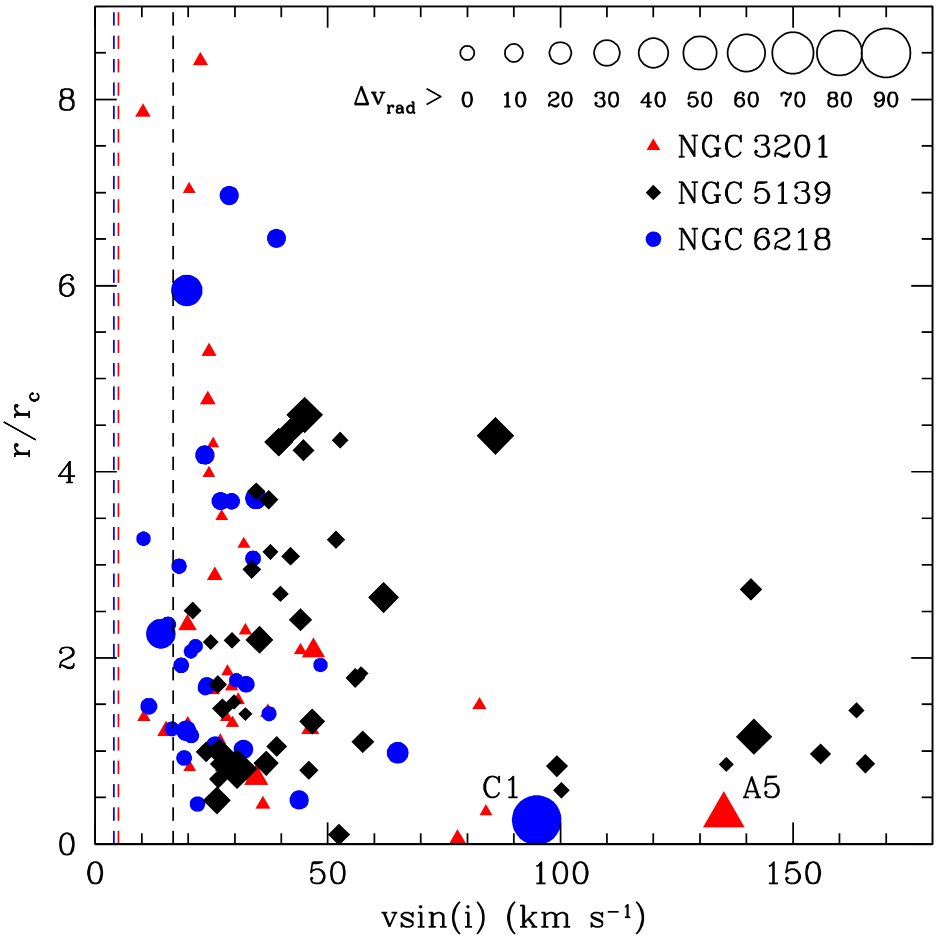

Figure 4.10: Correlation between the projected cluster-centric distance vs. $v\sin(i)$ for BSSs in NGC 3201 (*red triangles*), NGC 5139 (*black diamonds*), and NGC 6218 (*blue squares*). The symbol sizes are parametrized by the radial velocity offset with respect to the systemic velocity of the host GC and are scaled as shown in the upper right. The dashed vertical lines indicate the central velocity dispersion of each GC, color coded as the symbol color. The two labeled BSSs correspond to the ones in Figures 4.4 and 4.9. Note that for NGC 5139 we lack spatial coverage beyond $\sim 4.5\,r_c$ and, thus, do not cover the outermost regions (see also Figure 4.1).

rotators. We see that, in all three GCs, the velocity dispersion is significantly smaller than the rotational velocities of the fastest BSSs and therefore unable to be causing this spatial pattern. Interestingly, the fastest rotators in NGC 3201 (A5) and NGC 6218 (C1) have anomalous radial velocities and are located, in projection, even deeper in the cluster center at $< 0.5\,r_c$. Like the two fast rotators in ωCen at $> 2\,r_c$, these two rapidly rotating BSSs could possibly be in the early stage of ejection from their host GCs, given their projected locations and radial velocity offsets with respect to their parent stellar system. On the other hand, if the two fast rotators in ωCen at $> 2\,r_c$ were also formed in the inner regions, then they are possibly already well in the process of ejection. In agreement with this, we find that the furthest out of the two has a radial velocity of 288.3 km s^{-1}, right on the edge of the radial velocity distribution of ωCen (see Figure 4.4). Another interpretation is simply that fast rotating BSSs form at the same rate both in the outskirts and in the central core of its parent GC, and they later sink down into the inner regions due to mass segregation processes. Our data favors the first scenario, the one in which fast rotating BSSs form preferentially in the inner regions, since, in all three GCs, we find slow rotating BSSs distributed across the entire cluster's spatial extent with a certain underlying density profile, while fast rotators seem to depart from such a profile into a much more concentrated one. A Kolmogorov-Smirnov test has been performed on the slow- and fast-rotating BSS subsamples and it was found that the hypothesis in which the group consisting of BSSs with $v\sin(i)>70$ km s^{-1} and the one with $v\sin(i)<70$ km s^{-1} are drawn from the same cluster-centric density distribution has a p-value <0.005. This is consistent with our idea that fast rotating BSSs are indeed located preferentially in the deeper regions of these clusters. The same test was performed for the individual clusters and we found a p-value < 0.04 for NGC 3201 and NGC 6218, while NGC 5139 gives a p-value <0.2. Therefore, even for the individual samples we find that the radial distributions of fast rotating BSSs are consistent with being shifted towards the inner regions compared to the radial distribution of slow rotating BSSs.

Lovisi et al. (2010) reported three fast rotators in M4 having anomalous radial velocities and suggested a scenario in which three and four-body interactions occurring in the dense GC cores may be responsible for creating these fast rotating BSSs by transferring large amounts of angular momentum into kinetic energy. As stated in the last paragraph, we think our results can be linked to the same phenomenon, where the progenitors of some fast-rotating BSSs in our sample experienced a recent interaction event in the GC core regions that put them on a hyperbolic trajectory, kicking the BSS out of the GC gravitational potential at relatively high velocities ($v_{\rm rad}\sim 100$ km s^{-1}).

4.3.2 Spin-Down and Ejection Timescale Estimates for Rapidly Rotating BSSs

As it was shown in Chapter 3, we find typical BSS masses in the range of $0.8-1.35\,M_\odot$ in our sample GCs. We use the stellar evolution models of Ekström et al. (2012) to estimate the typical spin-down timescales for stars in this mass range and find that the longest spin-down time to reach equatorial rotational velocities below $v_{\rm eq,rot}\simeq 10$ km s^{-1} is about $200-300$ Myr for $0.8\,M_\odot$ stars and decreases to ~ 100 Myr for a $1.35\,M_\odot$ star. In addition to this internal stellar dynamics estimate, we use a back of the envelope calculation including the quantities provided in Georgiev et al. (2009) and Harris (1996) to compute the escape times from the GC centre out to the tidal radius for the two

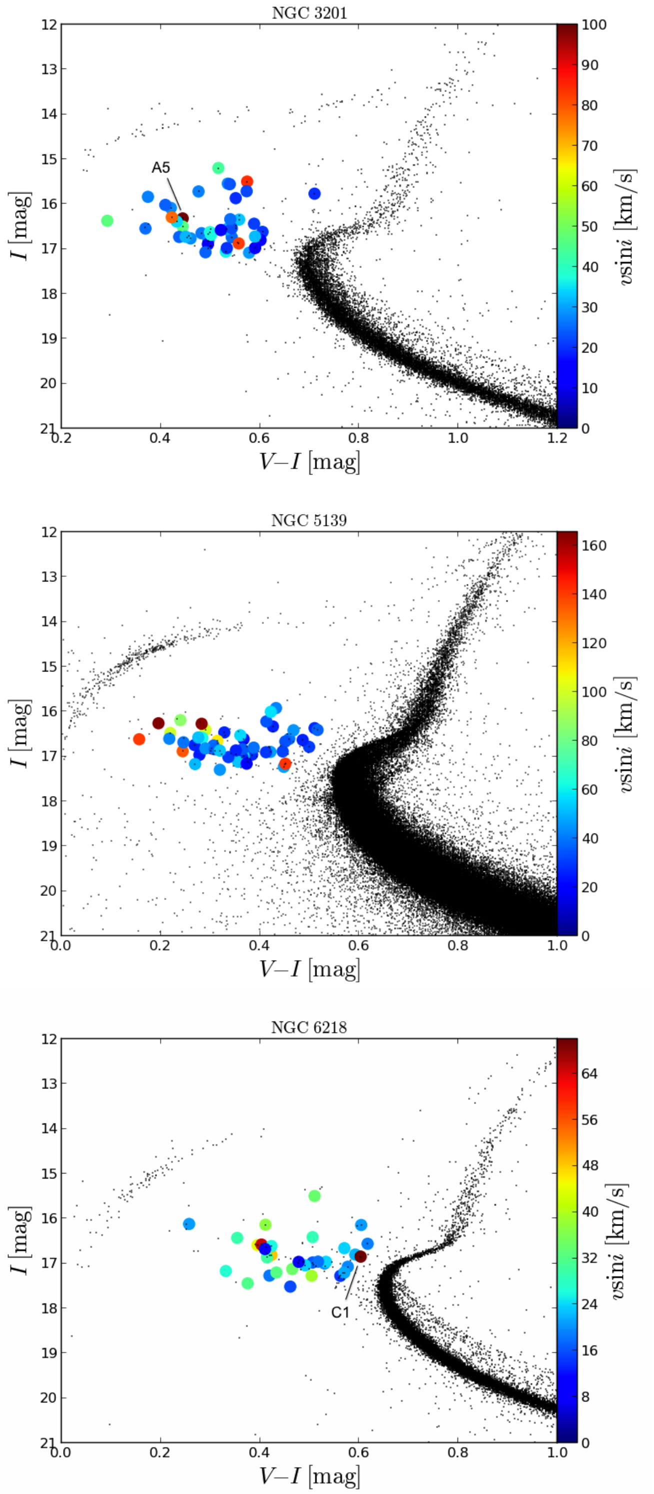

Figure 4.11: Color-Magnitude Diagrams for all three GCs. Big circles are the BSS candidates and the color of the circle shows the $v\sin(i)$ value. Note that bluer BSSs are preferentially faster rotators than redder BSSs. This is best seen in ω Cen. The BSS with anomalously high radial velocities corresponding to those labeled in Figure 4.4 and 4.9 are labeled accordingly.

rapidly rotating BSSs in NGC 3201 (A5) and NGC 6218 (C1). Our calculations give an upper limit of ~ 400 kyr for these BSSs to escape their parent GCs, which would mean that these two rapidly rotating BSSs, if indeed were formed in the core, must have been formed no longer than some hundred thousands years ago, assuming also that the dynamical interaction which set them at high velocities was the same that caused their formation. Similarly, the BSS in ωCen located at $> 2\,r_c$ and with high relative radial velocity previously mentioned could have migrated to its projected location after $\sim$200 kyr if it started its ejection at $\sim 1 r_c$. Hence, we suggest that these rapidly rotating BSSs that are likely in the process of ejection must have experienced strong dynamical interaction no longer than $\sim 10^5$ yrs, which would set a very significant constraint on their age, if we assume that these dynamical interaction were also responsible for their formation. More generally, based on the spin-down timescale estimates, we suggest that the observed rapidly rotating BSSs with $v\sin(i) > 70$ km s^{-1} formed in strong dynamical interaction events in the central regions of their host GCs no longer than ~ 300 Myr ago.

4.3.3 BSS colors vs. $v\sin(i)$

The CMD location of BSSs in relation with their parent GC's stellar population can be a powerful tool for determining their formation history. In Figure 4.11 we plot the CMDs of our target GCs and explicitly show the BSS $v\sin(i)$ values in order to search for global trends. Even though slow and fast rotators are spread over all colors and magnitudes, an unexpected global trend seems to hold for NGC 5139: the fastest rotating BSSs are preferentially bluer than the slower rotating BSSs. We illustrate this more clearly in Figure 4.12 where we plot the BSS $v\sin(i)$ vs. their dereddened $V{-}I$ color, i.e. $(V{-}I)_0$. Reddening values were obtained from Dotter et al. (2010) for NGC 3201 and NGC 6218 and from Villanova et al. (2007) for ωCen using Cardelli et al. (1989) extinction law with $R_V = 3.1$. The increase in the $v\sin(i)$ dispersion for BSS with $(V{-}I)_0 \lesssim 0.25$ mag is striking. In NGC 3201 and NGC 6218, the number of blue BSSs is smaller and a larger sample is required to decide whether a similar trend exists in these GCs. In any case, the majority of red BSSs with colours $(V{-}I)_0 \gtrsim 0.25$ mag show a significantly smaller $v\sin(i)$ dispersion than their blue counterparts with few outliers at high $v\sin(i)$ values. We defer the study of correlations between $v\sin(i)$ values and stellar masses and ages to a future work, but point out that there is an apparent $v\sin(i)$ dichotomy between cool and hot BSSs.

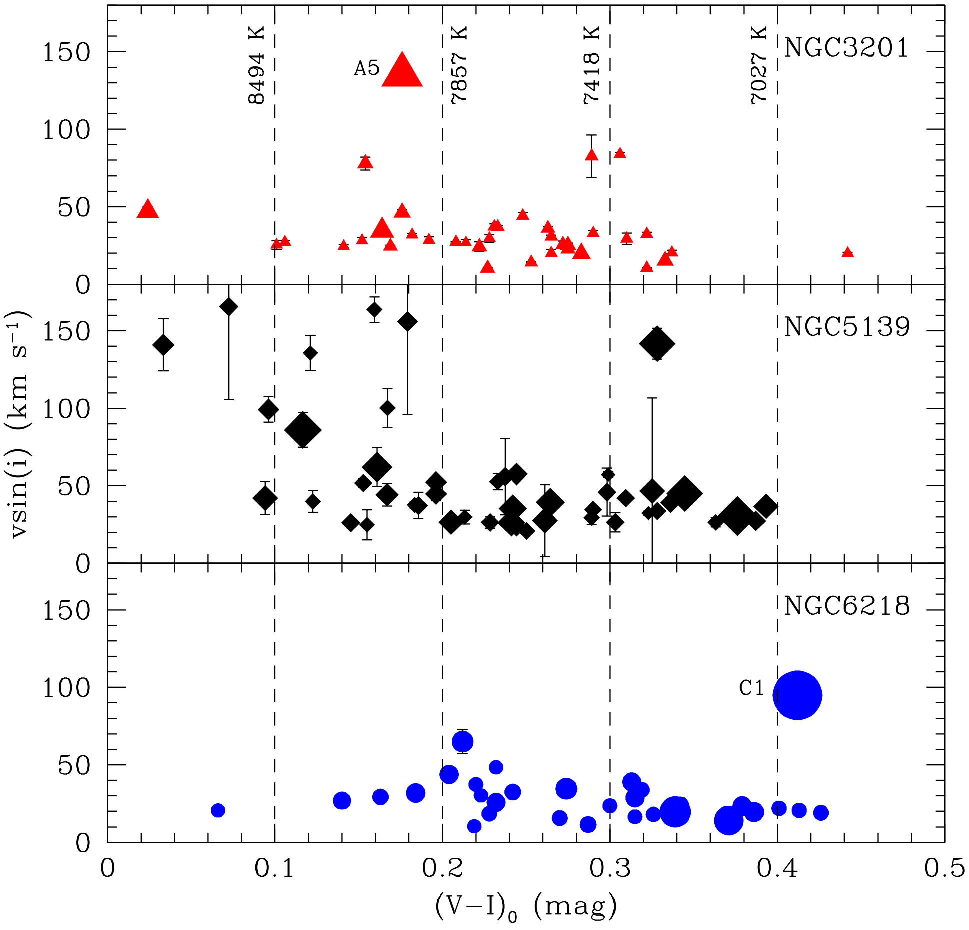

Figure 4.12: Dereddened $V-I$ colors versus $v\sin(i)$ values for our sample BSSs in each target GC, NGC 3201, NGC 5139, and NGC 6218. Note significant increase of the $v\sin(i)$ dispersion in NGC 5139 for BSS colors $(V-I)_0 \lesssim 0.25$ mag. The symbol sizes are parametrized by the radial velocity offset with respect to the systemic velocity of the host GC and are scaled as shown in Figure 4.10. The dashed vertical lines show stellar effective temperature values that correspond to different $V-I$ colors as derived by the relations from Bessell et al. (1998).

4.4 Summary

We obtained multi-object spectroscopy ($R \approx 10000$) with IMACS on the 6.5-meter Baade Telescope at Las Campanas observatory for 137 BSS candidates in three Milky Way GCs (NGC 3201, NGC 5139, and NGC 6218). The BSS candidates were selected from optical HST/ACS and ESO/WFI photometry and resulted in 116 (∼93%) of confirmed BSSs with radial velocities consistent with the host GC systemic velocity for which good quality spectra could be obtained. We convolve template spectra to fit the absorption line profiles of several strong spectral features employing the pPXF technique (Cappellari

& Emsellem, 2004) and conduct detailed Monte-Carlo simulations to determine the fidelity and to constrain the influence of systematics involved in our analysis.

We find a bimodal distribution of BSS $v\sin(i)$ values in all three target GCs, with $\sim 90\%$ of the BSS population having $v\sin(i)$ values between 10 and 50 km s^{-1} and a peak value around $20-30$ km s^{-1} in NGC 3201 and NGC 6218, while in ωCen $\sim 80\%$ of the BSS population has $v\sin(i)$ values between 20 and 70 km s^{-1} and a peak around 30 km s^{-1}. The lower limit of the $v\sin(i)$ distributions (and hence, their peaks) seem higher than what is found in other GCs and we argue that this could be due to either our sample selection, or due to a systematical overestimation of $v\sin(i)$ for the slowest rotating BSSs by ~10 km s^{-1}. This, in any case, would not affect our conclusions based on comparative analysis (fast versus slow rotating BSSs). For all GCs, we find rapidly-rotating BSSs with $v\sin(i) > 70$ km s^{-1}, which are predominantly found in the central regions of their parent GCs and have sometimes differential radial velocities that are consistent with stars in the process of being ejected from their host stellar systems through hyperbolic orbits. We discuss the spin-down timescales of these rapidly-rotating BSSs using calculations for main-sequence stars with equivalent stellar masses and compare them to calculations of the dynamical ejection timescales from their host GCs. We suggest that, in general, most BSSs with $v\sin(i) > 70$ km s^{-1} formed no longer than ~ 300 Myr ago in cluster core regions and may be subsequently ejected from their parent GCs. We find two fast rotating BSSs in NGC 3201 (A4) and in NGC 6218 (C1) likely in the early process of ejection which must have experienced strong dynamical events no longer than some $\sim 10^5$ yrs, as well as one rapidly rotating BSS in ωCen which, as well, appears to be on a hyperbolic trajectory. These strong dynamical events in which BSSs might be kicked out of their parent GCs are likely to be related to their initial formation process.

We investigate the BSS $v\sin(i)$ values as a function of their photometric properties and find that in ωCen the blue BSS population with colors $(V-I)_0 \lesssim 0.25$ mag shows a significantly larger $v\sin(i)$ dispersion than their red counterparts. This remarkable difference between blue and red BSSs is not obvious in the other two GCs due to the smaller BSS samples. This is the first time that photometric properties can be related to dynamical properties of BSSs, such as their rotational and differential radial velocity. We have shown that there is a fundamental bimodality in the $v\sin(i)$ distributions of BSSs and a significant difference in the way BSSs populate the CMD of ωCen according to their internal dynamics. This, in turn, is likely related to their formation processes which we have already discussed in Chapter 3.

Table 4.2: Properties of blue straggler stars in NGC 3201

ID	r/r_c	I	$V-I$	v_r	σ	σ	σ	σ	$v\sin(i)$
					Mgb triplet	H_β	MgII4481	H_γ	
		(mag)	(mag)	(km/s)	(km/s)	(km/s)	(km/s)	(km/s)	(km/s)
BSS1	0.83	15.72	0.48	499.03 ± 1.16	27.9	30.2	22.3	40.0	27.2 ± 0.6
BSS2	0.35	15.50	0.57	504.46 ± 2.64	98.5	84.4	66.4	78.7	84.0 ± 0.8
BSS3	1.66	16.74	0.54	516.73 ± 2.77	38.6	23.9	10.7	31.6	25.0 ± 1.6
BSS4	1.36	16.09	0.42	500.49 ± 1.40	20.4	39.1	34.3	58.2	28.2 ± 1.9
BSS5	1.11	16.65	0.48	502.43 ± 1.65	24.0	28.7	21.0	38.6	26.9 ± 1.8
BSS6	1.55	16.56	0.53	497.15 ± 1.89	20.7	35.1	28.5	33.7	30.8 ± 1.0
BSS7($A5$)	0.31	16.32	0.44	589.95 ± 19.60	121.1	139.5	153.7	126.6	135.2 ± 3.5
BSS8	0.82	16.62	0.60	500.24 ± 0.79	19.3	28.2	25.2	32.2	20.3 ± 1.7
BSS9	1.24	16.50	0.44	486.05 ± 1.06	55.1	44.4	44.2	50.3	46.2 ± 1.9
BSS10	1.30	16.81	0.50	505.71 ± 0.46	–	30.0	25.0	40.8	29.5 ± 2.3
BSS11	1.85	16.77	0.46	499.45 ± 2.21	–	31.1	22.1	21.0	28.5 ± 2.2
BSS12	1.22	16.80	0.60	519.08 ± 2.80	14.4	28.8	10.7	30.9	15.2 ± 0.8
BSS13	0.72	16.35	0.56	500.09 ± 1.81	45.9	31.7	33.5	45.6	33.0 ± 1.6
BSS14	1.43	16.62	0.50	497.62 ± 0.86	–	41.5	35.8	44.8	37.1 ± 1.9
BSS15	1.29	15.77	0.71	499.67 ± 1.08	18.3	23.3	19.2	25.7	19.9 ± 0.6
BSS16	0.71	16.39	0.43	538.25 ± 2.17	33.5	50.6	24.5	53.5	34.6 ± 1.6
BSS17	0.06	16.29	0.42	487.92 ± 1.84	82.2	95.7	67.9	71.9	77.9 ± 4.2
BSS18	0.43	17.06	0.53	494.53 ± 1.42	19.8	37.8	14.8	34.7	36.1 ± 1.0
BSS19	1.69	17.08	0.58	498.17 ± 2.54	10.3	31.4	27.0	34.8	29.4 ± 3.7
BSS20	2.08	15.20	0.52	499.40 ± 1.51	54.3	51.4	33.2	49.5	44.1 ± 2.1
BSS21	1.49	16.88	0.56	508.64 ± 1.64	–	–	–	82.6	82.6 ± 13.8
BSS22	1.37	16.98	0.59	498.62 ± 2.52	15.1	23.7	10.3	35.1	10.5 ± 0.2
BSS23	7.86	16.89	0.49	511.73 ± 2.01	23.0	25.4	10.2	27.9	10.3 ± 0.3
BSS24	3.52	15.84	0.37	500.08 ± 1.04	29.0	26.0	26.5	38.3	27.2 ± 1.0
BSS25	7.03	16.98	0.53	500.05 ± 1.82	15.3	21.2	8.1	23.9	20.2 ± 2.2
BSS26	4.78	17.07	0.49	491.50 ± 4.28	28.3	–	11.8	35.0	24.2 ± 3.1
BSS27	5.29	16.73	0.44	511.07 ± 2.57	24.5	25.0	22.2	38.3	24.5 ± 0.7
BSS28	4.30	16.54	0.37	501.01 ± 2.32	–	31.4	22.0	–	25.4 ± 2.9
BSS29	8.42	16.54	0.54	492.50 ± 2.78	–	28.6	11.8	36.4	22.6 ± 0.9
BSS30	1.41	16.69	0.50	507.86 ± 1.90	33.0	38.6	10.5	34.0	37.0 ± 0.9
BSS31	2.89	16.34	0.54	511.61 ± 1.40	23.5	27.8	27.5	46.8	25.7 ± 2.2
BSS32	2.35	15.87	0.55	522.94 ± 2.07	16.7	28.3	19.1	40.6	19.9 ± 0.6
BSS33	2.29	16.58	0.52	507.21 ± 1.09	14.0	31.5	9.7	32.1	14.1 ± 0.2
BSS34	2.08	16.37	0.29	469.66 ± 0.79	46.3	46.4	31.4	60.0	46.9 ± 3.1
BSS35	2.29	16.72	0.59	498.72 ± 2.58	20.3	35.0	17.7	33.9	32.3 ± 1.3
BSS36	3.98	16.02	0.41	504.25 ± 2.15	–	26.5	24.3	–	24.4 ± 1.0
BSS37	3.23	16.73	0.45	503.97 ± 1.49	–	32.2	27.2	46.0	32.0 ± 0.8

Table 4.3: Properties of blue straggler stars in NGC 5139

ID	r/r_c	I (mag)	$V-I$ (mag)	v_r (km/s)	σ Mgb triplet (km/s)	σ H_β (km/s)	σ MgII4481 (km/s)	σ H_γ (km/s)	$v\sin(i)$ (km/s)
BSS1	1.05	16.61	0.46	209.63 ± 2.02	–	36.4	8.0	53.6	39.0 ± 1.0
BSS2	1.32	17.23	0.45	257.97 ± 4.95	–	–	–	46.6	46.6 ± 60.0
BSS3	1.15	17.16	0.45	284.99 ± 18.59	–	158.6	–	139.9	141.6 ± 10.0
BSS4	0.79	16.90	0.42	214.34 ± 1.51	–	–	–	45.9	45.9 ± 15.4
BSS5	0.70	16.33	0.43	214.86 ± 5.09	–	–	29.6	26.2	26.5 ± 6.2
BSS6	0.43	16.75	0.27	213.66 ± 2.43	–	26.2	–	31.0	26.2 ± 1.9
BSS7	0.58	16.41	0.29	220.32 ± 3.40	–	105.4	–	89.7	100.3 ± 12.6
BSS8	0.81	16.79	0.50	160.22 ± 2.46	–	30.5	–	30.6	30.5 ± 1.2
BSS9	0.86	16.88	0.24	224.22 ± 3.66	–	–	–	135.7	135.7 ± 11.3
BSS10	0.84	16.48	0.22	206.72 ± 17.92	–	95.7	–	117.3	99.3 ± 8.1
BSS11	0.95	16.96	0.38	258.38 ± 0.36	–	27.4	–	27.7	27.6 ± 23.1
BSS12	1.10	16.99	0.37	204.58 ± 4.14	–	57.8	–	41.7	57.6 ± 2.1
BSS13	0.97	16.82	0.30	245.44 ± 10.95	–	155.9	–	–	155.9 ± 60.0
BSS14	0.99	16.61	0.37	209.96 ± 2.31	21.4	23.5	–	30.1	23.9 ± 1.5
BSS15	1.46	16.37	0.51	210.31 ± 1.99	–	27.3	–	34.0	27.3 ± 0.9
BSS16	1.00	16.46	0.33	197.56 ± 2.77	–	26.5	–	32.7	26.5 ± 4.1
BSS17	0.86	16.63	0.49	220.69 ± 1.78	–	28.0	–	24.9	26.5 ± 3.0
BSS18	0.87	16.41	0.52	197.65 ± 2.56	6.9	40.1	–	36.8	36.8 ± 1.9
BSS19	0.47	17.02	0.36	191.38 ± 7.33	–	49.3	17.2	39.0	26.2 ± 3.1
BSS20	1.78	16.53	0.36	212.79 ± 1.29	–	–	–	55.9	55.9 ± 24.7
BSS21	4.39	16.19	0.24	288.28 ± 4.21	–	83.9	–	118.0	86.0 ± 11.2
BSS22	2.17	16.97	0.28	232.24 ± 3.36	–	18.8	–	44.0	24.9 ± 9.8
BSS23	3.09	15.92	0.43	238.91 ± 1.77	–	42.0	–	41.3	42.0 ± 1.0
BSS24	3.79	16.22	0.41	237.57 ± 2.59	–	37.2	27.8	43.5	34.6 ± 1.2
BSS25	4.34	17.12	0.36	234.85 ± 6.59	–	52.7	–	–	52.7 ± 5.3
BSS26	2.95	16.67	0.45	238.94 ± 1.26	–	33.9	–	27.5	33.7 ± 1.5
BSS27	2.19	16.91	0.41	220.16 ± 4.75	–	28.8	–	35.7	29.4 ± 4.4
BSS28	3.14	16.76	0.31	232.69 ± 1.16	–	37.5	–	48.2	37.7 ± 2.0
BSS29	1.40	16.89	0.45	226.91 ± 2.18	–	32.4	–	29.5	32.3 ± 1.4
BSS30	1.83	16.01	0.42	225.47 ± 3.26	–	64.3	31.6	58.3	57.2 ± 2.0
BSS31	4.23	17.30	0.32	247.63 ± 2.96	–	44.7	–	55.2	44.8 ± 4.2
BSS32	4.61	16.42	0.47	285.25 ± 4.83	–	45.2	–	34.5	45.0 ± 1.6
BSS33	1.53	17.02	0.34	231.19 ± 2.85	–	28.3	–	39.3	29.8 ± 4.5
BSS34	2.19	16.84	0.36	190.82 ± 2.60	–	35.2	–	42.6	35.3 ± 3.0
BSS35	2.69	16.69	0.25	233.78 ± 2.96	–	55.1	–	39.4	39.9 ± 6.9
BSS36	0.86	16.26	0.20	241.15 ± 4.49	–	176.2	–	132.3	165.6 ± 60.0
BSS37	1.44	16.27	0.28	232.61 ± 5.24	–	164.9	–	134.5	163.6 ± 8.2
BSS38	2.73	16.62	0.16	205.38 ± 11.20	–	137.0	100.6	161.0	141.0 ± 16.8
BSS39	4.32	16.80	0.39	188.53 ± 2.66	–	–	–	39.4	39.4 ± 4.6
BSS40	2.65	16.59	0.28	271.06 ± 3.56	–	59.3	–	68.0	62.0 ± 12.5
BSS41	3.27	16.58	0.28	238.78 ± 2.08	–	47.0	–	63.2	51.8 ± 2.9
BSS42	2.41	16.82	0.29	251.05 ± 4.53	–	50.4	27.6	40.8	44.2 ± 7.3
BSS43	4.44	16.61	0.22	258.09 ± 1.20	–	42.4	–	40.2	42.1 ± 10.7
BSS44	2.51	17.16	0.37	237.16 ± 5.34	–	20.7	11.8	43.3	20.9 ± 1.2
BSS45	3.70	16.84	0.31	213.49 ± 1.31	–	38.2	–	33.8	37.3 ± 8.5
BSS46	1.72	16.87	0.35	215.68 ± 2.80	–	26.3	–	–	26.3 ± 3.6
BSS47	0.10	16.87	0.32	206.61 ± 2.05	–	53.5	32.7	44.0	52.4 ± 2.2

Table 4.4: Properties of blue straggler stars in NGC 6218

ID	r/r_c	I	$V-I$	v_r	σ	σ	σ	σ	$v\sin(i)$
					Mgb triplet	H_β	MgII4481	H_γ	
		(mag)	(mag)	(km/s)	(km/s)	(km/s)	(km/s)	(km/s)	(km/s)
BSS1	1.24	16.98	0.51	-42.32 ± 3.46	–	27.6	13.5	–	16.5 ± 1.4
BSS2	1.17	16.14	0.60	-41.03 ± 2.67	–	21.7	18.7	23.5	20.7 ± 2.7
BSS3	1.40	16.14	0.41	-47.41 ± 1.98	–	59.4	33.8	51.3	37.4 ± 2.8
BSS4	1.92	16.81	0.42	-45.63 ± 3.52	77.2	55.9	32.5	49.9	48.4 ± 2.6
BSS5	0.43	16.80	0.59	-41.06 ± 4.83	12.3	24.6	16.8	20.1	22.0 ± 1.7
BSS6	0.47	16.59	0.40	-31.14 ± 4.15	47.9	39.6	37.0	45.5	43.9 ± 2.6
BSS7(C1)	0.26	16.85	0.60	47.03 ± 4.37	104.3	76.7	–	–	94.9 ± 6.0
BSS8	2.26	17.28	0.56	-4.04 ± 17.93	13.7	18.3	–	–	14.1 ± 1.4
BSS9	1.68	17.04	0.49	-47.33 ± 1.50	23.3	26.1	19.2	31.7	23.6 ± 2.0
BSS10	0.93	16.56	0.62	-49.20 ± 3.81	19.2	20.2	11.6	25.8	19.1 ± 0.4
BSS11	1.22	17.07	0.58	-60.67 ± 1.93	27.0	–	17.6	23.2	19.6 ± 1.8
BSS12	0.98	16.58	0.40	-24.66 ± 2.43	43.9	–	66.8	74.3	65.0 ± 7.8
BSS13	1.05	16.61	0.42	-57.21 ± 1.68	26.5	24.6	22.9	34.6	25.8 ± 1.7
BSS14	1.76	16.86	0.41	-43.41 ± 3.38	–	42.8	27.8	26.7	30.4 ± 1.5
BSS15	2.13	17.20	0.57	-46.08 ± 2.18	14.1	33.1	12.4	–	21.6 ± 2.2
BSS16	6.97	16.41	0.51	-31.07 ± 6.48	–	–	28.1	56.5	28.8 ± 3.1
BSS17	5.95	17.00	0.53	-0.05 ± 17.34	–	19.6	26.4	27.6	19.7 ± 1.3
BSS18	3.69	17.17	0.33	-55.31 ± 1.40	–	27.5	25.0	25.7	27.0 ± 0.8
BSS19	4.18	16.66	0.57	-58.38 ± 2.93	–	22.0	26.7	33.6	23.6 ± 1.3
BSS20	2.07	16.12	0.26	-45.48 ± 2.46	–	30.8	19.8	33.9	20.6 ± 1.2
BSS21	2.36	17.52	0.46	-39.58 ± 4.21	–	15.2	–	17.2	15.7 ± 1.9
BSS22	3.68	16.43	0.35	-51.02 ± 1.31	–	36.7	26.0	47.7	29.3 ± 0.8
BSS23	3.07	15.50	0.51	-39.51 ± 3.90	73.3	49.6	30.9	35.5	33.9 ± 1.7
BSS24	1.92	17.27	0.42	-49.02 ± 0.91	9.8	25.6	31.5	12.7	18.5 ± 1.9
BSS25	3.71	17.12	0.47	-64.62 ± 3.32	12.4	36.1	–	16.1	34.6 ± 0.8
BSS26	1.70	16.96	0.53	-53.54 ± 3.56	28.1	21.3	9.2	26.7	24.0 ± 2.3
BSS27	2.99	16.96	0.52	-48.39 ± 1.28	11.1	21.6	22.2	19.1	18.1 ± 1.9
BSS28	1.02	17.44	0.38	-58.69 ± 3.46	43.2	–	10.3	33.8	31.9 ± 3.9
BSS29	1.48	16.96	0.48	-52.06 ± 3.75	15.3	32.6	8.0	19.9	11.5 ± 0.3
BSS30	3.28	16.68	0.41	-45.76 ± 4.37	13.2	31.4	10.2	41.1	10.4 ± 0.4
BSS31	1.72	17.20	0.43	-51.76 ± 2.10	19.9	34.9	30.9	16.8	32.5 ± 1.2
BSS32	6.51	17.27	0.50	-57.36 ± 3.76	37.9	47.5	52.9	18.1	39.0 ± 2.5

Bibliography

Bailyn , C. D. 1995, Annual Review of Astronomy and Astrophysics, 33, 133

Bellini, A.; Piotto, G.; Bedin, L. R.; Anderson, J.; Platais, I.; Momany, Y.; Moretti, A.; Milone, A. P.; Ortolani, S.; 2009, Astronomy & Astrophysics, 493, 959

Benz, W., & Hills, J. G., 1987, The Astrophysical Journal, 323, 614

Bessell, M. S., Castelli, F., & Plez, B. 1998, Astronomy & Astrophysics, 333, 231

Cappellari, M., & Emsellem, E. 2004, Publications of the Astronomical Society of the Pacific, 116, 138

Cardelli, J. A., Clayton, G. C., & Mathis, J. S. 1989, The Astrophysical Journal, 345, 245

Dalessandro E., Lanzoni B., Ferraro F. R., Rood R. T.,Milone A., Piotto G., Valenti E., 2008, The Astrophysical Journal, 677, 1069

Davies, M. B., Piotto, G., & de Angeli, F. 2004, Monthly Notices of the Royal Astronomical Society, 349, 129

Dotter, A., Sarajedini, A., Anderson, J., et al. 2010, The Astrophysical Journal, 708, 698

Ekström, S., Georgy, C., Eggenberger, P., et al. 2012, Astronomy & Astrophysics, 537, A146

Fekel, F. C. 1997, Publications of the Astronomical Society of the Pacific, 109, 514

Ferraro, F. R., Paltrinieri, B., Fusi Pecci, F., et al. 1997, Astronomy & Astrophysics, 324, 915

Ferraro, F. R., Sabbi, E., Gratton, R., et al. 2006, The Astrophysical Journal Letters, 647, L53

Ferraro, F. R., Sollima, A., Rood, R. T., et al. 2006, The Astrophysical Journal, 638, 433

Ferraro, F. R., Beccari, G., Dalessandro, E., et al. 2009, Nature, 462, 1028

Ferraro, F. R., Lanzoni, B., Dalessandro, E., et al. 2012, Nature, 492, 393

Fusi Pecci, F., Ferraro, F. R., Corsi, C. E., Cacciari, C., & Buonanno, R., 1992, The Astronomical Journal, 104, 1831

Georgiev, I. Y., Hilker, M., Puzia, T. H., Goudfrooij, P., & Baumgardt, H. 2009, Monthly Notices of the Royal Astronomical Society, 396, 1075

Gray, D. F. 2008, The Observation and Analysis of Stellar Photospheres, by David F. Gray, Cambridge, UK: Cambridge University Press, 2008,

Harris, W. E. 1996, The Astronomical Journal, 112, 1487

Kaluzny, J., Olech, A., Thompson, I. B., et al. 2004, Astronomy & Astrophysics, 424, 1101

Knigge, C., Leigh, N., & Sills, A. 2009, Nature, 457, 288

Leigh, N., Sills, A., & Knigge, C. 2009, Monthly Notices of the Royal Astronomical Society, 399, L179

Leigh, N., Sills, A., & Knigge, C. 2011, Monthly Notices of the Royal Astronomical Society, 416, 1410

Lombardi, J. C. Jr.; Warren, J. S.; Rasio, F. A.; Sills, A.; Warren, A. R., 2002, The Astrophysical Journal, 568, 939

Lovisi, L., Mucciarelli, A., Ferraro, F. R., et al. 2010, The Astrophysical Journal Letters, 719, L121

Lovisi, L., Mucciarelli, A., Lanzoni, B., et al. 2012, The Astrophysical Journal, 754, 91

Lovisi, L., Mucciarelli, A., Lanzoni, B., Ferraro, F. R., & Dalessandro, E. 2013, arXiv:1301.3295

Lovisi, L., Mucciarelli, A., Lanzoni, B., et al. 2013, arXiv:1306.0839

Bernacca, P. L., & Perinotto, M. 1970, Contributions dell'Osservatorio Astrofisica dell'Universita di Padova in Asiago, 239, 1

Mazur, B., Krzemiński, W., & Thompson, I. B. 2003, Monthly Notices of the Royal Astronomical Society, 340, 1205

Piotto, G., De Angeli, F., King, I. R., et al. 2004, The Astrophysical Journal Letters, 604, L109

Prugniel, P., & Soubiran, C. 2001, Astronomy & Astrophysics, 369, 1048

Robin, A. C., Reylé, C., Derrière, S., & Picaud, S. 2003, Astronomy & Astrophysics, 409, 523

Royer, F., Grenier, S., Baylac, M. O., Gómez, A. E., Zorec, J. 2002, Astronomy & Astrophysics, 393, 897

Sarajedini, A., Bedin, L. R., Chaboyer, B., et al. 2007, The Astronomical Journal, 133, 1658

Sarna, M. J., & De Greve, J. P., 1996, Quarterly Journal of the Royal Astronomical Society, 37, 11

Sills, A. 2010, American Institute of Physics Conference Series, 1314, 105

Sills, A., Adams, T., & Davies, M. B., 2005, Monthly Notices of the Royal Astronomical Society, 358, 716

Stryker, L. L. 1993, Publications of the Astronomical Society of the Pacific, 105, 1081

Tonry, J., & Davis, M. 1979, The Astronomical Journal, 84, 1511

Villanova, S., Piotto, G., King, I. R., et al. 2007, The Astrophysical Journal, 663, 296

Zloczewski, K., Kaluzny, J., Rozyczka, M., Krzeminski, W., & Mazur, B. 2012, ACTAA, 62, 357

Chapter 5

The BSS Population in NGC 1261: Evidence for a Post-Core-Collapse Bounce State.

In this chapter, we work on the topics described in Section 1.5 and study the color-magnitude diagram properties of BSSs. By comparing the data to stellar collision models we are able to present evidence for a very particular dynamical history in NGC 1261, making it a similar, yet unique case among other GCs with well defined BSS features, such as M 30 and NGC 362. In Section 5.1 we present the data used in this work, then we present the analysis of the CMD in Section 5.2. We discuss the implications for the dynamical history of NGC 1261 in Section 5.3, and then summarise our results in Section 5.4.

5.1 Data Description

The inner region photometric catalog comes from the HST/ACS Galactic Globular Cluster Survey (Sarajedini et al., 2007). It consists of ∼30 min. exposures in the F606W ($\sim V$) and F814W ($\sim I$) bands for the central $3.4' \times 3.4'$ field of NGC 1261. The photometry was corrected to account for updated HST/ACS WFC zero points and calibrated in the Vega photometric system. The catalog provides high quality photometry down to ~ 6 mag below the main-sequence turn-off. Additionally, we performed PSF photometry using the DoPHOT software package (Alonso-García et al., 2012; Schechter et al., 1993) on HST/WFC3 data taken with the F336W ($\sim U$) band, available from the Hubble Legacy Archive (PI: Piotto, Proposal ID: 13297). The photometry was calibrated using Stetson standards (Stetson, 2000) from the NGC 1261 field. The astrometry was refined with the HST/ACS optical catalog using bright isolated stars, after which we reach a median accuracy of $\sim 0.002''$ between the optical and F336W-band catalogs. We also use wide-field photometry from the catalog published by Kravtsov et al. (2010), built from observations at the 1.3-m Warsaw telescope at Las Campanas Observatory, using a set of $UBVI$ filters and a $14' \times 14'$ field of view. The photometry is calibrated to Stetson (2000) and the median error is $\leqslant$0.04 mag for all filters and colors down to $V = 20$ mag. The complete description of their data reduction and photometric calibration can be found in Kravtsov et al. (2010).

5.2 The central BSS population in NGC 1261

BSSs are selected through their position in a CMD. Having three filters, we can use the additional color information to remove contaminants. First, we cross-match the optical ACS catalog with the F336W-band catalog and keep matched sources with separations < 0.02" ($\sim$ 0.5 pix) and reported errors[1] < 0.03 mag in the F606W and F814W filter. This results in ~ 25000 sources in a $\sim 2.7' \times 2.7'$ field centered on NGC 1261 (see Figure 5.1). We use a F814W < 19.5 mag limit for the BSS selection criteria from Leigh et al. (2011), who define the BSS region based on magnitude and color cuts in the (F606W-F814W) vs. F814W CMD, shown by the polygon in Figure 5.1. All stars inside the region are considered to be BSS candidates, and used in the following analysis (unless removed from the sample; see further down in the text).

We identify two prominent BSS sequences in the CMD, each containing $\sim$20 BSSs (see inset panel). We label them the blue-sequence-BSSs (B-BSSs; shown as blue squares) and the red-sequence-BSSs (R-BSSs, red triangles). Similar to M 30 and NGC 362[2], the B-BSS sequence is narrower and better defined, while the R-BSS sequence is dispersed towards redder colours. We note the appearance of a group of BSSs lying bluer from the B-BSS sequence in the CMD. Since they cannot be directly associated with the B-BSS sequence, as they are clearly separated in the diagram, we choose to label them as extremely-blue-BSSs (eB-BSSs, black circles) and we later discuss their likelihood of being associated to a particular BSS population. This bluer component has neither been observed in M 30 nor in NGC 362, and, if confirmed real, requires a given BSS formation scenario, particular to the history of NGC 1261, that is not present in the other two GCs.

---

[1] Taken from the HST/ACS catalog. More information on the errors is found on the catalog's README file.

[2] Note that in those studies, the HST F555W filter is used as a V band proxy, while we use the F606W filter.

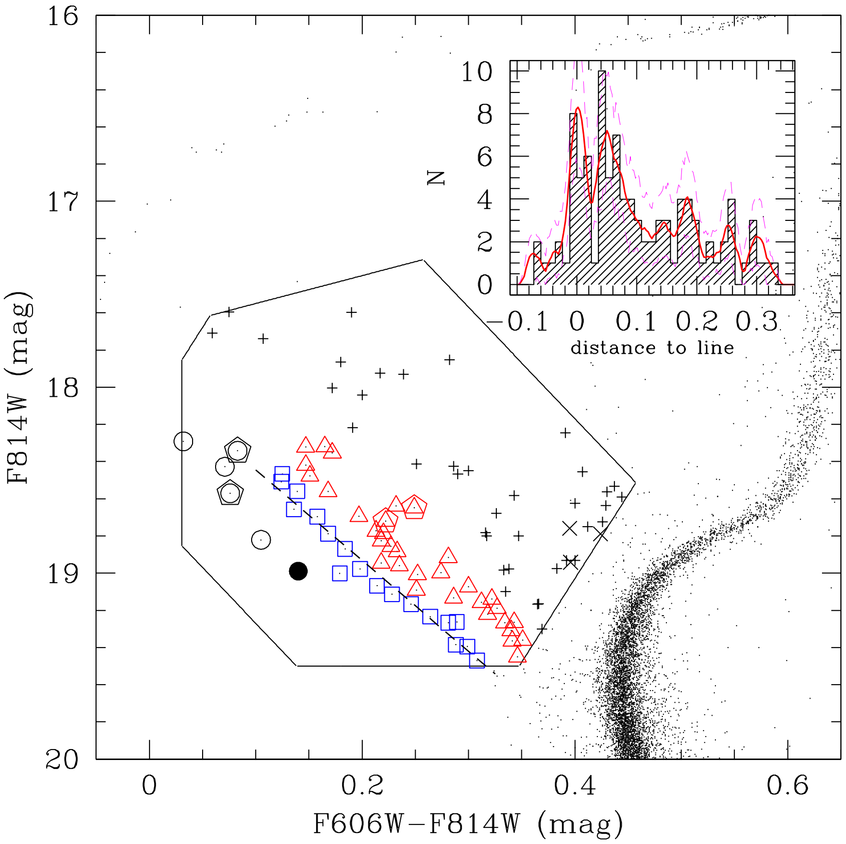

Figure 5.1: (F606W-F814W) vs. F814W CMD of the NGC 1261 inner region. All detections come from the final matched HST catalog. The R-BSS (red triangles), B-BSS (blue squares) and eB-BSS (black circles; filled circle is explained in Fig 5.2) sub-samples are marked; crosses mark the rest of the BSS sample (except for diagonal crosses, see Fig 5.2). Pentagon symbols mark special cases, see Fig 5.2 . The inset panel shows the distribution of BSS perpendicular distances from the best-fit line to the B-BSS sequence (shown as a dashed line) in mag units. The solid red line shows a non-parametric Epanechnikov-kernel probability density estimate with 90% confidence limits represented by the dotted pink lines.

We now introduce the F336W-band photometry for contaminant detection. We show in Figure 5.2 the (F336W-F814W) vs. F336W CMD and use the same symbols for the BSSs as in Figure 5.1. Three BSS candidates plus another star from the eB-BSS group cannot be distinguished from *normal* MS/SGB stars based on their location in the (F336W-F814W) vs. F336W CMD (shown as diagonal crosses and a filled circle, respectively), and hence we exclude them from the full BSS sample and subsequent analysis. It is worth noting that two R-BSSs and another two eB-BSSs in Figure 5.2 (additionally marked with a pentagon) also show significantly redder (F336W-F814W) colors than the rest of their groups. This result may point into photometric variability (since the F336W and F814W-band images on HST were taken ~ 7 years apart, while the F606W and F814W-band exposures are less than an hour apart). Indeed W UMa eclipsing binary systems are frequent among BSSs and have been detected in the double BSS sequences

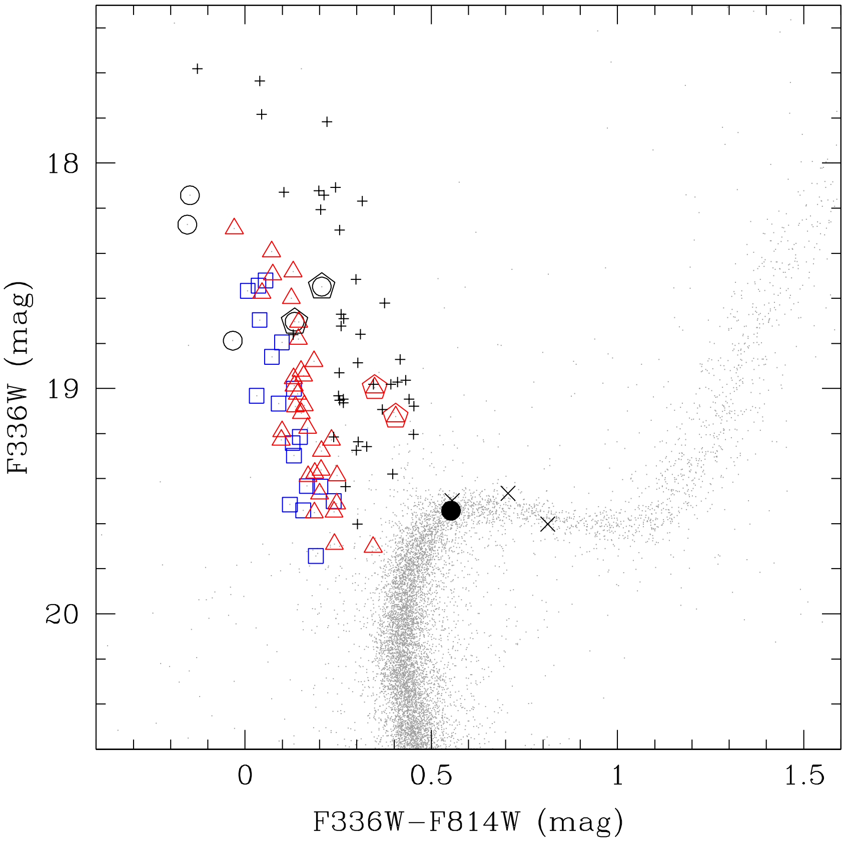

Figure 5.2: (F336W-F814W) vs. F336W CMD of the NGC 1261 inner region. Filled and ×-shape symbols indicate BSS candidates that were rejected from our BSS sample. Pentagon symbols mark BSS candidates that appear slightly faint in the F336W band, relative to their parent subsamples.

of NGC 362 (Dalessandro et al., 2013) and M 30 (Ferraro et al., 2009). In particular, the W UMa BSSs detected in NGC 362 were found to show a typical variability of 0.3 mag in all F390W, F555W and F814W bands (see Figure 10 in Dalessandro et al. (2013)) which could account for the deviations found in (F336W-F814W) colors for these BSSs in NGC 1261. Another explanation could be the blend of cooler stars, which would explain the apparent missing flux in the F336W band. However, the fact that the source centroids were requested to match within 0.02” (∼0.2 FWHM in the optical) in the optical and near-ultraviolet, along with the conservative 0.03 mag error limit in the optical bands, points rather towards a well-fitted single PSF detection. We compare now the identified sub-samples with isochrones from stellar collisional models of Sills et al. (2009) (private communication). The models have a metallicity of $Z = 0.001$ ($[\mathrm{Fe/H}] = -1.27$) and solar-scaled chemical composition ($[\alpha/\mathrm{Fe}] = 0$). In Sills’s models, pairs of stars with masses between 0.4 and 0.8 $M_\odot$ are collided using the MMAS software package (Lombardi et al., 2002). The parent stars are assumed to be non-rotating, and 10 Gyr old at the time of the collision. The collision products are evolved using the Monash stellar evolution code, as described in Sills et al. (2009). The time of the collision is assumed to be $t = 0$, and then isochrones of various ages are obtained by interpolating along the tracks to determine the stellar properties (effective temperature, luminosity, etc.) at ages between 0.2 and 5 Gyr. For the isochrones, we used collision products of the following stellar mass combinations: $0.4{+}0.4, 0.4{+}0.5, 0.4{+}0.6, 0.5{+}0.6, 0.6{+}0.6$, and $0.8{+}0.8\,M_\odot$. We have adopted the distance modulus and reddening values of NGC 1261 from Dotter et al. (2010) and augmented the distance modulus by 0.25 mag in order to match the low-mass end of the collisional isochrone to the location of the main-sequence fiducial line in the CMD[3]. We find that the location of the B-BSSs and eB-BSSs can be reproduced by 2 Gyr and 200 Myr old isochrones of the stellar collisional models, respectively, as seen in Figure 5.3. We note that the agreement of the model with the B-BSSs is remarkably good. The eB-BSS sub-sample, although much less populated, is also somewhat consistent with the collisional 0.2 Gyr isochrone model. This enlarges the likelihood of this BSS feature being a real distinct population. The R-BSSs need further explanation. Ferraro et al. (2009) and Dalessandro et al. (2013) found for M 30 and NGC 362 that the lower bound of the R-BSSs could be fairly well bracketed by the zero-age main-sequence (ZAMS) shifted by 0.75 mag towards brighter luminosities in the V (F555W in their case) band, which approximately indicates the region populated by mass-transfer binaries, as predicted by Tian et al. (2006). In our case we use the 0.25 Gyr old Dartmouth isochrones (Dotter et al., 2008), and find that the R-BSS sequence can only be reproduced by a region bracketed by the 0.25 Gyr old isochrone shifted by 0.45 mag and 0.75 mag to brighter F606W-band luminosities (grey region in the Figure). This shift is less than that required for M 30 and NGC 362 , and we note that a small difference is expected due to slightly different HST filters (F606W vs. F555W) as a V band proxy. However, the prediction by Tian et al. is based only on Case A (main-sequence donor) mass-transfer models. Lu et al. (2010) showed that case B (red-giant donor) mass-transfer products lie indeed in a bluer region than the ZAMS+0.75 mag boundary. Our current understanding of binary mass transfer is limited and, hence, our observations could help putting constraints on future binary stellar evolution models.

5.3 Dynamical State of NGC 1261

Ferraro et al. (2009) and Dalessandro et al. (2013) have demonstrated that M 30 and NGC 362 show signs of being in an advanced state of dynamical evolution, as revealed by their centrally segregated BSS radial profiles (which puts them in the Family III

---

[3] This is mostly caused by the different metallicity/alpha enhancement between the Sills models models and the cluster, which has a metallicity closer to [Fe/H]$\sim -1.35...-1.38$ according to the latest studies (Dotter et al., 2010; Kravtsov et al., 2010; Paust et al., 2010), and a large α-enhancement as it is expected for GCs in the halo (Pritzl et al., 2005; Woodley et al., 2010).

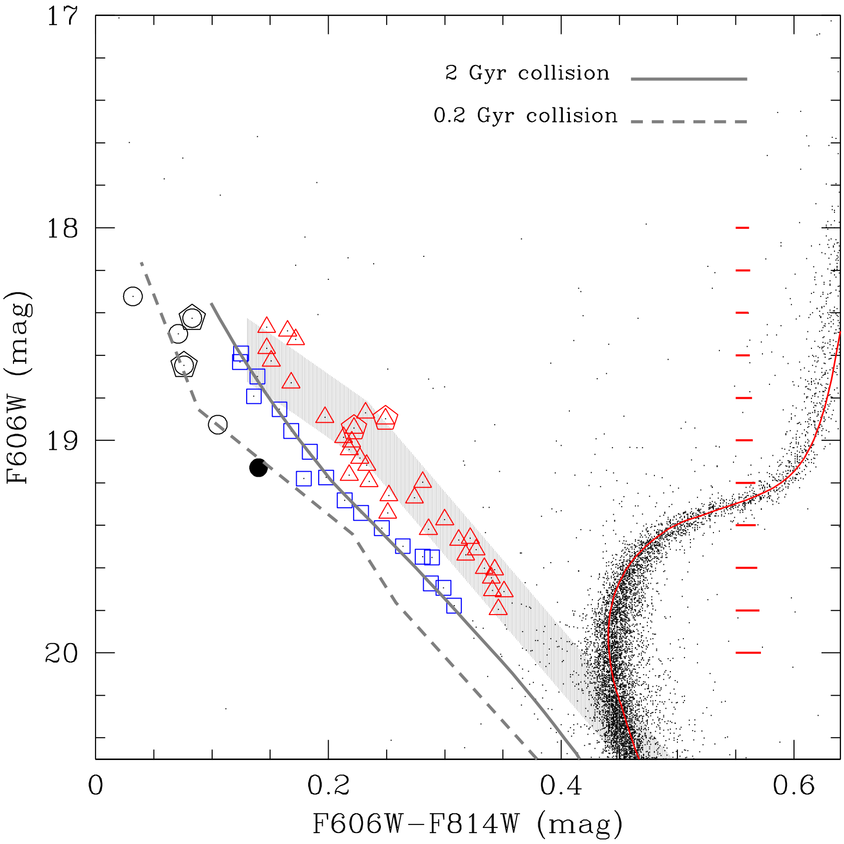

Figure 5.3: (F606W-F814W) vs. F606W CMD of the NGC 1261 inner region with overplotted collisional isochrones of 2 Gyr and 200 Myr old, up to 1.3 $M_\odot$ and 1.6 $M_\odot$, respectively. The grey band shows the zero-age main sequence isochrone, shifted by 0.45 and 0.75 mag to brighter luminosities, to match the R-BSS sequence. The red line is a Dartmouth isochrone with cluster parameters adopted from Dotter et al. (2010). The representative photometric errors as obtained in the HST/ACS catalog are plotted in red bars.

group in Ferraro et al., 2012) and by their centrally peaked radial stellar density profiles. Likewise, we plot in Figure 5.4 the normalized, cumulative BSS radial density profile for all BSS candidates and for the R-BSS and B-BSS sequences in NGC 1261 out to 3.8 core radii, i.e. the extent of the HST observations. As expected, the whole BSS sample, as well as each BSS sequence, are more centrally concentrated than the reference SGB population[4]. However, contrary to what was found in M 30 and NGC 362, we find the B-BSS component more centrally concentrated than the R-BSS component. A K-S test shows that the null-hypothesis of these stars being drawn from the same radial distribution has a p-value of 0.33, which implies a non-negligible likelihood for common parent distributions. Nevertheless, the difference between these profiles and the ones for M 30 and NGC 362 is still significant and motivates a discussion on possible qualitative differences of BSS formation history in NGC 1261 versus the other GCs. We do not find any B-BSSs inside $\sim 0.5\, r_c$ (or about 10”), in agreement with Ferraro et al. (2009) and

---

[4] We choose SGB stars from the CMD inside the 19.2<F606W<19.5 mag range.

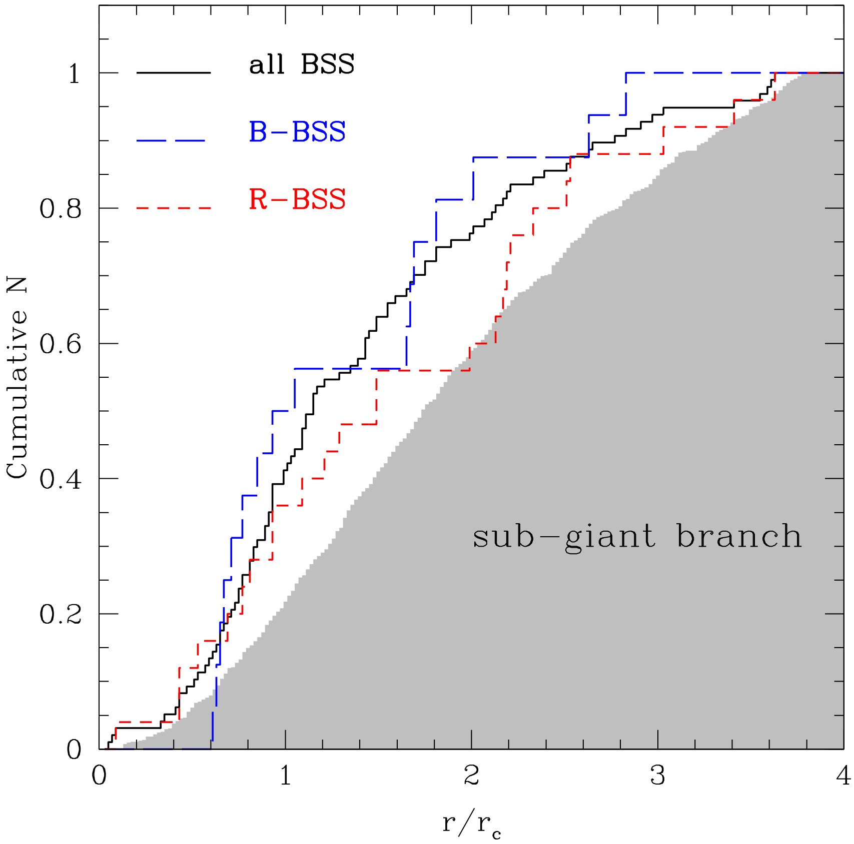

Figure 5.4: Normalized cumulative radial distribution of BSSs in the central $3.8\, r_c$ of NGC 1261. The full BSS sample (solid black line), B-BSSs (long-dashed blue line) and R-BSSs (short-dashed red line) are plotted. The corresponding cumulative distribution of the reference SGB population is shown as the shaded region. We use the centre of gravity coordinates RA = 03h 12m 16.21s, DEC = $-55^{\circ}\, 12'\, 58.4''$ given by Goldsbury et al. (2010), and $r_c = 0.35'$ (Harris, 1996).

Dalessandro et al. (2013), who as well report no B-BSSs within the inner 5-6”($\sim 1.5\, r_c$ and $\sim 0.5\, r_c$ respectively). These authors suggest that dynamical kicks are responsible for clearing the innermost region of any B-BSSs. The detailed process is, however, unknown as accurate dynamical models are numerically expensive and, thus, still lacking.

The results from Figure 5.4 alone cannot be used to suggest an advanced dynamical state in NGC 1261, as the central concentration of BSSs is now known to be ubiquitous among all studied GCs. A more complete understanding can be obtained by looking at the BSS radial profile at larger cluster-centric distances, as the radial distance of the normalized BSS density minimum will depend on the cluster's dynamical age. Ferraro et al. (2012) showed that as a GC evolves dynamically the BSS radial density profile takes the form of a central high maximum and a secondary peak at larger radii with a minimum in between. In order to follow this approach we include the wide-field photometry catalog in our analysis and carefully merge it [5] with the inner-region ACS catalog, providing us with a sampling of NGC 1261 out to $r > 30\, r_c$.

We plot in Figure 5.5 the relative fraction of BSSs to SGBs[6] as a function of cluster-centric radius, assuming Poissonian noise for the error bars. The BSSs in the wide-field catalog are the ones selected by Kravtsov et al. (2010), i.e. stars on the BSS region of all (B-V), (V-I) and (B-I) CMDs. We then apply an additional magnitude cut ($I < 19.45$ mag) in order to hold the same faint magnitude limit used with the inner sample (see Fig 5.1)[7]. Considering these selection steps, combining both samples is hence acceptable for our purposes. We find that the BSS fraction is maximal in the center and drops rapidly with radius reaching near to zero at $r \sim 10\, r_c$. A subsequent rising in the fraction profile is discernible, although this is only caused by the detection of two BSSs alone (see the inset panel) and therefore not strongly supported statistically. The absence of a clear outer layer suggests that the majority of the BSS population has already been affected by dynamical friction. Hence, in the framework constructed by Ferraro et al. (2012), NGC 1261 would classify as a dynamically old cluster and would be grouped in late-FAMILY II/FAMILY III , not surprisingly similar to M 30 and NGC 362. Moreover, the half-mass relaxation time is about 10^8 years, which is actually shorter than that of NGC 362, $\log t = 8.7$ and M 30, $\log t = 9.2$, as found in Paust et al. (2010).

However, the core structure of NGC 1261 does not show signatures of core collapse. It is well approximated by a King model with a concentration parameter $c \approx 1.2$ (Harris, 1996; Paust et al., 2010). It has a central luminosity density of 2.22 $L_{\odot}\mathrm{pc}^{-3}$ (Paust et al., 2010), which is relatively low for GCs. Moreover, the binary fraction radial profile found by Milone et al. (2012) shows a flat distribution, i.e. without signs of mass segregation, contrary to the ones in M 30 and NGC 362, which are centrally peaked. Therefore it is not surprising that the binary merger products, i.e. the R-BSS population, in these GCs are also more centrally segregated than the R-BSS population in NGC 1261. This apparent evolutionary contradiction may not be as problematic as it first seems. According to both Monte-Carlo dynamical models (e.g. Heggie & Giersz, 2008) and direct-integration N-body models (e.g. Hurley & Shara, 2012), clusters can go through core-collapse and then, if there is some energy source in the core, stay or pass through a long-lived post-core-collapse bounce state in which they do not show classic post core-collapse signatures. The Heggie & Giersz models of M 4 all went through core collapse at $t = 8\,\mathrm{Gyr}$,

---

[5] The resulting merged SGB radial profile distribution is checked to be smooth and continuous, therefore, ruling out severe completeness issues for the BSSs, which are in a similar magnitude range. The merging point is chosen at 3.8 r_c.

[6] They were selected using a $19.2 < V < 19.5$ mag range cut. We use the "*V ground*" magnitude on the ACS catalog in order to make them compatible with the wide-field gound-based photometry.

[7] The F814W<19.5 mag limit from Fig. 1 is checked using the "*I ground*" magnitude on the ACS catalog and is found to translate to $I < 19.45$ mag.

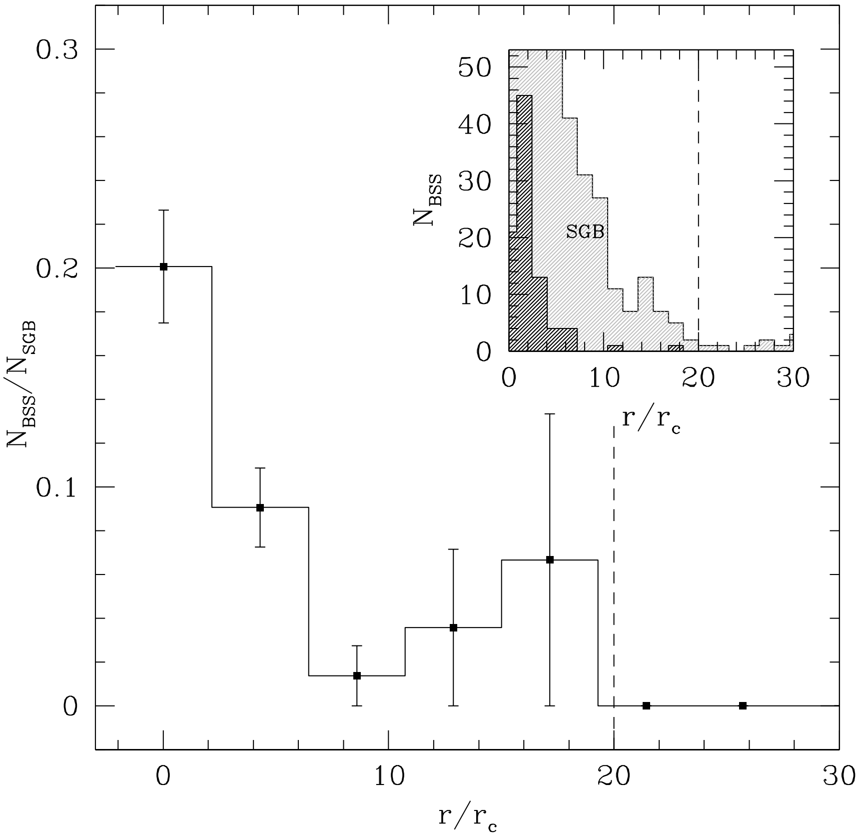

Figure 5.5: Ratio of BSS to SGB stars as a function of radial distance. The inset panel shows the number of BSSs and SGB stars. Both panels have a dashed vertical line indicating the approximate location of the cluster's tidal radius, according to Paust et al. (2010).

and then remained in a non-collapsed state for another ∼2−3 Gyr due to "binary burning" in the core. Hurley & Shara propose a binary black hole as an alternative central potential energy source. We know today that black holes may be common in GCs (e.g. Chomiuk et al., 2013; Strader et al., 2012), so that a binary black hole in the core of NGC 1261 may be considered a valid possibility.

5.4 Summary

We find that the inner BSS population in NGC 1261 includes at least two distinct well defined sequences similar to what was found in M 30 and NGC 362, and as well includes a smaller group of BSSs that have unusually blue colours in the CMD, and which could be associated with a distinct coeval BSS population, if confirmed real. The comparison with collisional stellar evolution models reveals that the B-BSS and eB-BSS sub-samples are consistent with a 2 Gyr and 0.2 Gyr old stellar collision-product population, respectively. This provides the grounds for considering NGC 1261 an extremely valuable test laboratory for stellar collision and BSS formation models. This observation along with evidence collected from the literature suggest as a preliminary interpretation for the dynamical history of NGC 1261 that the cluster experienced a core-collapse phase about 2 Gyr ago, and that since then it has bounced through core oscillations. The subsequent core oscillations occasionally created more BSSs during these short timescale processes when the central stellar density was particularly enhanced – one such likely 0.2 Gyr ago. During these periods of core density enhancements the cluster likely burned some of its core binaries, thereby flattening their radial density distribution profile, and currently the cluster is likely in a post core-collapsed state which, according to different simulations, may appear as an unevolved GC. Follow-up spectroscopic characterization of the BSS sequences in NGC 1261 is of utmost importance in order to confirm and better understand their origins and formation mechanisms, and in particular test the chemical abundance predictions related to different BSS formation models.

Bibliography

Alonso-García, J., Mateo, M., Sen, B., et al. 2012, The Astronomical Journal, 143, 70

Chomiuk, L., Strader, J., Maccarone, T. J., et al. 2013, The Astrophysical Journal, 777, 69

Dalessandro, E., Ferraro, F. R., Massari, D., et al. 2013, The Astrophysical Journal, 778, 135

Dotter, A., Chaboyer, B., Jevremović, D., et al. 2008, The Astrophysical Journal Supplement Series, 178, 89

Dotter, A., Sarajedini, A., Anderson, J., et al. 2010, The Astrophysical Journal, 708, 698

Ferraro, F. R., Beccari, G., Dalessandro, E., et al. 2009, Nature, 462, 1028

Ferraro, F. R., Lanzoni, B., Dalessandro, E., et al. 2012, Nature, 492, 393

Goldsbury, R., Richer, H. B., Anderson, J., et al. 2010, The Astronomical Journal, 140, 1830

Harris, W. E. 1996, The Astronomical Journal, 112, 1487

Heggie, D. C., & Giersz, M. 2008, Monthly Notices of the Royal Astronomical Society, 389, 1858

Hills, J. G., & Day, C. A. 1976, The Astrophysical Journal Letters, 17, 87

Hurley, J. R., & Shara, M. M. 2012, Monthly Notices of the Royal Astronomical Society, 425, 2872

Knigge, C., Leigh, N., & Sills, A. 2009, Nature, 457, 288

Kravtsov, V., Alcaíno, G., Marconi, G., & Alvarado, F. 2010, Astronomy & Astrophysics, 516, A23

Leigh, N., Sills, A., & Knigge, C. 2011, Monthly Notices of the Royal Astronomical Society, 415, 3771

Lombardi, J. C., Jr., Warren, J. S., Rasio, F. A., Sills, A., & Warren, A. R. 2002, The Astrophysical Journal, 568, 939

Lu, P., Deng, L. C., & Zhang, X. B. 2010, Monthly Notices of the Royal Astronomical Society, 409, 1013

McCrea, W. H. 1964, Monthly Notices of the Royal Astronomical Society, 128, 147

Milone, A. P., Piotto, G., Bedin, L. R., et al. 2012, Astronomy & Astrophysics, 540, A16

Paust, N. E. Q., Reid, I. N., Piotto, G., et al. 2010, The Astronomical Journal, 139, 476

Pritzl, B. J., Venn, K. A., & Irwin, M. 2005, The Astronomical Journal, 130, 2140

Sarajedini, A., Bedin, L. R., Chaboyer, B., et al. 2007, The Astronomical Journal, 133, 1658

Schechter, P. L., Mateo, M., & Saha, A. 1993, Publications of the Astronomical Society of the Pacific, 105, 1342

Sills, A., Karakas, A., & Lattanzio, J. 2009, The Astrophysical Journal, 692, 1411

Stetson, P. B. 2000, Publications of the Astronomical Society of the Pacific, 112, 925

Strader, J., Chomiuk, L., Maccarone, T. J., Miller-Jones, J. C. A., & Seth, A. C. 2012, Nature, 490, 71

Tian, B., Deng, L., Han, Z., & Zhang, X. B. 2006, Astronomy & Astrophysics, 455, 247

Woodley, K. A., Harris, W. E., Puzia, T. H., et al. 2010, The Astrophysical Journal, 708, 1335

Chapter 6

Summary and Conclusions

The purpose of this thesis was to provide a wide arrange of observational evidence that could be used to derive constraints for the understanding of formation of BSSs in GCs. The relatively ambiguous aspect of BSSs in the present view of stellar evolution places them in a position of much inquiry. The detailed understating of their true nature is therefore essential if we wish to apply the lessons learned from the local universe and use them to derive information at the larger scales. Regarding the more distant implications, their hot stellar temperatures means that any UV flux characterisation of unresolved stellar systems will be significantly determined by our ability to model the specific frequency of BSSs in such systems. And at the most local and immediate vecinity, their understanding should give us bright ideas on the way that binaries interact and affect the observed population of low and intermediate mass stars, such as our Sun.

We were able to present a comprehensive proper-motion analysis based on Hubble Space Telescope (HST) observations and constructed, for the first time in the literature, proper-motion cleaned BSS catalogs in the inner regions of GCs. This novel approach allowed us to select BSS candidates in regions of the CMD that had been typically avoided by previous studies, given its high contamination of foreground and background stars. We make these catalogs available to the community which will expand the range of this work to hopefully very far-reaching conclusions.

The proper motion information of the cluster populations has allowed us to observe that BSSs posses in average lower velocity dispersion than stars of the main-sequence. This was something that, from basic principles of equipartition, the community had for long only assumed based on the observed BSS luminosities, which set them at inferred higher stellar masses. We have shown on this thesis the largest ever data set of velocity dispersion profiles of BSSs, which indeed confirmed that these are populations that have been greatly affected by two-body relaxation.

We have conducted the largest ever BSS mass distribution survey, based on stellar evolutionary track interpolation in the CMD. These BSS mass estimates are undoubtedly rather approximations of the real stellar masses of individual BSSs. Yet, they have proven to be accurate enough to probe the internal dynamics expected from the thermalisation in the core. In particular, we have shown that more massive BSS samples show a higher degree of relaxation with respect to MS stars. This effect was found to be stronger in dynamically older GCs, where the relaxation times of BSSs should be shorter. In addition, the photometric BSS mass estimates revealed a striking correlation between the average BSS mass and the cluster dynamical age. We argue that this can be explained by mass segregation if we consider that the expected radius of avoidance (r_{avoid}) for BSSs should naturally increase with dynamical age. Given that more massive BSSs should be first affected by two-body relaxation, then you may obtain a core that becomes increasingly populated by more massive BSSs as the cluster evolves dynamically. However, this might not be the entire picture and there could be an additional process also in action. In particular, a very detailed inspection of the CMDs of our entire GC sample, allowed us to use probability density functions of the BSS CMDs and we found that that the bulk of BSSs populate the CMD in different ways, according to the dynamical age of the cluster. This apparent "evolution" of the BSS CMD with dynamical age was shown to be unequivocally connected to the increase in average BSS mass. In more detail, we observed that the BSS positions in the CMD evolve from a more narrow and concentrated diagonal structure peaked at low luminosities, into a less defined and more extended component. The dynamically older GCs show an absence of the concentration of BSSs at low luminosities. This low luminosity peak is in good agreement to what you would expect from a BSS population formed due to primordial binary-evolution. Hence, we argue that dynamically older GCs have predominantly less binary-evolution BSSs in their inner regions, and consequently a higher abundance of dynamical BSSs. This idea goes in the same direction as some of the studies mentioned in Section 1.3, which make our findings a nice follow-up and confirmation of those original works in BSS formation. This argument is strongly supported by the observed lower binary fractions in dynamically older GCs, and the higher BSS mass expected for collision products according to detailed dynamical simulations.

We also tackled the BSS physical properties by studying their spectroscopic dynamical information. We obtained multi-object spectroscopy for 137 BSS candidates in three Milky Way GCs (NGC 3201, NGC 5139, and NGC 6218) and convolved template spectra to fit the absorption line profiles of several strong spectral features. Most notoriously, we found for all GCs that the rapidly-rotating BSSs with $v\sin(i) > 70$ km s^{-1}, are predominantly found in the central regions of their parent GCs and have sometimes differential radial velocities that are consistent with stars in the process of being ejected from their host stellar systems through hyperbolic orbits. This is very interesting to contrast with the previous findings described above. In particular, these fast-rotating BSSs with high differential radial velocities could suggest formation scenarios characterized by strong dynamical interactions. The fact that we find all of these BSSs inside the core regions of their parent GCs is another indication that the dynamical channel is more predominant than previously thought.

The last portion of the thesis is devoted to the comparison of photometric data to stellar collision models. We have found that the inner BSS population in NGC 1261 includes at least two distinct well defined sequences similar to what was found in M 30 and NGC 362, and as well includes a smaller group of BSSs that have unusually blue colours in the CMD, and which could be associated with a distinct coeval BSS population, if confirmed real. The comparison with collisional stellar evolution models reveals that the B-BSS and eB-BSS sub-samples are consistent with a 2 Gyr and 0.2 Gyr old stellar collision-product population, respectively. This provides the grounds for considering NGC 1261 an extremely valuable test laboratory for stellar collision and BSS formation models. This observation along with evidence collected from the literature suggest as a preliminary interpretation for the dynamical history of NGC 1261 that the cluster experienced a core-collapse phase about 2 Gyr ago, and that since then it has bounced through core oscillations. We believe that the results on the BSS formation history in NGC 1261 provide even more confirmation for our early proposal regarding dynamical-channel and binary-channel BSS formation. More specifically, the distinct and incredibly well defined collisional sequences in NGC 1261 and M 30 suggests that, for these GCs, this particular region in the CMD is absent of binary-evolution products, since BSSs in binaries should populate the CMD in a much less defined way, assuming different binary mass-ratios. Note that the relative under-abundance of binary-evolution products is what we, in the early chapters, suggested to be a characteristic of dynamically old GCs. This agrees well with the accepted notion of M 30 being a post-core-collapse cluster.

We believe that the goal of the thesis has been met successfully after combining a vast amount of different results, which all provide appealing evidence for specific constraints on BSS formation. All of our independent studies, using different methodologies, point towards BSSs being created in primordial binary-evolution channels, as well as in dynamical channels, and the data suggests that the predominance of each channel strongly depends on the dynamical age of the GC. More work is needed to obtain detailed and direct measurements of individual BSSs in both predicted regimes and try to build a more robust framework that will allow us to derive quantitative predictions on the field of BSS formation and globular cluster dynamics in general.

List of Figures

List of Tables